2004

Proof of concept design and analysis of active flow control of a supersonic micro-nozzle

Christopher J. Szachta

Proof of Concept Design and Analysis of Active Flow Control of A Supersonic Micro-Nozzle

by

Christopher J. Szachta

A Thesis Submitted In
Partial Fulfillment of the
Requirements for the

MASTER OF SCIENCE
IN
MECHANICAL ENGINEERING

Approved by:

Dr. Jeffrey Kozak Department of Mechanical Engineering	Jeffrey D. Kozak (Thesis Advisor)
Dr. Mark Kempski Department of Mechanical Engineering	Mark H. Kempski (Committee Member)
Dr. Kevin Kochersberger Department of Mechanical Engineering	Kevin Kochersberger (Committee Member)
Dr. Edward C. Hensel Department of Mechanical Engineering	Edward C. Hensel (Department Head)

DEPARTMENT OF MECHANICAL ENGINEERING
COLLEGE OF ENGINEERING
ROCHESTER INSTITUTE OF TECHNOLOGY

JULY 2004

Proof of Concept Design and Analysis of Active Flow Control of A Supersonic Micro-Nozzle

Proof of Concept Design and Analysis of Active Flow Control of a Supersonic Micro-Nozzle

ABSTRACT

Low Reynolds number supersonic nozzles have been studied for several years due to their significance in applications in micro-spacecraft. As satellite design reduces in mass and size, smaller more versatile propulsion systems will be required. In response to the need, a conical nozzle (expansion ratio of 25 and 20° half-angle of divergence) with throat dimensions of 600μm x 300μm has been designed and fabricated with capabilities in thrust magnitude control. The device utilizes the expansion of a silicone membrane, located on the upper surface of the supersonic micro-nozzle throat, as a mechanism to reduce the throat cross sectional area, and consequently vary the nozzle's expansion ratio.

The flow through the nozzle, with and without flow control, has been modeled using an analytical one-dimensional isentropic model and a viscous three-dimensional computational fluid dynamics (CFD) model using FLUENT. The ability of the proposed flow control device to affect the flow rate, nozzle efficiency, and thrust output has been determined using CFD. The micro-nozzle has been tested under separation conditions; under these conditions the nozzle performance has been experimentally determined. Furthermore, successful flow control has been demonstrated. Possible future developments for this flow control concept are discussed, which primarily include improvements in fabrication and experimentation techniques.

This Thesis is dedicated to my parents Stanley and Sheila.

Thank you for your love, support, and example. It has made me who I am, and has made this work possible.

Acknowledgements

I would like to thank my advisor Dr. Kozak for his guidance over the past two years. His ability to direct me in my work while letting me discover, explore and critically choose between project concepts, has not only helped me produce the work presented here, but has certainly helped me mature as an engineer. I would also like to thank Dr. Lynn Fuller and Dr. Surendra Gupta for all their help with lab work and equipment. Their generous donation of time, equipment, and ideas significantly contributed to the quality of this work. Finally, I would like to thank Dave Hathaway, who was forever willing to lend his time whenever he had the opportunity.

I would like to thank my parents for their support throughout my life and education. Without the work ethic instilled in me by my parents I would have never been able to accomplish this. I would also like to thank all my friends who were there to bounce an idea off of, or to just hang out and relax. Finally, I would like to thank my girlfriend and best friend Cristy, who listened to my aggravations, was understanding of the long hours spent at school, and always supportive of my work.

Table of Contents

List of Illustrations

List of Tables

List of Equations

List of Symbols

A	Nozzle Cross-Sectional Area
AFC	Active Flow Control
M	Mach Number
u	Fluid Velocity
a	Outer Radius of Membrane
q	Unit Lateral Pressure
y	Maximum Deflection
σ_b	Bending Stress
σ_d	Diaphragm Stress
σ	Maximum Stress
ν	Poisson's Ratio
t	Thickness of Membrane
E	Modulus of Elasticity
Re	Reynolds Number
ρ	Density
d	Throat Width
μ	Viscosity
Kn	Knudsen Number
λ	Mean Free Path
l	Characteristic Length
γ	Specific Heat Ratio
P_o	Total Pressure
P	Static Pressure
Subscript t	Throat Property
V	Velocity
τ	Thrust
N_{ISP}	Specific Impulse Efficiency

1 Introduction

The following section will describe the motivation of the current study. The benefits of the current work and its applications will be discussed. An introduction to supersonic flow theory will be presented as well. The next section in this chapter will provide information on prior research, which is applicable to the current study. This section will discuss previous research in the areas of Microelectromechanical Systems (MEMS) actuators, micro-nozzle investigations, and active flow control of small jets.

1.1 Motivation

The control of micro-flows is currently a significant area of research. It has attracted attention due to the multitude of applications. It has applications in trailing edge blowing, mixing, cooling/heating, drying, spraying, printing, and thrusting. More specifically the current study is an investigation into a method to provide active flow control to a supersonic converging-diverging micro-nozzle. The results of this investigation are most applicable to micro-thrusting.

Thrusting on this scale (throat widths of 1 mm or less), which is primarily applied to satellites, is an important application of thrust magnitude control. There is an ever increasing demand for lightweight solutions in satellite propulsion systems. This is due to the highly weight dependant launch costs. Currently launch costs can range from $10,000-$100,000 per kg of spacecraft at launch (Janson et al., 1998). Batch fabricated propulsion and integrated systems are of high interest for their weight savings and low fabrication costs. Batch fabricated micro-flow control devices would also provide weight savings by eliminating the need for multiple thrusters. Thrust control would provide micro-satellites with more accurate control with fewer thrusters than is currently required. This is the motivation for the work presented in this study.

Table 1.1 shows a current list of microspacecraft that are in use, awaiting launch, or in the design phase (Meuller et al., 2003). These satellites will need lightweight propulsion systems. It is estimated that for 1-20 kg spacecraft in orbit, attitude control requirements may range between sub-mNs and up and 10^{-4} Ns impulse bits. Also, there may be a need for propulsion systems which require higher thrust for missions that require fine pointing and significant slews (Meuller et al., 2003). These requirements can be met if a thrust magnitude

control system is in place, allowing the thrust output to be varied without requiring multiple propulsion systems.

Designation	Lead	Mass (kg)	Size (cm)	Power (W)	Voltage (V)
MightySat	USAir Force	64	48x69	<=32	-
Micro-Bus 70	Surrey Space Centre. U. of Surey England	40-70	35x35x65	21-43	12
Orsted	Danish Space Research Inst.	60.7	68x45x34	54 (EOL)	
SNAP-1	Surrey Space Centre. U. of Surrey England	6.5	34x23	4 (avg.) 7 (peak)	7-9
New Millennium ST-5	NASA Goddard Space Flight Center	20	42x20 (Flat-to-Flat)	7.5-8.5	5/0.25
PROBA	ESA	100	60x60x80	9	28
Folconsat	USAir Force Academy	50	46x46x43	24	12
ASU Sat 1	Arizone St. U	5	31x24	8.5-10	13
University Nanosat Program					
3-Corner Sat	Arizone St. U U. of Colorado New Mexico State U.	10	45x25	33	3.3-5
ION-F	Utah State U., U. of Washington, Virginia Polytech. Inst.	10/13	45x12/ 45x25	18	28
Emerald	Stanford U., Santa Clara U.	15	45x30	7	5/12
Constellation Pathfinder	Boston U.	1	20x14	1	
Solar Blade Heliogyro	Carnegie Mellon	5		28	

Table 1.1 - Overview of Current Microspacecraft (Meuller et al., 2003)

The current study investigates a method to vary the throat area of converging-diverging nozzles with throat widths on the order of 0.6mm (0.024 in). To this author's knowledge, this has not previously been investigated. The ability to modify the nozzle throat area allows for the output flow-rate and consequently thrust to be controlled. The ability to control this output thrust allows for a single nozzle to be used for multiple mission scenarios. For example, it would be possible to use a single nozzle for both minute attitude adjustments and significant corrections. The advantage of eliminating propulsion systems is a lower system complexity, as well as a reduced launch weight. Several different nozzle sizes would no longer be required; instead a single system could provide the necessary thrust output.

In the current study, a nozzle and actuation device will be presented and analyzed using analytical and numerical techniques. The actuation has been analyzed using the ANSYS finite element analysis software package. The viscous flow through the supersonic nozzle has been analyzed using an isentropic analysis. It has also been modeled using the FLUENT computational fluid dynamics (CFD) software package. Flow through the designed nozzle with and without flow control has been modeled to determine the effects of the flow control device on the output thrust, flow-rate and nozzle efficiency. A proof of concept device has been built, tested, and compared with the CFD analysis.

1.2 Background and Literature Review

1.2.1 Supersonic Nozzle Flow

In the current study, supersonic flow theory is being used to examine and design supersonic nozzles. In order to understand the effects of the mechanisms being used to influence the flow field, it is important to have an understanding of supersonic flow behavior. More specifically, supersonic flow through nozzles must be understood. The supersonic nozzles used in the current study are converging-diverging nozzles. Due to the complexity of supersonic flow theory, the analysis completed in this study will use the assumption of one-dimensional isentropic flow. This assumption states that the flow through the nozzle is both reversible and adiabatic, which implies there are no losses due to heat transfer or frictional effects. It will also be assumed that the fluid starts at rest within a large plenum and is accelerated through the nozzle due to a pressure difference across the nozzle. Figure 1.1 will be used to explain the behavior of the flow field through a converging-diverging nozzle under changing pressure conditions. In an isentropic analysis the behavior or performance of the nozzle is primarily dependant upon two criteria; the pressure ratio across the nozzle, and the nozzle's geometry.

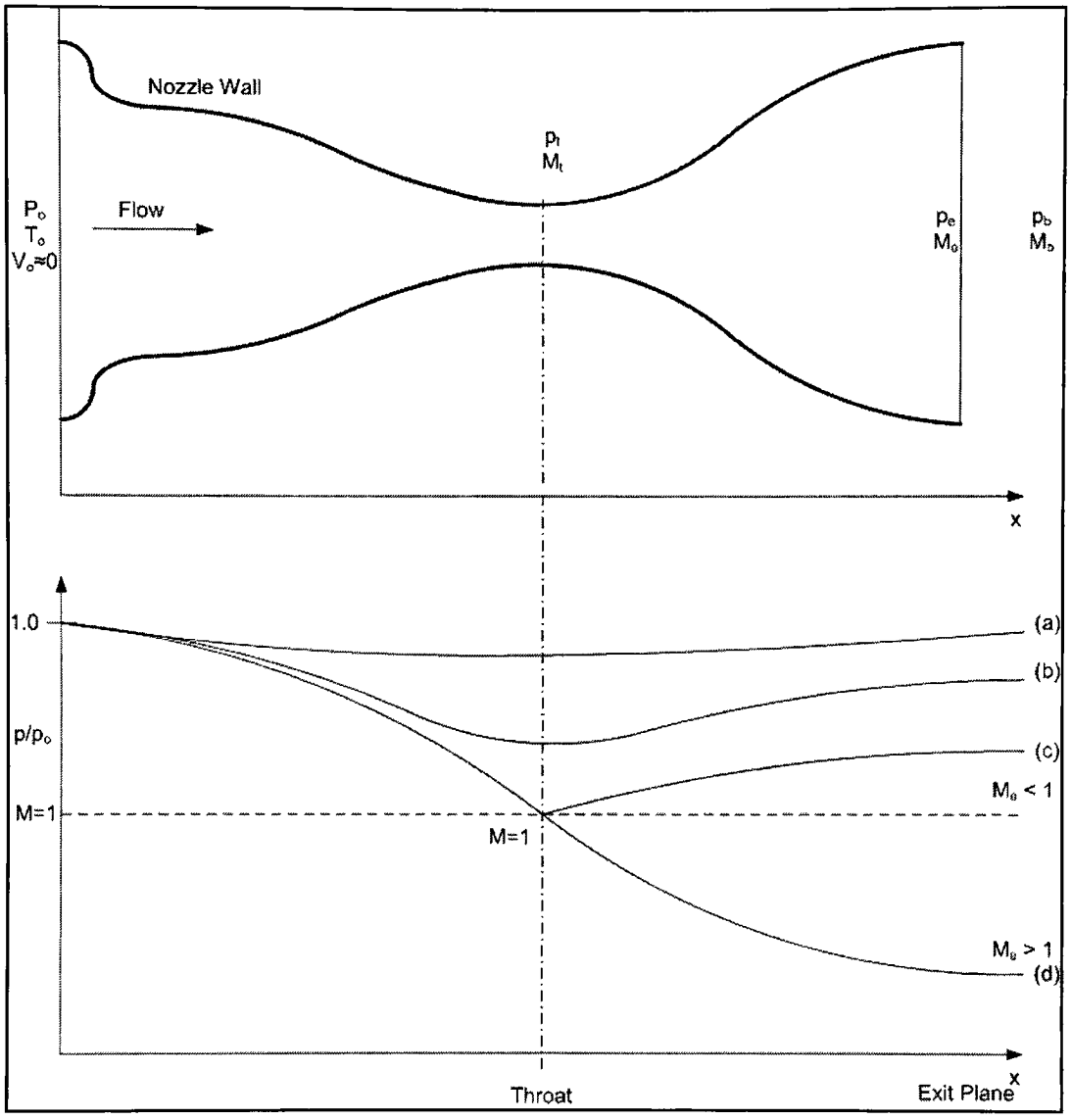

Figure 1.1 - Converging - Diverging Nozzle Flow (Fox & McDonald, 1998)

The upper portion of Figure 1.1 represents a converging-diverging supersonic nozzle. The lower graph is a representation of the flow pressure with respect to location within the nozzle. In all cases the fluid enters the convergent section of the nozzle and accelerates due to the decrease in the cross-sectional area of the nozzle. Case (a) and (b) shown in Figure 1.1 represent a condition where the back pressure is not low enough to permit supersonic flow. The flow accelerates until it reaches the throat, then as the nozzle diverges, the increasing area causes the flow to slow down. In case (c) the pressure difference across the nozzle is

large enough and the inlet to throat area ratio is high enough to permit the fluid to reach a choked condition at the nozzle throat. A choked condition implies that the fluid has reached a Mach number of one. Assuming that the plenum or stagnation conditions do not change, the mass flow rate at this choked condition is the maximum mass flow rate possible, regardless of the back pressure. Furthermore, the flow at the throat cannot accelerate beyond a Mach number of one. Equation 1-1 shown below relates the change in flow velocity through a supersonic nozzle to the nozzle's area change.

$$\frac{dA}{A} = \left(M^2 - 1\right)\frac{du}{u}$$

Equation 1-1 (Anderson, 2001)

Equation 1-1 is developed using isentropic relations. Upon examination of this equation it can be observed that for a Mach number less than one, a decrease in nozzle cross-sectional area is associated with an increase in flow velocity. Conversely, for a Mach number greater than one, an increase in nozzle cross-sectional area is associated with an increase in the flow velocity. This relationship is very important because it provides insight into a nozzle's behavior based on geometric considerations. This equation provides mathematical reasoning into the advantages of a converging-diverging supersonic nozzle. Once the flow has reached a choked condition it is possible for the flow to accelerate through an expansion, if an adequate pressure ratio is present.

Case (d) is an ideal operating condition where the back pressure is at a value that permits an isentropic acceleration to supersonic speeds. The fluid accelerates from zero to a Mach number of one at the throat and continues to accelerate isentropically through the divergent section of the nozzle. This implies no losses incur due to heat transfer or frictional effects. There is only one back-to-plenum-pressure ratio that will produce this flow. If the back pressure is even slightly lower than that in case (d), the nozzle is said to be under-expanded. This implies that the given nozzle geometry did not provide the expansion necessary to accelerate the fluid to a speed which would allow the nozzle's exit pressure to equalize with the outside back pressure. When this occurs, expansion waves will be present at the nozzle's exit plane. These expansion waves provide the proper expansion to decrease

the exit pressure, yielding pressure equilibrium between the nozzle's exit pressure and the outside back pressure. Conversely, if the back pressure is slightly above that shown in case (d) in Figure 1.1, the nozzle is said to be over-expanded. In this case the fluid within the nozzle is expanded to a speed that results in an exit pressure lower than the back pressure. In order for these pressures to reach equilibrium, oblique shocks will occur at the nozzle's exit plane. These shocks will slow the flow to a lower supersonic speed, consequently increasing the exit pressure.

The final cases to be discussed here occur when the back pressure is significantly higher than the back pressure in case (d) and lower than the back pressure in case (c). In this instance the fluid will accelerate to a choked condition at the throat. The fluid will then expand during the divergent section of the nozzle providing supersonic fluidic speeds. This acceleration creates a large pressure discontinuity between the fluid pressure within the nozzle and the back pressure. This pressure discontinuity produces a normal shock within the nozzle's divergent section. This shock slows the flow from supersonic to subsonic speeds and produces irreversible losses to the energy of the fluid. For this reason these operating conditions are undesirable. By avoiding this condition the nozzle will operate far more efficiently and safely.

The basic nozzle design and analysis used in this study will utilize the concepts introduced here. A more comprehensive description of the analysis is contained within Chapter 2 of this report.

1.2.2 Micro-nozzles

The term micro-nozzle has not been given a specific definition in terms of nozzle size. In this study, the term micro-nozzle will be used to describe nozzles with a wide range of throat dimensions. It will be used as a more general term to describe nozzles that have throat dimensions of 5mm or less, or are considered to operate at low Reynolds numbers. Nozzle flows are considered to be low Reynolds number flows if the Reynolds number is below 5,000 (Rothe, 1970). Due to the small scale of these devices and the consequently low Reynolds number flow, performance is a significant concern. As boundary layer buildup occurs in this flow regime, a shock-free transition to subsonic flow is possible in the

divergent section of the supersonic nozzle. Also, the assumptions made in the analysis of macro-flows may not be applicable within this flow regime.

The previous work completed in this area has been concerned with the performance of nozzles with constant expansion ratios, or in other words nozzles with fixed throat-to-exit-area ratios. A displacement thickness has been established; a measure that provides a method to quantify the boundary layer buildup within the nozzle. Furthermore, discharge coefficient and other nozzle efficiencies have been the focus of previous studies. To this author's knowledge no studies have addressed the possibilities of thrust magnitude control of micro-nozzles. The following published studies approach the performance concerns mentioned above for constant expansion ratio micro-nozzles.

CORNELL AERONAUTICAL LABORITORY, (ROTHE, 1970)

Rothe completed one of the first studies of low Reynolds number supersonic nozzles in 1970. The purpose of the study was to examine the flow inside low Reynolds number nozzles to determine how viscous effects influenced the nozzle flow. Electron-beam studies were completed providing gas temperature and density measurements throughout the nozzle's divergent section. Two axis-symmetric conical nozzles with diverging half angles of 20^{o} and throat diameters of 5mm and 2.5mm were tested. The maximum area ratio was 66 for both nozzles. The nozzle Reynolds numbers tested ranged from 100 to 1500.

Rothe showed that for Reynolds numbers less than 300 the temperatures reached a minimum inside the nozzle and increased towards the nozzle exit. For a Reynolds number of 110 the temperatures measured at the nozzle exit were above the sonic temperature for adiabatic flow. The data showed that the flow first accelerates above sonic conditions, but becomes subsonic by the time the flow reaches the nozzle exit through a shock-free viscous transition. This is the first time this phenomenon had been observed. This is significant; because it provides evidence of dominate viscous effects in this low Reynolds number flow regime. In this case the boundary layer filled the entire exit area. At Reynolds numbers above 500 the temperature profiles decreased throughout the entire length of the nozzle as inviscid theory predicts. Rothe also showed, through density measurements along the nozzle's centerline, that as long as the total to free stream pressure ratio produced an under-expanded jet there was no measured difference in the flow properties. The radial density profiles

allowed another important conclusion to be drawn. These profiles showed that the flow becomes fully viscous by the time the flow reaches the nozzle exit. That is, no uniform core flow exists.

This study was the first to provide a better understanding of viscous dominated supersonic nozzle flows. This is significant, because in high Reynolds number flows, the boundary layer region has little effect on the nozzle's performance. Due to the size and operating conditions of the nozzles investigated in the current study, Rothe's work provides insight into possible flow behavior. However, this study did not investigate the effect of nozzle geometry on the performance of nozzles within this flow regime.

NASA, (GRISNIK & SMITH, 1987)

Grisnik and Smith performed both an analytical and experimental analysis of low Reynolds number nozzles. The analytical analysis was accomplished using a two-dimensional kinetics nozzle program (TDK) version 2.5, December 1984. The program assumed a frozen chemical composition, no loss of mass from the system, perfect gases, axis-symmetric flow, and a compressible fluid. One-dimensional, non-equilibrium flow relations were used to calculate the behavior of the flow during the converging section and throat of the nozzle. Then, using these throat conditions the Method of Characteristics (MOC) was used to determine the flow properties in the divergent section of the nozzle. A boundary layer analysis was then performed to account for the viscous losses. The loss of performance due to the viscous effects was calculated and subtracted from the inviscid performance obtained from the MOC analysis. To quantify the boundary layer build up at these low Reynolds numbers a displacement thickness was established, defined as the distance the solid nozzle boundaries would have to displace in order to maintain the predicted inviscid mass-flow rate. Using this analysis the three nozzle geometries shown in Figure 1.2 and a modified trumpet geometry (not shown) were analyzed.

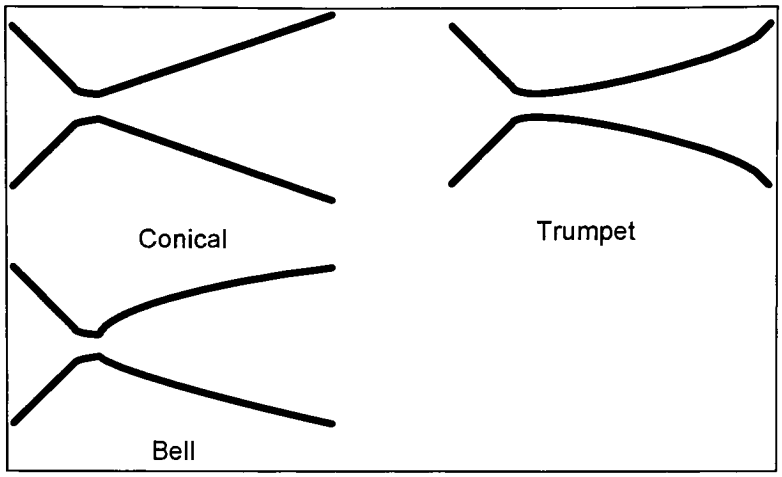

Figure 1.2 - Nozzle Geometries (Grisnik & Smith, 1987)

The displacement thickness at a Reynolds number of 4000 for the conical nozzle was about 40% of the exit plane, 37% for the bell nozzle, and 67% for the modified trumpet nozzle according to the TDK analysis. The TDK analysis also provided thrust coefficient results.

The experiments by Grisnik and Smith were conducted in a vacuum environment using unheated nitrogen and hydrogen. The purpose of the tests was to determine the viscous losses incurred for low Reynolds number nozzles of various divergent nozzle contours. The nozzles evaluated were axis-symmetric converging-diverging nozzles each with different diverging contours. The four geometries are described below in Table 1.2.

Nozzle	Shape	Exit Half-angle		Throat Diameter	Area Ratio
		Throat	Exit Plane	mm	
1	Conical	20°	20°	0.653	120:1
2	Bell	35°	20°	0.711	150:1
3	Trumpet	0°	36°	0.671	125:1
4	Modified Trumpet	15°	28°	0.64	135:1

Table 1.2 – Nozzle Geometries (Grisnik & Smith, 1987)

For each nozzle tested the thrust, inlet gas pressure, inlet gas temperature, test cell pressure, and mass flow rate data was taken over the Reynolds number range of 500 to 9000. Table 1.3 shows the results of this testing at a Reynolds number of 1000. The discharge coefficient is the ratio of the measured flow rate to the theoretical flow rate, while the specific impulse

coefficient is the ratio of the measure specific impulse to the theoretical maximum specific impulse. The thrust coefficient was calculated using Equation 1-2.

$$C_F = 1.7 C_D N_{ISP}$$

Equation 1-2 - Thrust Coefficient (Grisnik & Smith, 1987)

Nozzle	Shape	Discharge Coefficient, C_D		Specific Impulse efficiency, N_{ISP}		Thrust coefficient, C_F	
		Nitrogen	Hydrogen	Nitrogen	Hydrogen	Nitrogen	Hydrogen
1	Conical	0.87	0.88	0.80	0.78	1.18	1.17
2	Bell	0.91	0.92	0.85	0.75	1.31	1.17
3	Trumpet	0.88	0.86	0.83	0.78	1.24	1.14
4	Modified Trumpet	0.93	0.93	0.84	0.76	1.33	1.20
-	Orifice Plate	0.98	0.94	0.58	0.59	0.97	0.94

Table 1.3 – Results (Grisnik & Smith, 1987)

The authors discovered that the discharge coefficient is highly dependant on the ratio of nozzle throat radius of curvature to the nozzle throat radius even in this low Reynolds number flow regime. As this ratio increases so does the discharge coefficient. The thrust data showed a significant divergence from the isentropic predictions, suggesting that a large boundary layer existed within the nozzles. These experimental results were then compared with the TDK analysis. The TDK analysis proved to be unreliable and inaccurate. The authors concluded that the TDK code must be modified to more consistently reach converging properties at the throat for the low Reynolds number flow regime. They also concluded that at such low Reynolds numbers the method of subtracting the viscous effects from the inviscid performance is inaccurate. These conclusions provide further understanding of low Reynolds number nozzle flows.

MIT, (BAYT & BREUER, 2001)

MIT has also been involved in the design, fabrication, and testing of supersonic micro-nozzles. Bayt and Breuer designed and fabricated three-dimensional nozzles by enclosing a two dimensional nozzle profile between two plates of glass to form the upper and lower nozzle boundaries. The nozzle profiles were constructed from silicon using Deep Reactive Ion Etching (DRIE), an etching process that maintains a high level of anisotropy. This

process produces a straight wall etch capable of producing nozzle profiles with a sub-micron surface roughness, and minimal feature variation along the depth of the etch. Upper and lower glass plates were then anodically bonded to the silicon, which resulted in a seal demonstrating yield strengths higher than that of the parent materials. The upper boundary was predrilled to accept tubing to provide the nozzle's inlet and exit. The smallest nozzle fabricated had throat dimensions of 308μm x 18μm.

Testing was completed inside a vacuum where flow rate and thrust data were taken and compared with a two-dimensional finite volume Navier-Stokes simulation. Sonic flow was achieved, and a maximum average exit Mach number of 3.8 was demonstrated. Similar trends were shown between the experimental data and the theoretical results, but the actual nozzles' performance degraded more quickly than the theoretical model predicted. Bayt and Breuer believed this was likely due to the three-dimensional effects of the upper and lower glass boundaries, which were not modeled. The three-dimensional nozzle tested and analyzed in this study closely resembles the nozzles investigated in the current study. However, Bayt and Breuer did not investigate varying throat area or geometry.

CHOUDHURI, BAIRD, GOLLAHALLI, AND SCHNEIDER, 2001

Choudhuri examined the flow through optically accessible flat nozzles with conical, bell, and trumpet shaped diverging sections. The study investigated the effect of exit geometry on the performance of nozzles with small throat dimensions and a three dimensional configuration (flat nozzle). An investigation in the performance while varying propellants was also completed in this study, but will not be discussed here, as it does not pertain to the current study. Color Schlieren Defectometry was used to visualize the flow inside the nozzles, while thrust and flow rate data was taken to examine nozzle performance.

Parameters	Dimension			
	15° Nozzle	20° Nozzle	Bell Nozzle	Trumpet Nozzle
Throat Width	0.38 mm	0.38 mm	0.38 mm	0.38 mm
Expansion Ratio	25	25	25	25
Nozzle Half Divergence Angle	15°	20°	Rao Optimized	-
Chamber Length	7.5 mm	9 mm	7.5 mm	7.5 mm
Convergence Section Length	2.5 mm	2.5 mm	-	-
Divergence Section Length	13.5 mm	10 mm	13.5 mm	13.5 mm
Thickness	4.7 mm	4.7 mm	4.7 mm	4.7 mm

Table 1.4 – Nozzle Geometry (Choudhuri et al., 2001)

Nozzle dimensions are given in Table 1.4. The nozzle profiles were fabricated in oxygen-free copper using an Electron Discharge Machining (EDM) technique. Images, thrust, and pressure data was taken for each of the nozzle geometries. The testing was completed with the nozzles exhausting to atmosphere. Due to the high expansion ratio of the nozzles tested, and the inability to provide the high pressure ratio required across the nozzle, the flow in the nozzle's divergent portion exhibited separation. In the Schlieren images the separation or formation of a diamond shock pattern can be seen. It was noted that as the chamber pressure increased, the shocks moved downstream. This behavior was expected, but the separation in the 15° conical nozzle occurred farther downstream of the throat than in the other nozzle geometries. Choudhuri explains that this behavior is due to the more gradual slope of the nozzle wall, which counteracts the adverse pressure gradient. The conical, trumpet, and bell nozzles all performed comparably at low chamber pressures. As the pressure increased, the bell nozzle produced a significantly lower thrust and specific impulse, which is likely due to

separation caused by the inability of the fluid to follow the sharp turning angle. The 15° half-angle conical nozzle performed the best under the testing conditions.

It was noted that the flow separation did not occur symmetrically across the nozzles' diverging sections. A possible explanation for this behavior is perturbations from small imperfections within the throat area are disrupting the flow. Choudhuri suggests that because of this, the assumption of symmetric flow may no longer be valid for devices at this scale, where such imperfections may be inherent in the fabrication process. The nozzle investigation completed by Choudhuri played a considerable role in the nozzle geometry selection for the nozzle investigated in the current study. Furthermore, the current study is also using a three-dimensional flat nozzle at non-ideal operating conditions; therefore the experimental results from this study will be used as a basis for the CFD model constructed in the current study.

1.2.3 Flow Control

Active flow control (AFC) refers to the ability to control a flow, but the term is commonly used to describe the use of a small disturbance to produce a change in a larger flow field. The term is used in this study to describe the ability to control the properties of a small scale free jet. To this author's knowledge only two major approaches have been investigated to achieve flow control in this sense. First, flap actuators have been used to affect a jet shear layer to produce a large alteration in the downstream flow. Secondly, synthetic jet actuators or zero-mass flux control jets have been located in the shear layer at the exit of a larger free jet to turn or vector the larger flow field.

The studies described in this section present the latest work in the area of flow control most applicable to the current study. The nozzle throat dimensions on which the following studies perform flow control are 30 times greater than the current study's nozzles. However, to this author's knowledge, these are the smallest scale investigations completed.

THE UNIVERSITY OF TOKYO, (SUZUKI, H., KASAGI, SUZUKI, Y., & SHIMA, 1999)

Copper plated polyimide film was used to create electromagnetic actuators, which were used to excite the shear layer of a jet to achieve active jet control. The actuators fabricated and tested were 9mm (0.354 in) in length and 3mm (0.118 in) in width. The whole assembly was 60μm (0.002 in) thick. Eighteen of these actuators were mounted on the exit of a 20mm (0.787 in) diameter jet. Each of the actuators was driven independently from a multi-channel digital-analog board. The testing was completed using a converging nozzle with a 42 : 1 contraction ratio. The working fluid was water impregnated with die to allow flow visualization, while a two-component fiber laser Doppler velocimetry (LDV) was employed to measure the transverse and longitudinal velocity components of the jet flow. The actuators were driven in three modes; synchronously by a square wave signal of f = 4Hz, a spiral movement with f = 1.6 Hz combined with an axial movement at f = 3.2 Hz, and out of phase with square wave signals at 1.6 Hz.

From the synchronously driven actuators, axis-symmetric vortex rings with regular spacing were formed, the spiral movement produced vortex rings that were alternately displaced off the jet axis, and driving the actuators out of phase caused the jet to spread in all radial directions. When the actuators were driven out of phase the centerline velocity dropped to about 45 % of the natural jet's centerline velocity for the velocity measurements made at x/D = 6. However, even though the system successfully modified the flow field significantly, the efficiency of the flap actuator itself was very low, and the overall power consumption was 0.18W. Furthermore, the system described here uses actuators on the scale of several millimeters. The current study is investigating a flow control device, which modifies a jet whose largest linear dimension is on the order of several hundred microns.

UNIVERSITY OF MICHIGAN, (CHRISTOPHOROU ET AL., 2000)

Electrostatic actuators have been fabricated and tested, and have survived operations at speeds greater than 210m/s. These actuators have been integrated with piezoresistive sound detectors to provide jet screech detection. The micro-actuators were mounted on the edge of a 1-inch diameter nozzle. A PC board and function generator was used to drive the actuators as well as monitor the actuators' operation. It was shown that the MEMS devices excited the macro level flows to levels equivalent or greater than those achievable through large-scale

forcing. The devices in this study were not applied to "micro" scale jet flow as the current study is addressing.

LOS ALAMOS NATIONAL LABORATORY, (SMITH & GLEZER, 2002)

Smith and Glezer completed a study of jet vectoring using synthetic jets. The jet vectoring was completed on a jet with a cross-sectional area size of 12.7mm (0.5 in) x 76.2mm (3.0 in). The synthetic jet orifice measured 0.51mm (0.02 in) x 76.2mm (3.0 in) and was mounted on the upper surface of the larger jet exit plane. A drawing of a synthetic jet is shown in Figure 1.3 below. A synthetic jet works through the deflection of an actuator that drives a diaphragm. The diaphragm movement creates suction and blowing so there is zero net mass flow, but the outward jet is more directed than the jet during suction.

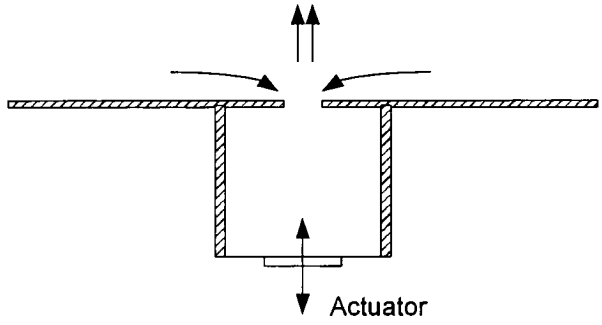

Figure 1.3 - General Synthetic Jet (Smith & Glezer, 2002)

In this study the flow was analyzed using both Schlieren imagery and particle image velocimetry. From these visualizations it was evident that the larger flow field was directed by the introduction of the synthetic jet; however the magnitude of the flow's thrust was largely unaffected. The purpose of the current study is to vary the output thrust of a converging-diverging nozzle, not to vary the thrust direction. Furthermore, this study achieved flow control on a much larger free jet than the one investigated in the current study.

1.2.4 MEMS Actuation Types

In the current study a valve or actuator must be used to provide the displacement necessary to vary the throat area of the micro-nozzle. This actuator must be able to handle high operating pressures, and simply fit into the overall system. Several actuation types were considered. Each will be discussed in the following section.

THERMOPNEUMATIC ACTUATORS

Thermopneumatic actuators use the expansion of a fluid to provide the force necessary to create displacement. This type of actuator is utilized in a commercially available valve through Redwood Microsystems Corp., and uses a refrigerant as the working fluid (Zdeblick et al., 1994). The fluid is heated through a resistive heater, which thermally expands the fluid causing a diaphragm to displace. This type of actuator can handle high forces and high pressures, but has a slow response time. Figure 1.4 below shows a drawing of the Redwood valve that utilizes this type of actuator. Several other valves of this type have been fabricated using a variety of membrane materials. For example Baechi and Buser have utilized a silicone material to reduce the cross-sections of micro-channels in a novel particle handling system (Baechi & Buser, 2000).

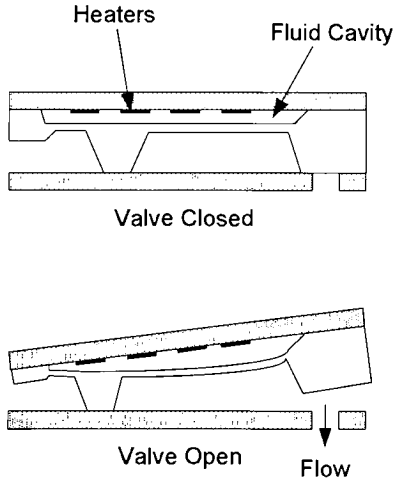

Figure 1.4 - Thermopneumatic Valve (Mueller, 1999)

BI-MORPH ACTUATOR

This actuator uses nickel and silicon together, taking advantage of their different thermal expansion rates. A Bi-morph valve has been developed by Hewlett-Packard and IC Sensors. A nickel layer is deposited onto a silicon membrane and both layers are heated. The nickel has a higher coefficient of thermal expansion than the silicon, which puts the nickel in tension. This expansion provides the deflection necessary to open the valve. Figure 1.5 shows a sketch of this valve type. The device for this type of actuation is fairly large, but can handle high pressures and has better response times than the thermopneumatic actuators.

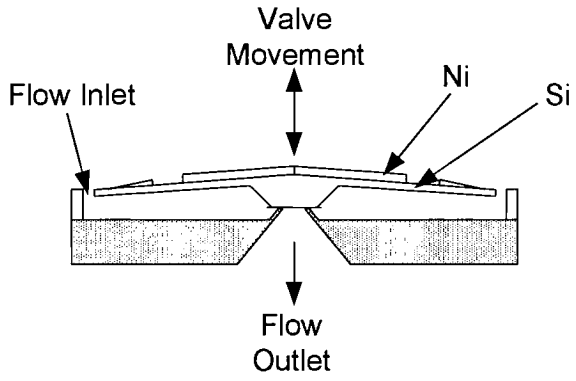

Figure 1.5 - Bi-Morph Valve (Mueller, 1999)

SHAPE MEMORY ALLOY ACTUATOR

Shape memory alloy actuators use Ti/Ni alloys that have the ability to return to a prescribed shape at a set transition temperature. The deflection of these actuators are dependant upon the anneal state during the fabrication of the device. This type of actuation device is advantageous due to its quick response time, large deflections, and ability to handle high pressures. The disadvantage of this type of actuation is the difficulty and cost of fabrication.

ELECTROSTATIC ACTUATOR, PIEZOELECTRIC ACTUATOR, ELECTROMAGNETIC ACTUATOR

These three actuation types are described by the type of force used to provide the desired deflections. Each of these actuators requires voltages greater than 20V and cannot provide deflections greater than several micrometers.

Table 1.5 below shows an overview of each actuation type and its rating for integration into a micro-spacecraft application.

	Thermo-pneumatic	Bi-morph	Shape Memory-Alloy	Electrostatic	Piezoelectric	Electromagnetic
Size and Weight	Excellent	Excellent	Excellent	Excellent	Excellent	Excellent
Power	Good	Good	Good	Excellent	Excellent	Excellent
Voltage	Acceptable	Unknown	Unknown	Poor	Poor	Acceptable
Cycle Time	Poor	Poor	Poor	Excellent	Excellent	Excellent
Pressure	Marginal	Marginal	Marginal	Poor	Unknown	Unknown
Leakage	Poor	Poor	Poor	Poor	Unknown	Unknown
Seating Pressures	Acceptable	Acceptable	Acceptable	Poor	Good	Good
Ratings: Excellent, Good, Acceptable, Marginal, Poor						

Table 1.5 - Actuator Evaluation For Micro-Spacecraft (Mueller, 1999)

2 Design of a Micro-Nozzle with Active Flow Control

2.1 Actuator Selection

The actuator selected for integration into a micro-nozzle device with active flow control (AFC) is critical for successful operation of the given system. The actuator must provide the necessary deflection and force to decrease the micro-nozzle's throat area significantly to affect the nozzle thrust and flow-rate. This is estimated as a deflection of approximately 50μm (0.002 in), assuming a nozzle thickness of 300 μm (0.012 in). Also, a significant amount of force will be required for the actuator to constrict a high pressure flow (689 kPa (100 psi)). Therefore the actuation type must be able to produce seating pressures of at least 689 kPa (100 psi) in a valve application. Furthermore, the actuator must be small enough to be used in a micro-nozzle device with throat dimensions on the order of 300μm (0.012 in) x 600μm (0.024 in).

The ideal application of this nozzle system is for integration into a micro or nano-spacecraft system. With this in mind, the actuation system selected must also be low power. In future spacecraft it is expected that the voltage available will be on the order of 5V. Furthermore a given device should not exceed 1 – 3 Watts of power consumption (Mueller, 1999).

Each of the actuation types considered is listed in Table 1.5. These represent the major methods of mechanical actuation on the small scale required for integration with the micro-nozzle. Each actuation type and its applicability to a micro-nozzle system are described on the following pages.

2.1.1 Electromagnetic Actuation

This type of actuation uses an electromagnetic force to displace a membrane or valve seat. Unfortunately, due to current fabrication limitations in micromachining, external coils or permanent magnets are typically used to provide the strong magnetic field required.

One example of this actuation type is a valve concept by DASA/Germany. A depiction of this valve is shown in Figure 2.1.

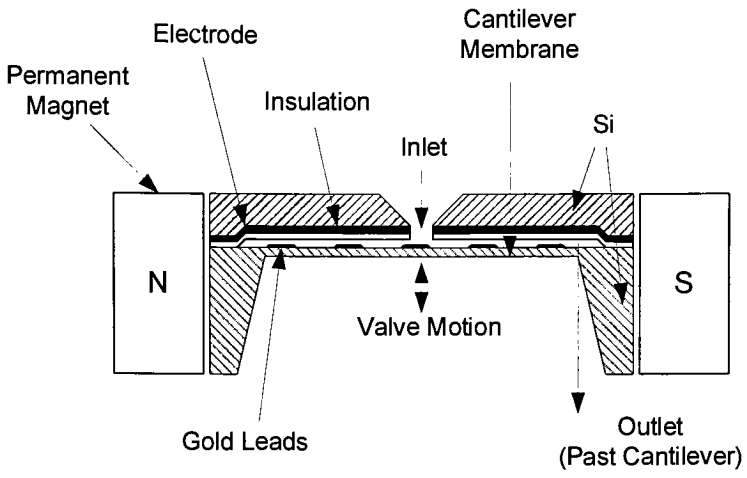

Figure 2.1 - Electromagnetic Valve (Mueller, 1999)

The movement of the valve seat is triggered by a current input to the gold leads, either into or out of the page depending on the desired motion. The current is fed through a magnetic field created by the external magnet, which creates an electromagnetic force on the membrane, causing it to deflect. Unfortunately, the electromagnetic forces are quite weak and the stroke is small. The seating pressures for the valve depicted above are on the order of about 14 kPa (2 psi), and the stroke is on the order of 10 – 15 μm (0.0004 - .0006 in) (Mueller, 1999). While the power requirements are low and the time response has been shown as less than 1 ms, the small stroke and low seating pressures eliminate its applicability to the application of interest in the current study.

2.1.2 Piezoelectric

Piezoelectric devices are still in development. They utilize piezoelectric materials, which when excited by a voltage produce a displacement. At this time these devices are only capable of producing small deflections on the order of several microns, and require high voltages on the order of 50 – 100 V. For these reasons this actuator type will not be pursued further in this study.

2.1.3 Electrostatic

Electrostatic actuators exhibit similar shortcomings of the piezoelectric and electromagnetic actuators. This actuation type also requires high voltages, and while the time response is short, electrostatic forces are too weak to be considered a viable option in the current application.

2.1.4 Shape Memory Alloy

Shape memory alloys, for example Ti/Ni alloys, are able to transform shape due to a phase transformation at a temperature set during the fabrication process. The stroke or displacement is also determined during fabrication. This actuation type is capable of producing large deflections while delivering a considerable force throughout the stroke. This type of actuation is also low power with power requirements ranging from 0.3 – 2 Watts (Mueller, 1999). The devices also can be made quite small, which would allow for their integration into the thrust vectoring device being investigated in the current study. Unfortunately, while this actuation type is suitable, the difficulties inherent in the fabrication of these devices are not easily overcome. A commercially available solution does not exist, therefore the device would have to be designed and fabricated. This task is not possible given the resources available, and therefore this actuation type will not be pursued further.

2.1.5 Bi-Morph

This actuator type takes advantage of the dissimilar thermal expansion coefficients of two different materials to provide the stroke. Figure 1.5 is a drawing of a valve that utilizes a bi-morph actuator. This type of actuation also satisfies the stroke, force, and power requirements specified. However, devices capable of providing large stroke lengths have dimensions on the order of a couple centimeters. Furthermore, due to resource limitations it would be difficult to complete the fabrication of this actuator type.

2.1.6 Thermopneumatic

Thermopneumatic actuators are capable of meeting all of the stroke, force, power, and size requirements specified. Furthermore, they are easily fabricated. This actuation type can also be used with a variety of working materials. For example, a number of valves have been fabricated that utilize both silicon and silicone membrane materials. For these reasons this actuation type will be pursued.

In the current study a silicone membrane material will be selected to allow for large membrane deflections. Also, a traditional thermopneumatic system will not be utilized. For simplicity the membrane will not be loaded by the thermal expansion of a heated fluid, but instead, the system will be pressurized by an external pressure source. While this is not ideal in a spacecraft application, it further simplifies the system in this proof-of-concept system. Later, studies could integrate a thermopneumatic actuator.

2.2 Design

2.2.1 Actuation Device

A silicone diaphragm located directly above the nozzle throat is being used to affect the nozzle flow through pressurized actuation. The size of this diaphragm is constrained by nozzle throat width as well as the desired deflection magnitude. The throat width of the nozzle is 0.6 mm (0.024 in), limiting the diameter of the diaphragm to this dimension. The actuation is achieved by pressurizing a sealed chamber with an external pressure source capable of a maximum pressure of approximately 689 kPa (100 psi). Therefore, the silicone thickness must be determined such that the desired deflection is possible given this pressure limitation. A Solidworks drawing of the device is shown in Figure 2.2

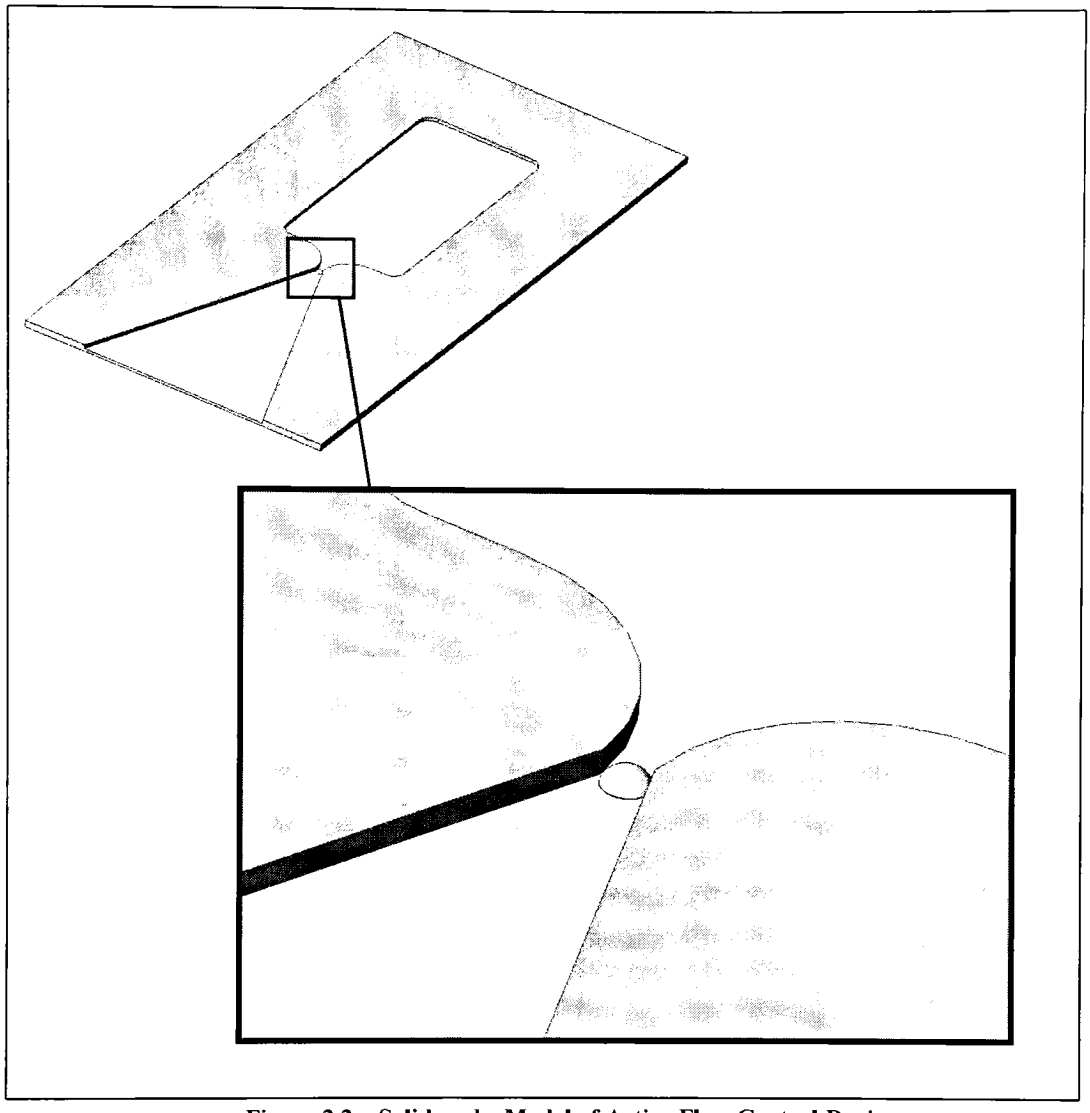

Figure 2.2 – Solidworks Model of Active Flow Control Device

2.3 Diaphragm Analysis

2.3.1 Analytical Flat Plate Analysis

Using analytical techniques a flat plate analysis of the diaphragm was completed. In order to permit the use of a manageable analytical model, several assumptions were necessary. The major assumptions are in relation to the silicone material. In both this analysis and the FEA analysis to be covered in Section 2.3.2 the silicone is treated as a linear elastic isotropic material. While this is not entirely correct due to the rubber nature of the silicone, it

affords the application of a more simplistic approach to the analysis. However, the material constants can be estimated using the Rivlin-Saunders strain-energy density function as shown by Kempski (Kempski et al., 1988). The ability to quantify the membrane's material properties under variable manufacturing processes (degassing) is a candidate for future investigations, but will not be addressed in the current study. Furthermore, the actuation process is unrefined, and therefore a more accurate membrane deflection model is unnecessary, as other factors would eradicate any accuracy gained by a more precise model. Therefore, the assumption of silicone as a linear elastic isotropic material will be used throughout this analysis. Also, the pertinent mechanical properties of the silicone will be assumed, as no concrete values are available due to variability in fabrication. Table 2.1 below shows several sources of values for the Modulus of Elasticity of silicone.

Material	Modulus of Elasticity (MPa)	Membrane Thickness (mm)	Source
MRTV I American Safety Technologies, Inc.	0.51	0.132	Yang, X., Grosjean, C., and Tai, Y., 1999
Dow-Corning Sylgard 184	1.5	0.003	Baechi, D., Dual, J., and Buser, R., 2001
Dow-Corning 96-083	0.7-1.0	0.029-0.107	Bousse, L., Dijkstra, E., and Guenat, O., 1996
Bisco Solid Silicone HT-6135	1.724	0.254	Rogers Corporation Technician

Table 2.1 - Modulus of Elasticity of Silicone

Two different silicones were pursued as possible membrane materials. Sylgard 184 from Dow-Corning and Bisco Solid Silicone HT-6135 were obtained. The Sylgard 184 comes in a two part liquid form that cures upon mixing. This type of silicone allows the membrane to be spun on to a substrate in varying thicknesses by varying the spin speed. The Bisco Solid Silicone HT-6135 comes in a sheet form with a least thickness of 0.254 mm (0.01 in). This is

a far simpler alternative, but thinner sheets are unavailable. This sheet silicone will be pursued due to its simplicity in application, but the membrane analysis will be completed for both this sheet and a thinner membrane of the Sylgard 184, which could possibly be used in future studies where greater deflections could be necessary. The material properties used in the analysis of each membrane are shown in Table 2.2.

Material	Modulus of Elasticity (MPa)	Poisson's Ratio
Dow-Corning Sylgard 184	1.5	0.45
Bisco Solid Silicone HT-6135	1.724	0.45

Table 2.2 - Silicone Mechanical Properties

Due to a lack of available material property data a Poisson's ratio of 0.45 was assumed. The silicone behaves similarly to that of rubber; therefore a Poisson's ratio of 0.45 was deemed a reasonable estimate.

The analytical model implemented in the analysis of the membrane assumes that diaphragm stresses occur due to large deflections. As a membrane's deflection exceeds half of its thickness, stresses in the middle portion of the diaphragm become significant, and therefore can no longer be ignored. This diaphragm stress causes the diaphragm to stiffen under large deflections, resulting in a non-linear load-deflection relationship. In the analysis of the sheet silicone this model is not necessary, but in the case of the Sylgard silicone this model becomes necessary. The Sylgard silicone membrane is thinner and the deflections are greater. The model presented below is for use with a circular membrane of linear elastic isotropic material. The following equations are implemented:

$$\frac{qa^4}{Et^4} = K_1 \frac{y}{t} + K_2 \left(\frac{y}{t}\right)^3$$

Equation 2-1 (Young, 1989)

$$\frac{\sigma a^2}{Et^2} = K_3 \frac{y}{t} + K_4 \left(\frac{y}{t}\right)^2$$

Equation 2-2 (Young, 1989)

The constants K_1, K_2, K_3, and K_4 are defined for varying edge and loading conditions. The boundary condition used in the current analysis is a fixed and held (clamped) boundary. The load being applied is due to an external pressure source, which is being modeled as a uniform pressure 'q' over the entire membrane. The constants are defined under this given edge and load condition as described in Equations 2-3 (a-d).

$$K_1 = \frac{5.33}{1-\nu^2} \quad \textbf{(a)}$$

$$K_2 = \frac{2.6}{1-\nu^2} \quad \textbf{(b)}$$

At Center: $K_3 = \frac{2}{1-\nu}, K_4 = 0.976$ **(c)**

At Edge: $K_3 = \frac{4}{1-\nu^2}, K_4 = 0.476$ **(d)**

Equations 2-3 (a-d) (Young, 1989)

Once the constants are found, Equation 2-1 must be solved for the deflection given the applied pressure. Using this information, the stresses at both the center and edge of the membrane can be found using the appropriate coefficients and Equation 2-2.

A simpler model, which does not include the effects of stress stiffening, is represented by Equation 2-4.

$$y_c = \frac{-qa^4}{64D}, \text{where } D = \frac{Et^3}{12(1-\nu^2)}$$

Equation 2-4 (Young, 1989)

The results shown in Figure 2.3 are obtained from the solution of the two models described above for the sheet silicone under an applied constant pressure from 0 – 650 kPa (0 – 95 psi).

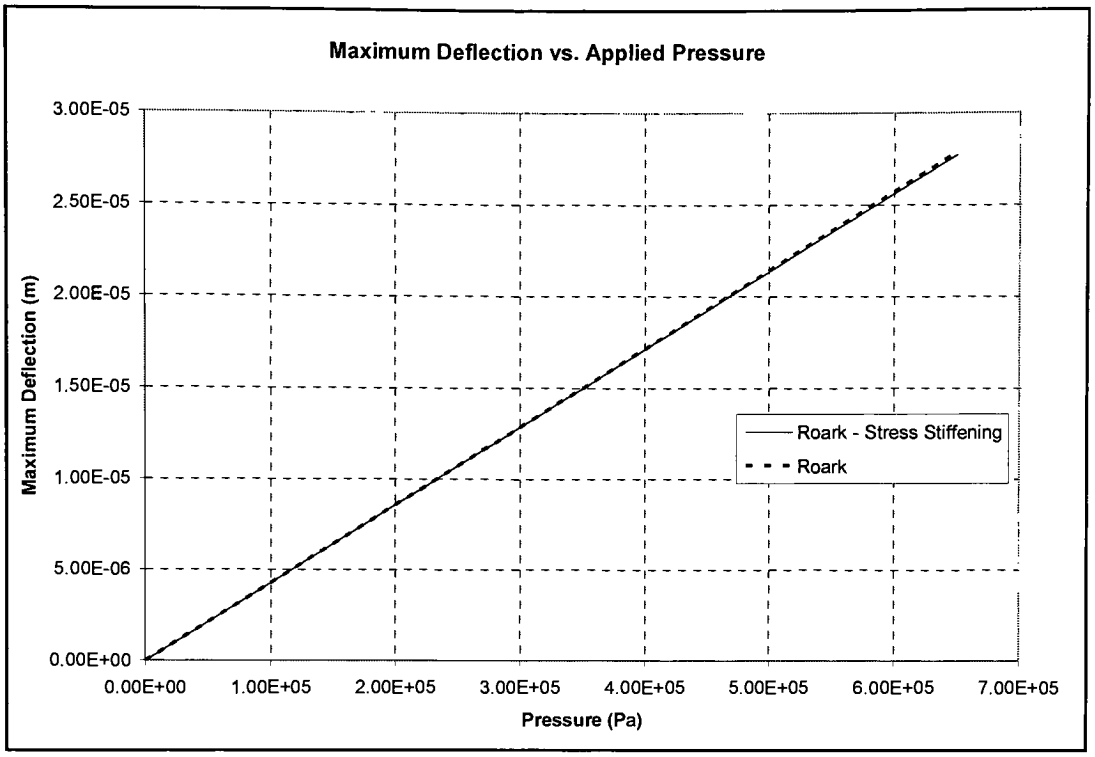

Figure 2.3 - Deflection Results for Sheet Silicone

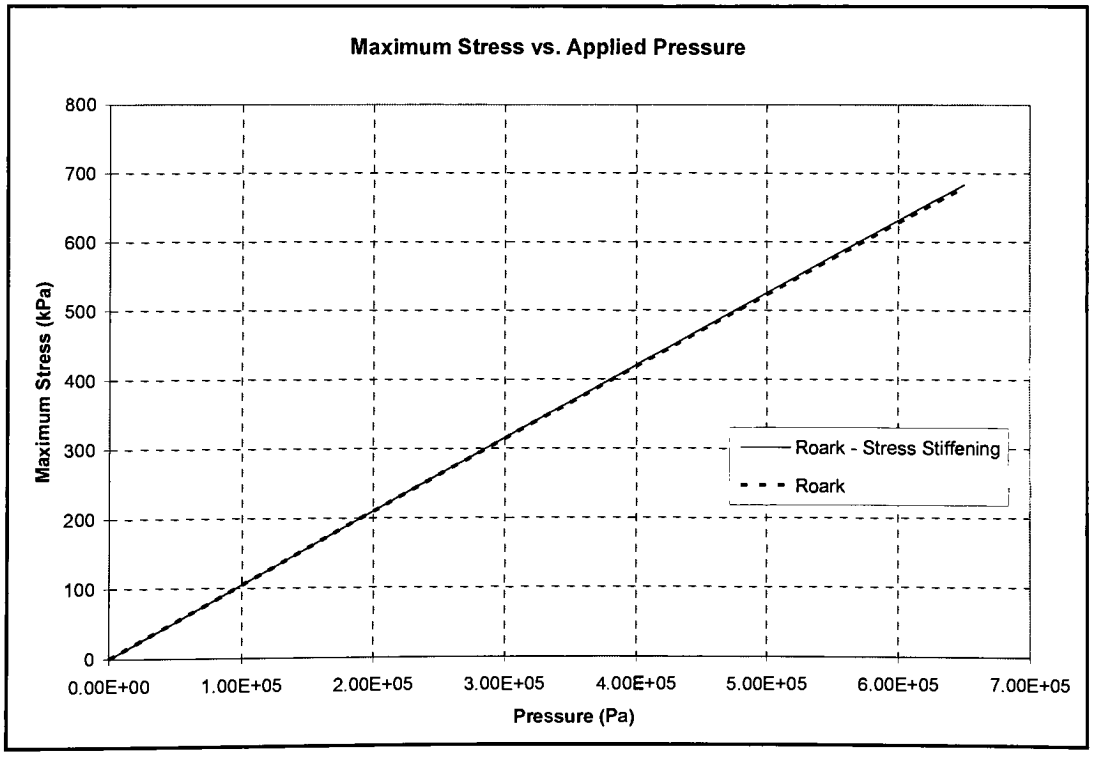

Figure 2.4 – Maximum Stress Results for Sheet Silicone

It is clear from the results presented in Figure 2.3 that the observation of the diaphragm stress in the membrane constructed of sheet silicone has little effect on the maximum membrane deflection. This same phenomenon can be seen in the plot of the maximum stress versus applied pressure shown in Figure 2.4. Once again the results for both models are similar. The maximum stress of the sheet silicone under the applied pressure is 684 kPa (99 psi). The maximum allowable tensile strength for this type of silicone is 5.5 MPa (797 psi), therefore the silicone has a factor of safety of approximately eight. Failure of the silicone should not be of concern. Even if the flow field exhibits the violent nature of a shock, the membrane should be upstream of the shock and therefore unaffected by the disturbance.

The results for the thinner silicone membrane of Dow-Corning Sylgard 184 however, are quite distinct depending upon the inclusion or exclusion of the diaphragm stress. The membrane thickness was set at 0.1 mm (0.004 in), the Modulus of Elasticity was set to 1.5 MPa (218 psi) and all other properties remained unchanged. The results obtained from the two analytical models are shown in Figure 2.5 and Figure 2.6.

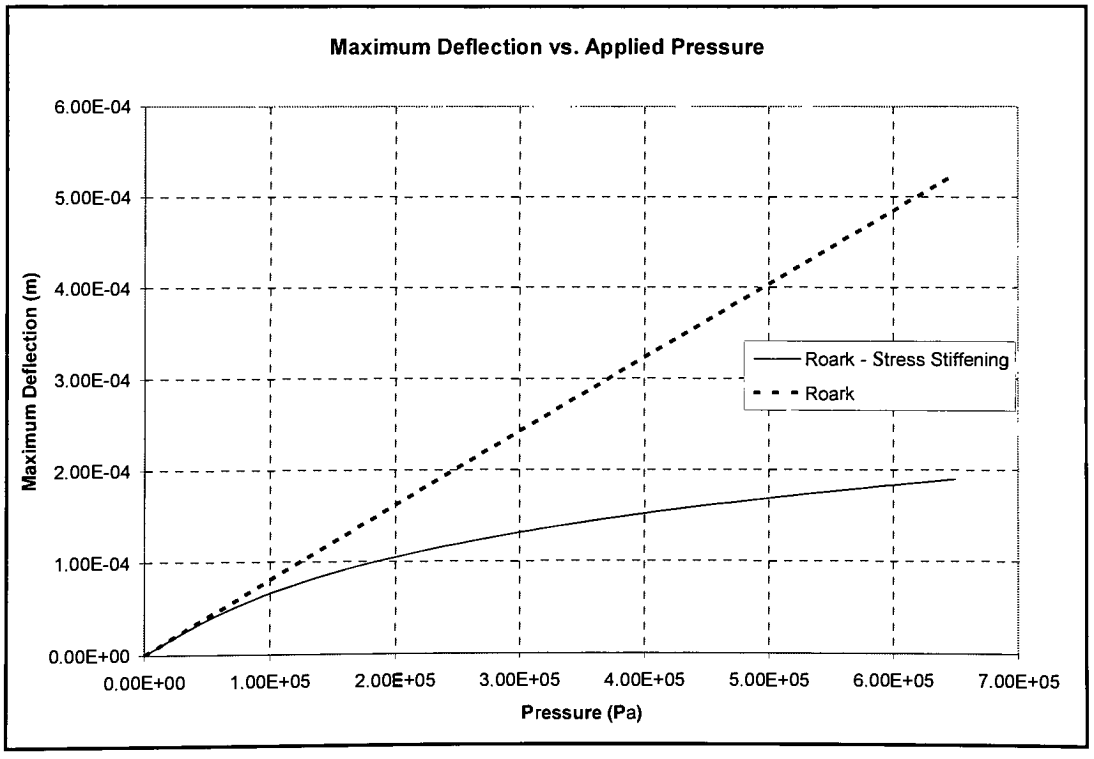

Figure 2.5 – Deflection Results for 100μm Thick Sylgard 184

For this thin membrane, the Roark model with stress stiffening is a more realistic model, as the maximum deflection is nearly four times the membrane thickness. The maximum deflection of this membrane under the largest pressure load is approximately 190 μm (0.0075 in). From Figure 2.6 it is clear that the membrane undergoes a maximum stress of nearly 2 MPa (290 psi). The tensile strength of the Sylgard 184 is 7.1 MPa (1030 psi), so even under this large pressure load, the factor of safety for the membrane is 3.6.

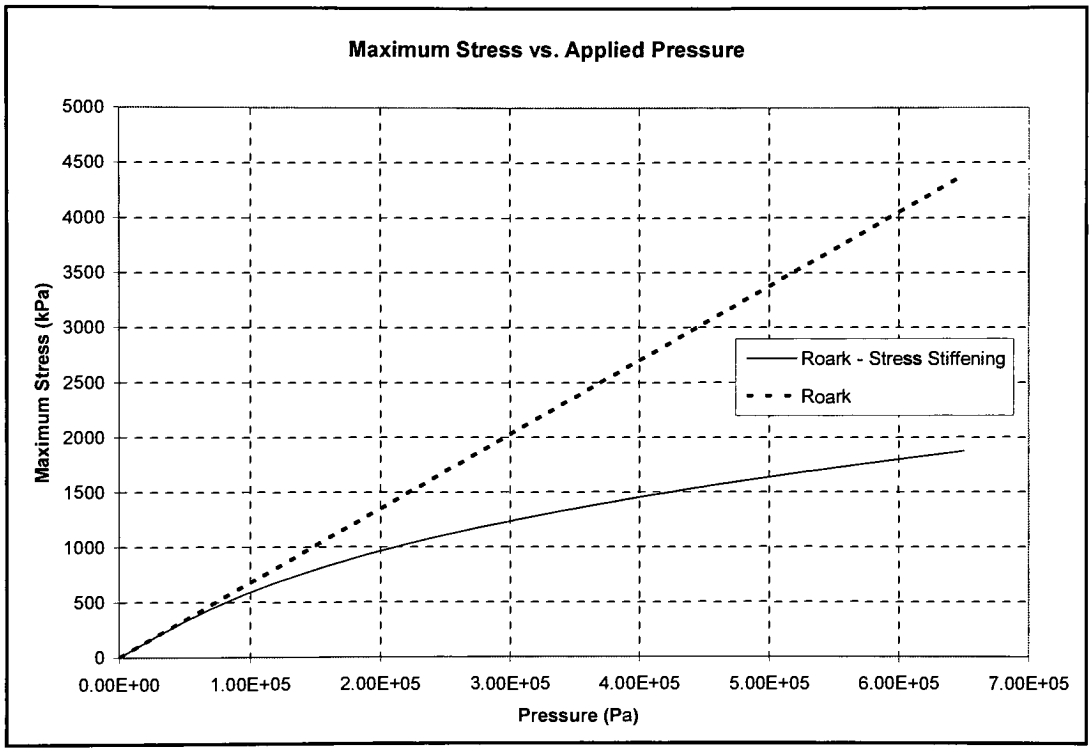

Figure 2.6 - Maximum Stress Results for 100 μm Thick Sylgard 184

Overall, the analytical model appears to be providing reasonable results, but this analytical model will be validated with finite element analysis (FEA) using the ANSYS software package.

2.3.2 Finite Element Analysis (FEA)

FEA was used to model the Bisco Solid Silicone Sheet to be used in the experimental setup. FEA on the membrane was completed for two reasons. First, the results of the FEA

model could be used to instill more confidence in the analytical model. Second, these results could then be used in a flow model to allow for a theoretical prediction of the flow behavior.

2.3.2.1 Model Setup

To determine the appropriate node density, a membrane of radius 0.3mm (0.012 in), and thickness of 0.127mm (0.005 in) was modeled with various node densities. The results were then plotted against each other to determine the number of nodes necessary to achieve a convergent solution. The model parameters used in the ANSYS model are shown below in Table 2.3.

Element Type	Axisymmetric Shell 51
Stress Stiffening	ON
Non-Linear Geometry	ON
Adaptive Solution Control	ON
Number of Substeps	20
Initial In-plane Tension	None
Number of Nodes	Variable
Node Spacing Ratio	0.25

Table 2.3 – ANSYS Solid Model Parameters

The model parameters used in this membrane analysis were obtained from literature on finite element analysis of flat plates (Boedo, 1999). The same material assumptions were made in the FEA model as made for the analytical model. The silicone was treated as a linear elastic isotropic material, and the physical properties used in the model were those of the Bisco Solid Silicone Sheet. The axisymmetric shell 51 element type allowed the circular plate to be modeled as a single line constructed of nodes and elements. This is shown in Figure 2.7. The boundary conditions were set to model a circular plate with clamped edges. The displacement of the node located at the center of the plate, or node '1' as designated in Figure 2.7, was constrained in the X-direction and Z-rotation. The displacement of the edge node, or node '2' as designated in Figure 2.7, was constrained in all degrees of freedom. The pressure load was applied to each element in the negative Y-direction.

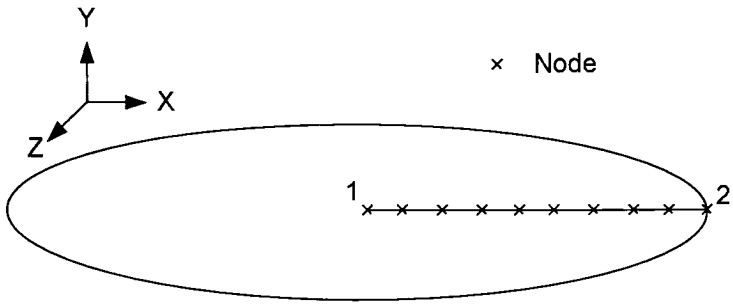

Figure 2.7 - ANSYS Model

The model was solved for an applied uniform pressure of 100 kPa (14.5 psi) with 50, 100, 150, 200, and 250 nodes. The results of each of these models were then compared to quantify the model's convergence. The maximum stress, Von Mises stress, and maximum deflection for each model are listed in Table 2.4.

Number of Nodes	Maximum Stress (kPa)	Von Mises Stress (kPa)	Maximum Deflection (mm)
50	418.74	362.85	.0338
100	421.54	365.26	.0338
150	431.72	374.08	.0330
200	432.34	374.61	.0330
250	432.71	374.93	.0330

Table 2.4 - Test Model Results

Looking at this data, it is clear that at least 150 nodes are necessary for the model to reach a convergent solution. The final model will use 150 nodes across the membrane radius to analyze the 0.254 mm (0.01 in) thick sheet silicone. The model setup is unchanged except for the thickness, which is adjusted to 0.254 mm (0.01 in).

2.3.2.2 Final Results

The results presented in this section are for a 0.6 mm (0.024 in) diameter Bisco Solid Silicone membrane with a thickness of 0.254 mm (0.01 in), clamped edges, and applied

pressures of 207 (30 psi) , 414 (60 psi), and 621 kPa (90 psi). These results will be presented and compared to the analytical model results presented in section 2.3.1.

Table 2.5 shown below summarizes the FEA results. It is clear that the membrane is far from failure under these loading conditions. The factor of safety for the membrane is at least six.

Pressure (kPa)	Stress Intensity (kPa)	Von Mises Stress (kPa)	Maximum Deflection (μm)
207	333	301	8.68
414	660	595	17.3
621	795	689	26.2

Table 2.5 - Summarized Results of FEA

Figure 2.8 is a plot of the Von Mises stress throughout the membrane for the 621 kPa (90 psi) loading case. The plot shows that the maximum stress is located at the clamped edge of the membrane, which is as expected.

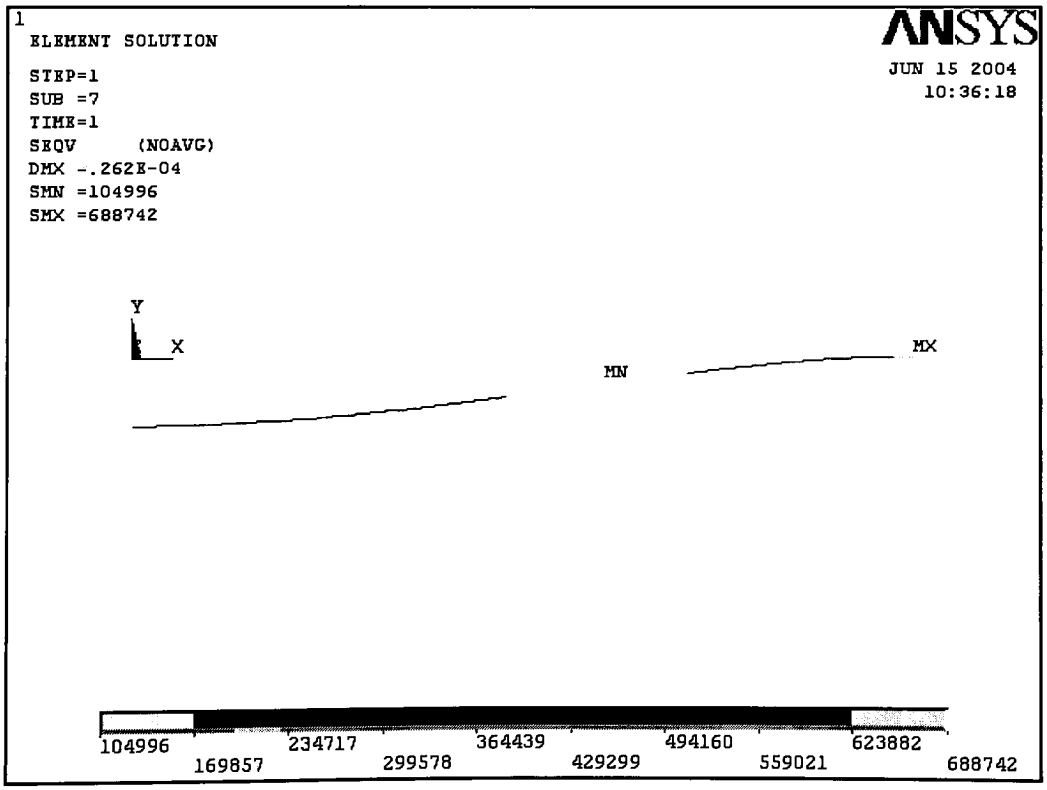

Figure 2.8 - Von Mises Stress Plot Under 621 kPa (90 psi) Pressure Load

The FEA results were also compared to the analytical model results. Figure 2.9 shows a plot of maximum deflection at the three loading pressures modeled within ANSYS. The greatest percent difference between the maximum deflection of the analytical model and FEA model for a given pressure is 2.5%. This close agreement instills more confidence in the model results. However, the stress values are not in as close of agreement. The greatest percent difference for the maximum stress in the membrane at a given pressure is 35%. Although the stress values are different, the stress obtained from the analytical model considers only the bending stress, while the ANSYS model is specifying a maximum stress. For this reason it would be expected that the ANSYS model would predict larger stress results than the analytical model. Also, because the membrane is well within the safe range of operation, this discrepancy in stress results is not of significant concern.

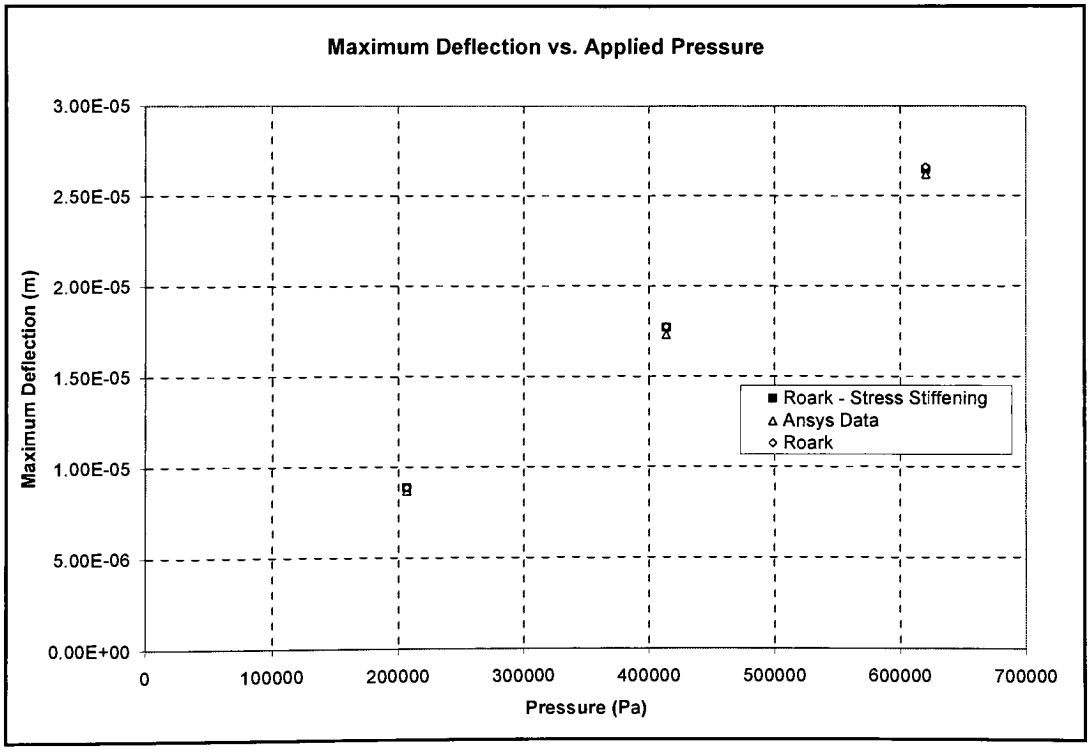

Figure 2.9 - Model Comparison – Maximum Membrane Deflection

The ANSYS results also provide a deflection profile. Using this profile information, the effective area of the deflection can be calculated. This can in turn be used to calculate the area reduction of the nozzle throat. Knowing this, a flow model can be constructed.

2.4 RIT Nozzle Design

The RIT nozzle design was completed using an isentropic one-dimensional analysis along with information gained throughout the literature review. The nozzle design was primarily driven by concerns regarding fabrication and experimental testing. Specific criteria was set, which provided the basis of the nozzle design. First, because the active flow control device is a silicone membrane, the nozzle shall be wider than it is thick to allow the membrane to deflect sufficiently into the nozzle flow. Secondly, the nozzle shall be capable of producing at least 10 mN (0.0022 lbf) of thrust so that it may be measured with reasonable accuracy using available equipment. Third, it shall be able to be fabricated using semiconductor fabrication techniques.

Using these criteria, and information gained throughout the literature search, the final nozzle design was determined. The nozzle consists of a two dimensional profile cut into a silicon wafer. The nozzle inlet is directed perpendicular to the nozzle flow, which allows for easy integration of the micro device to the macro world. When the flow enters the nozzle it turns into a plenum before converging to a 0.3 mm (0.012 in) x 0.6 mm (0.024 in) throat. The flow then enters the nozzle exit section comprised of a 20 degree divergence angle providing for an exit-to-throat expansion ratio of 25. The nozzle height remains unchanged at 0.3mm (0.012 in) throughout the expansion. The three-dimensional nozzle is being used for its easy fabrication. The throat size was determined by thrust calculations, which will be presented in the following sections. The expansion ratio of 25 along with the 20 degree divergence angle was used because of the high performance of a similar nozzle of this geometry studied by Chouhuri et. al. A CAD model of this nozzle is shown in Figure 2.10.

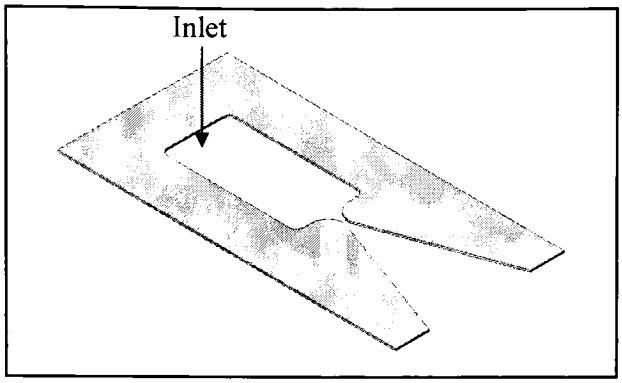

Figure 2.10 – Solidworks Model of RIT Nozzle

2.5 Isentropic One-Dimensional Analysis

An isentropic one-dimensional analysis is being used to achieve a better understanding of the flow behavior and overall performance of the nozzle under various operating conditions. This analysis should provide reasonable estimates for the nozzle's output thrust and specific impulse, as well as provide insight into the flow phenomena occurring inside the nozzle as inlet conditions vary.

The analysis will be completed for two very different operation states under similar pressure inputs. One analysis will consider the nozzle's performance under ideal conditions, where the exit pressure is low enough to provide the proper pressure ratio to ensure an isentropic expansion to supersonic flow. This is also considered running the nozzle 'on design.' The other analysis will consider an exit pressure of standard atmosphere, which will produce an adverse pressure gradient causing separation in the flow. This is considered running the nozzle 'off design.' The latter analysis mimics the conditions under which the nozzle will be experimentally tested.

The assumptions used to simplify both models are similar. Both models are assuming one-dimensional isentropic flow. Also, both models assume constant physical properties. Furthermore, the isentropic analysis assumes that the air is a calorically perfect gas; that is, its specific heats are considered constant.

2.5.1 On Design Operation

The model presented in this section provides insight into the performance of a nozzle with active flow control (AFC) if operated in a near vacuum environment. The analysis for 'on design' operation assumes that the nozzle is exhausting to near vacuum, where the exit pressure is set at 500 Pa (0.073 psi). The model assumes the total plenum pressure is set at 700 kPa (102 psi) with a constant geometry except for a variable nozzle throat area. Due to the set inlet pressure the nozzle is under expanded, which causes expansion fans to occur at the nozzle exit in order to equalize the flow pressure. The effect of these expansion fans on the nozzle performance are not being considered in this model. The equations and calculation procedure are contained within Appendix A. Only the results will be presented here.

Figure 2.11 is a plot of the nozzle thrust and specific impulse as the nozzle throat area decreases. This model predicts that as the throat area decreases the thrust will decrease, while the specific impulse will increase. If the Sylgard 184 membrane analyzed in Section 2.3.1 is used, at maximum deflection the thrust would decrease by approximately 32%, while the specific impulse would increase by approximately 1.5%.

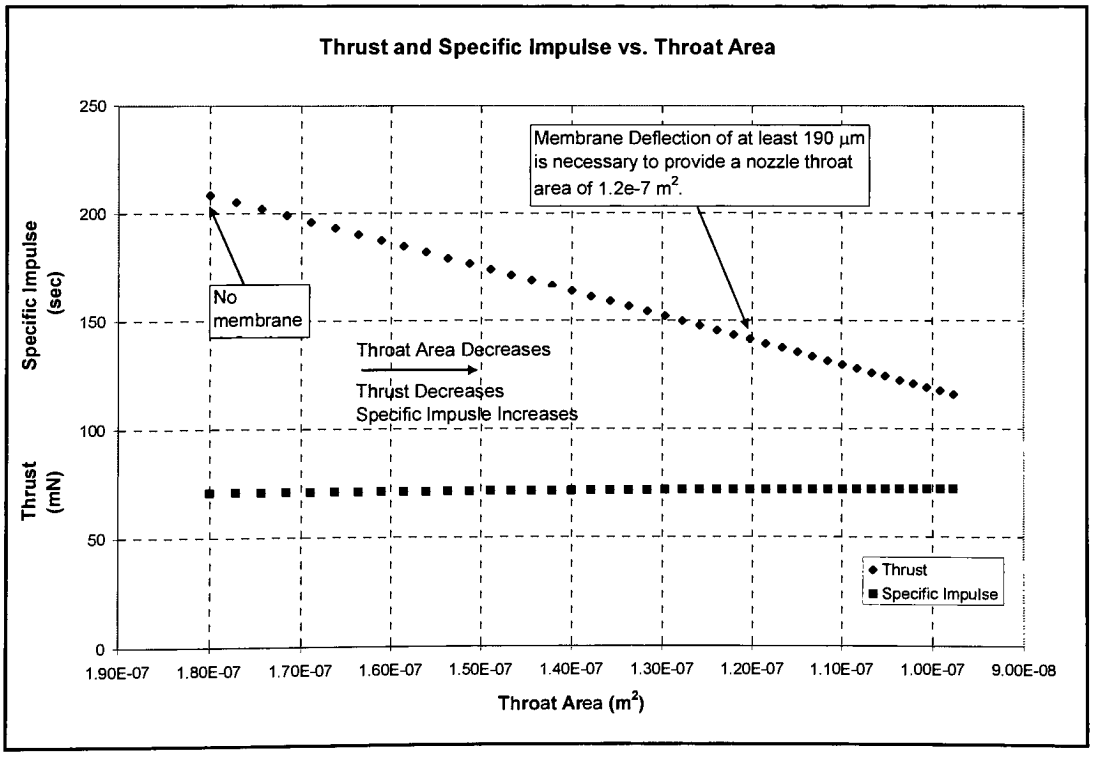

Figure 2.11 - Thrust and Specific Impulse vs. Throat Area For 1-D Isentropic Model

These results are for a specific geometry with an expansion ratio of twenty-five. The change in the overall thrust and specific impulse of a nozzle, due to a reduction in the throat area, is also a function of the initial nozzle expansion ratio. Figure 2.12 shows how the AFC effectiveness is affected by changing the initial nozzle expansion ratio. For the model results shown below, the inlet pressure was held constant at 700 kPa (102 psi). The original throat dimensions were maintained at 0.3mm (0.012 in) x 0.6mm (0.024 in), and the throat area was decreased from 1.8 e-7 m^2 (2.8 e-4 in^2) to 1.2e-7 m^2 (1.9 e-4 in^2) in each case. At each initial expansion ratio the percent difference in the thrust and specific impulse was recorded over the full range of the nozzle throat area.

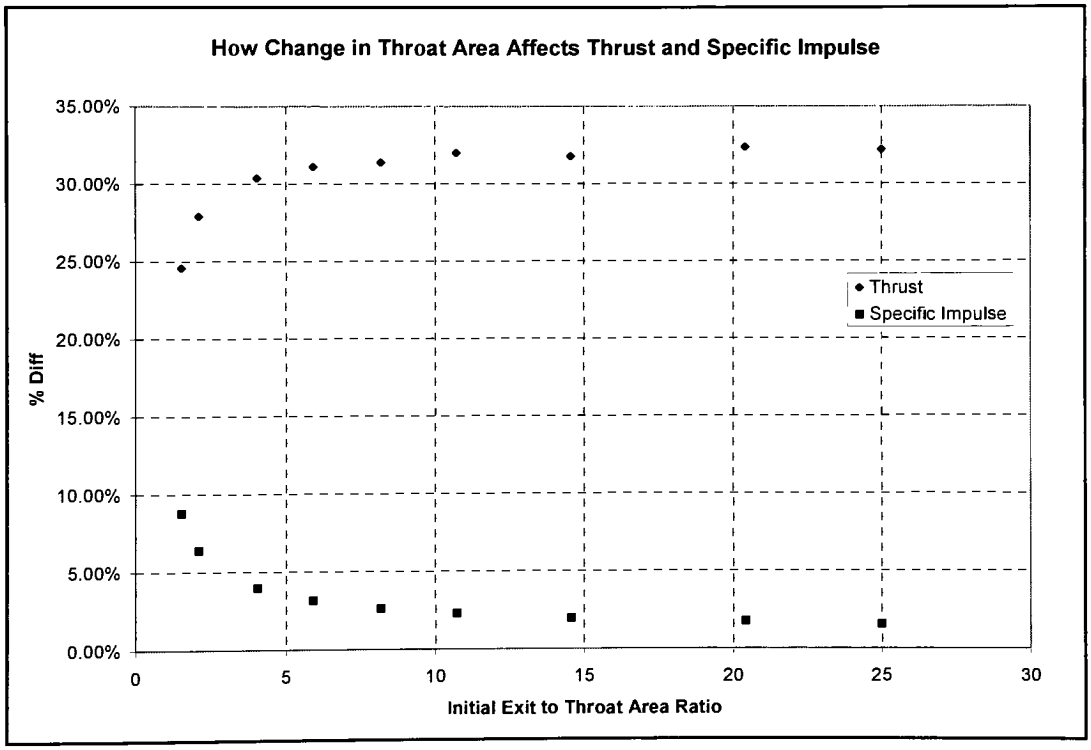

Figure 2.12 - AFC Effectiveness as a Function of Initial Exit to Throat Area Ratio For 1-D Isentropic Model

It is clear from this figure that as the initial expansion ratio is decreased the AFC's effectiveness in thrust output reduction is decreased, while the increase in the specific impulse is amplified. Of course, the change as a result of the throat reduction can be

increased further with the application of a thinner silicone diaphragm, which would allow for larger deflections, and consequently greater fluctuations in thrust and specific impulse.

2.5.2 Off Design Operation

'Off design' operation refers to nozzle operating conditions that will cause a shock or separation to occur within the nozzle's divergent section. This occurs when the inlet to exit pressure ratio across the nozzle is not large enough to provide the proper fluid expansion for a nozzle's geometric expansion. In the case of the RIT nozzle, the geometric expansion of the divergent portion of the nozzle is twenty-five. The inlet to exit pressure ratio necessary for this nozzle to operate 'on design,' or isentropically, is approximately 529.1. The RIT nozzle is being experimentally tested in atmospheric conditions, which means the exit pressure is approximately 1 atm. Therefore, for isentropic operation the inlet pressure must be 529.1 atm or 53611 kPa (7776 psi). Due to the inability to safely test at these pressures, the nozzle will be operating 'off design'. The isentropic model presented here is a first estimate of the nozzle performance under these operating conditions.

An additional assumption is necessary for this model. The shock formed inside the nozzle is not isentropic, but the shock is assumed thin, therefore the flow before and after the shock will be treated as isentropic. The equations and analysis procedure are contained in Appendix A. The results will be presented here.

Two models were constructed to predict nozzle performance under both changing inlet pressure and throat area. One model considers the RIT nozzle with its original geometry under varied pressure inlet conditions. Another model considers a single inlet pressure, while the nozzle throat area is varied. In both models the shock location, mass flow rate, thrust, and specific impulse are calculated. Figure 2.13 shows a plot of the shock location as the inlet pressure is varied from 207 kPa (30 psi) to 965 kPa (140psi). It is clear that as the pressure is increased the shock moves upstream.

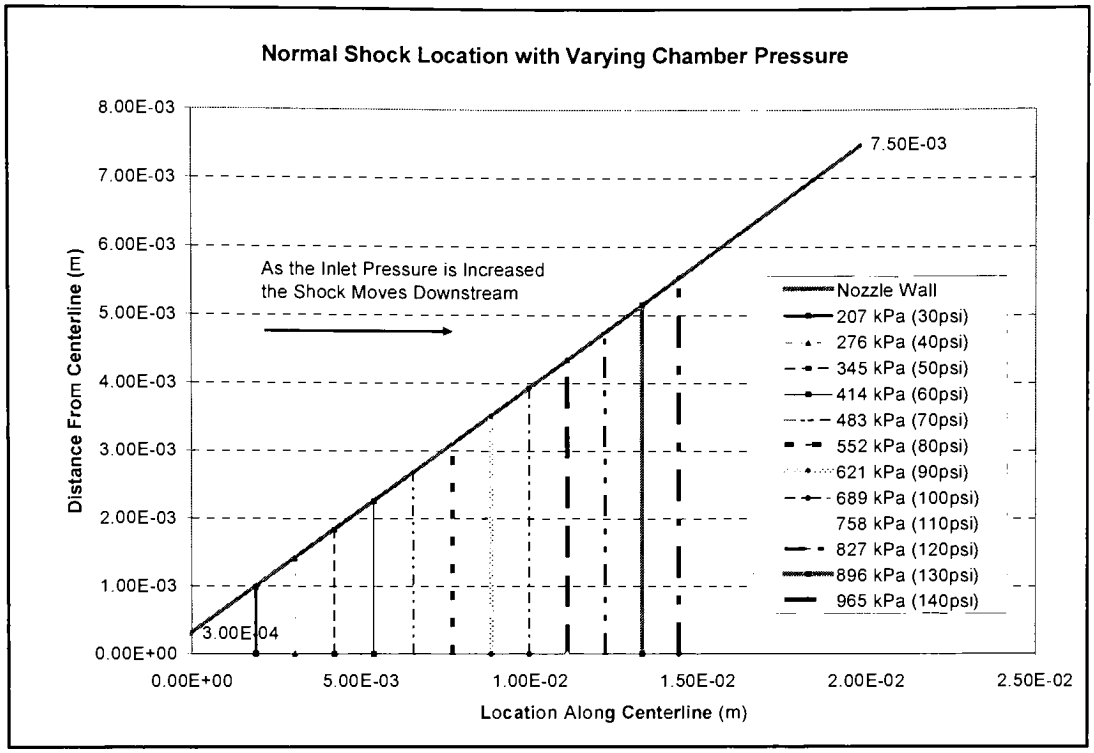

Figure 2.13 - Shock Location as Chamber Pressure Varies For 1-D Isentropic Model

As stated previously, the primary application of the device investigated in the current study is thrust production for small satellites. Therefore thrust and specific impulse performance are vital. Figure 2.14 is a plot of the thrust and specific impulse performance as the inlet pressure is varied from 207 kPa (30 psi) to 965 kPa (140psi). It is interesting to note that the thrust seems to be increasing exponentially while the specific impulse appears to be increasing linearly with pressure. This is expected because the specific impulse is a function of velocity, whereas the thrust is a function of the square of the velocity. The specific impulse values are somewhat low due to the low exit speed of the separated flow, and the maximum thrust output is approximately 30 mN (0.0067 lbf).

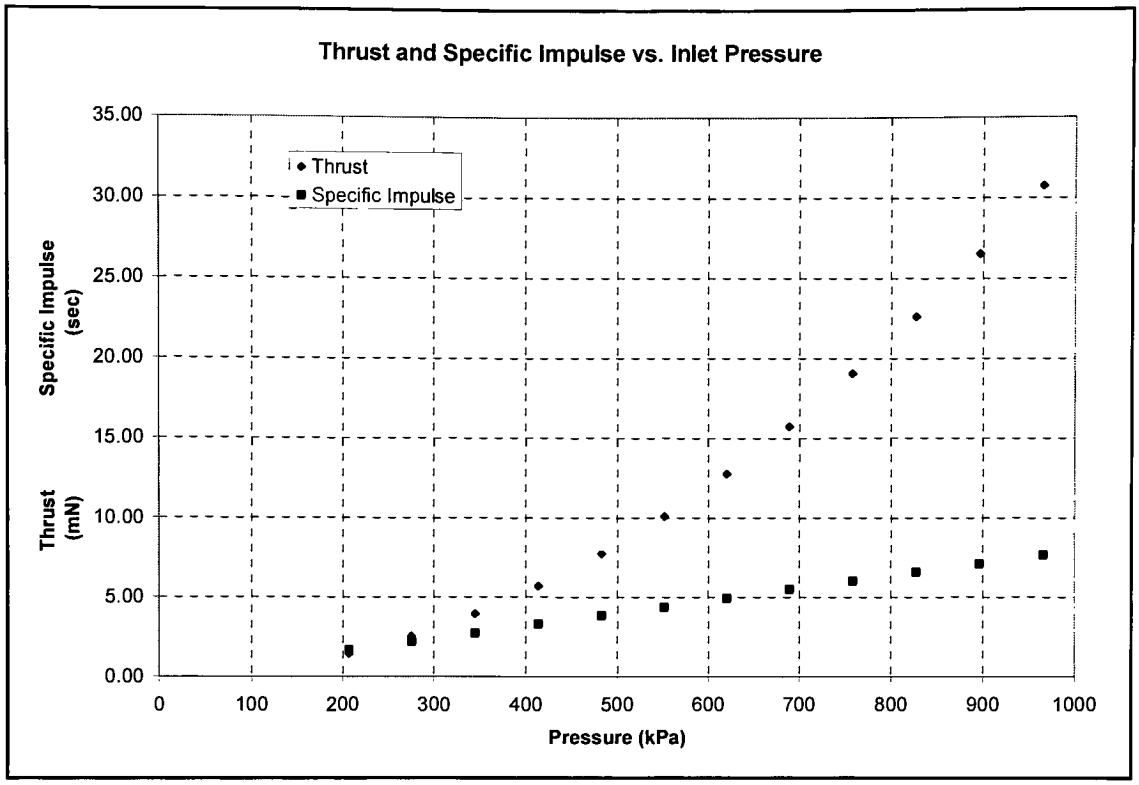

Figure 2.14 - Thrust and Specific Impulse vs. Inlet Pressure For 1-D Isentropic Model

The other model constructed under separation conditions considers a single inlet pressure while the throat area is varied similarly to that in the 'on design' isentropic model. The inlet pressure is set at 552 kPa (80 psi) while the throat area is varied from its initial value of 1.8 e-7 m^2 (2.8 e-4 in^2) to a final value of 1.0 e-7 m^2 (1.6 e-4 in^2). As the throat area is decreased the shock location, thrust, and specific impulse are calculated. Figure 2.15 is a plot of the shock location as the throat area is decreased. It is evident that as the throat area is decreased the shock moves upstream. This is expected because the decrease in the throat area provides an increase in the nozzle expansion ratio. Therefore, when the throat area is decreased the fluid reaches the same level of compression at a location further upstream.

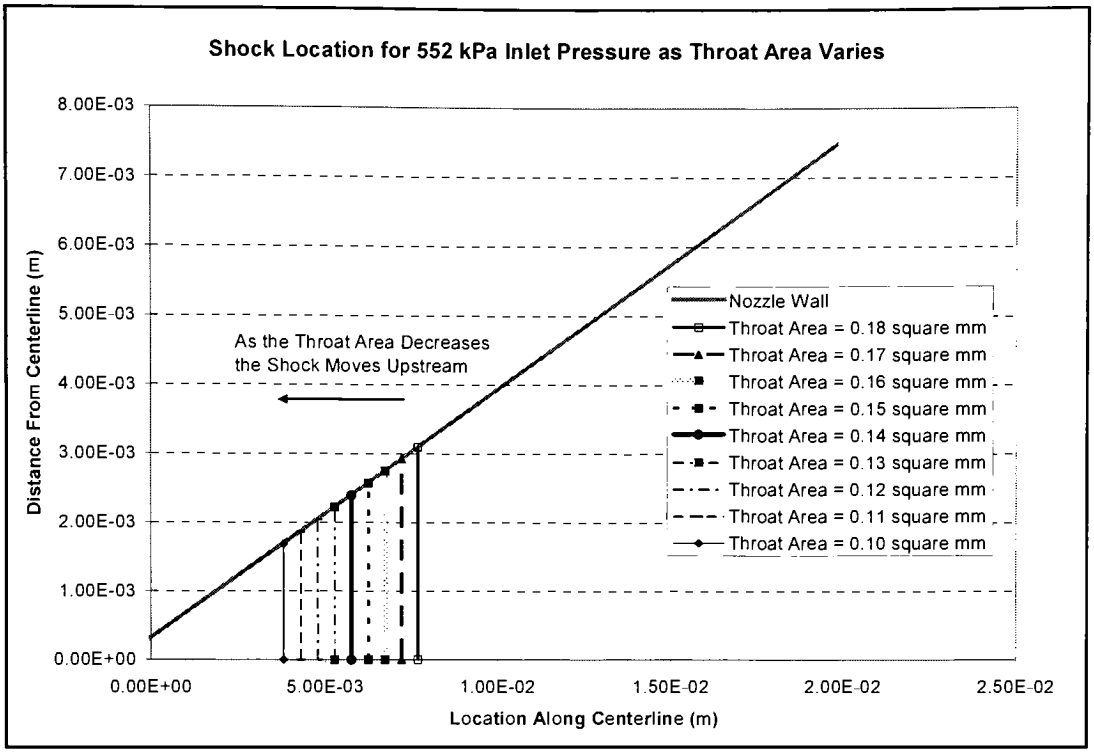

Figure 2.15 - Shock Location as Throat Area is Varied For 1-D Isentropic Model

The thrust and specific impulse are also significantly affected by the throat area reduction, which can be viewed in Figure 2.16. As the throat area is reduced the thrust and specific impulse decrease. This is different than the nozzle running 'on design' because the exit speed decreases as nozzle throat area decreases when separation is present. Once again, the thrust is more significantly affected by the change. Over the throat area reduction, the thrust output of the nozzle is decreased by approximately 69 percent, while the reduction in the specific impulse is approximately 44 percent.

The isentropic model will be compared to a computational fluid dynamics (CFD) model as well as experimental data. This analysis provides for a basic understanding of the characteristics of the flow within the nozzle, as well as providing an initial estimate regarding nozzle performance.

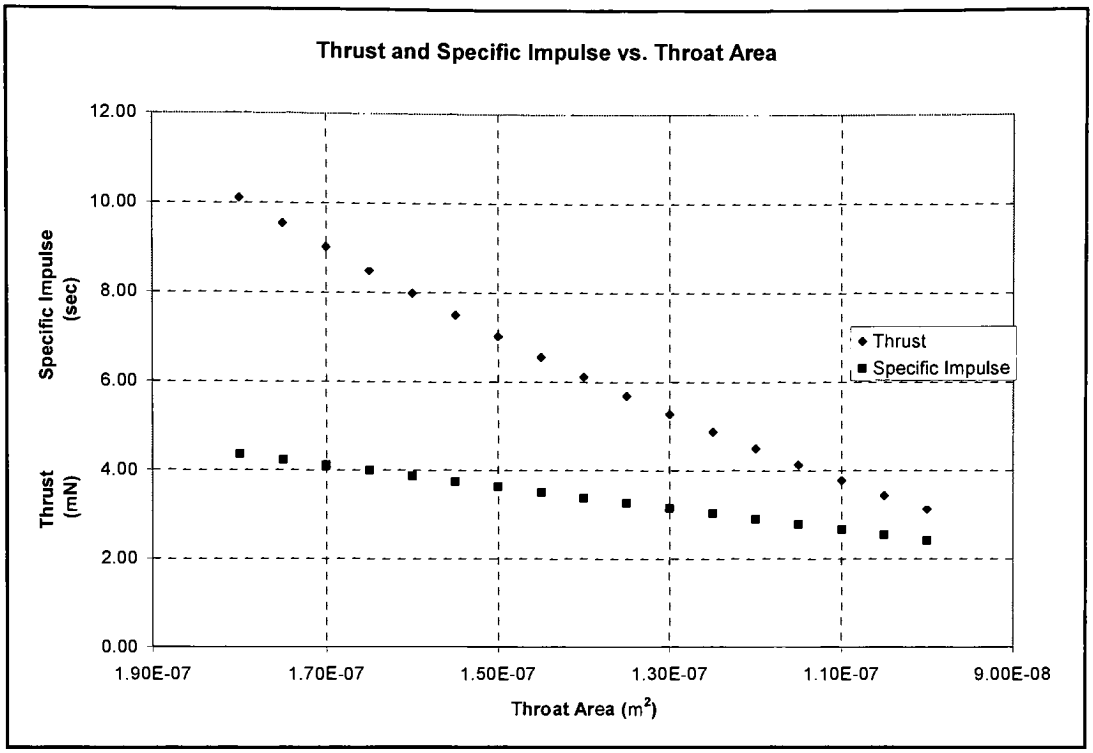

Figure 2.16 - Thrust and Specific Impulse as Throat Area is Varied For 1-D Isentropic Model

The isentropic model was used in conjunction with other factors to determine the nozzle throat dimensions. Using this data, the nozzle size was chosen to allow compatibility with available experimental equipment. The throat size is such that the thrust output is large enough to allow for accurate measurement with the available balance, while the flow rate is small enough to utilize an available flow meter. The throat size was determined by meeting these demands, but using the smallest workable dimension. The experimental equipment will be discussed in more detail in Section 5.1.

3 CFD Analysis

The viscous flow through the supersonic nozzle will be modeled using the FLUENT computational fluid dynamics (CFD) software package. Flow through the designed nozzle with and without flow control will be modeled to determine the effects of the flow control device on the output thrust and flow behavior.

Before modeling the RIT nozzle, a similar micro-nozzle must be modeled to verify the validity of a viscous model solution for a problem of this type. Experimental results for a similar nozzle are being used to validate a CFD model using thrust data along with qualitative experimental results obtained through Schlieren photography. Once model settings are determined and validated, a similar viscous model will be constructed to analyze the flow through the RIT nozzle, with and without flow control.

3.1 Basic Model Setup

3.1.1 Fluid Type

Both of the modeled nozzles are of similar size and geometry. More specific details will be described in the geometry section of this chapter. In both nozzles the propellant fluid is air. The properties used are obtained from the default material settings provided within the FLUENT database. Table 3.1 below shows the property settings used for the working fluid in each model.

Air Property Settings in Fluent Model	
Density	Ideal Gas
Cp	1006.43 $^{J}/_{kg\text{-}K}$
Thermal Conductivity	0.0242 $^{W}/_{m\text{-}K}$
Viscosity	1.79E-05 $^{kg}/_{m\text{-}s}$
Molecular Weight	28.966 $^{kg}/_{kgmol}$

Table 3.1 - Air Property Settings

3.1.2 Flow Physics

The flow modeled in each nozzle is moving at both subsonic and supersonic speeds. Due to the high speeds of the flow it is important that the fluid is treated as compressible. The flow of interest is driven by a pressure change across the device. These pressure conditions along with the nozzle geometry are two factors that determine the operating flow regime. Due to the pressure conditions and geometries being modeled in the current study, it is expected that the flow will reach supersonic speeds and then transition to subsonic speeds through either a shock or a shock-free viscous transition. The shock is likely to occur because the nozzles are being operated 'off-design.' The shock-free viscous transition may occur due to the low aspect ratio of the nozzles being studied. The nozzle aspect ratio refers to the throat height to width ratio. This shock-free viscous transition is due to the boundary layer build up, which fills the nozzle exit, slowing the flow.

3.1.3 Boundary Conditions

Four boundary conditions are necessary to satisfy the problem addressed in this study. Figure 3.1 shown below depicts the RIT nozzle with three boundary conditions labeled one thru three.

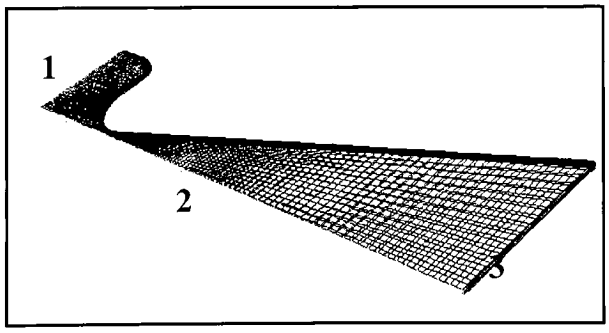

Figure 3.1 – Boundary Conditions

The face labeled '1' in Figure 3.1 is a pressure inlet. This is the total pressure or the plenum pressure. The face labeled '2' in Figure 3.1 is a symmetry boundary condition; because the geometry is symmetric, the boundary condition can be used to lower mesh size and consequently computational time. The face labeled '3' in Figure 3.1 is a pressure outlet boundary condition. This boundary pressure was set at atmospheric pressure to represent the

nozzle's exhaust to standard atmosphere. The fourth boundary condition is the wall boundary defined by the nozzle geometry. The wall is designated as a stationary wall with zero heat flux. The walls defining the nozzle geometry are significantly large, which would inhibit significant heat transfer to and from the system, and therefore, the assumption of no heat flux is considered reasonable.

3.1.4 Meshing Strategy

The ability to achieve a convergent solution in FLUENT is very much dependant upon the mesh that is constructed within Gambit. Gambit is a software package used in the construction of a model's geometry and mesh. For a high quality mesh, in general it is ideal to mesh using quad elements with little skew and a low aspect ratio. This was considered while meshing each of the nozzle geometries. The mesh size was limited by the computing power of the systems available. This limited the mesh size to approximately 150,000 elements.

Due to the turbulent boundary layer inherent in high speed flows it is important to capture boundary layer effects. These wall effects are of significant importance, and if not detected, the validity of the entire solution can suffer (FLUENT Help Manual). For this reason care was taken to place several elements within the boundary layer along each of the wall boundaries.

3.1.5 FLUENT Limitations

Limitations include the assumptions being made in the analysis to decrease iteration time and model complexity, as well as more fundamental limitations as a result of the limitations of the theoretical models being employed by the software. The small scale flow in the current investigation warrants an investigation into the validity of the theoretical model used by FLUENT.

The flow regime through the micro-nozzle can be determined by the Reynolds number and Knudsen number. Equation 3-1 is the formulation used to calculate the Reynolds number in a two-dimensional nozzle (Bayt, 2001).

$$\mathrm{Re}_l = \frac{\rho_l M_l d_l}{\mu_l}$$

Equation 3-1 - Reynolds Number

The Reynolds number for the smaller RIT nozzle is at the very least 8260 at the nozzle throat. This value can be used to then calculate the Knudsen number, which will provide insight into the validity of the no slip, continuum analysis used by FLUENT. The Knudsen number has also been described as the degree of rarefaction of a gas (Zelesnik, 1991). Equation 3-2 shows the formulation used to calculate the Knudsen number.

$$Kn = \frac{\lambda}{\ell} \approx \frac{M}{\mathrm{Re}_l}$$

Equation 3-2 - Knudsen Number

Equation 3-2 assumes a perfect gas at thermodynamic equilibrium. The given geometry generates a maximum Knudsen number on the order of 1 x 10^{-4}. Table 3.2 shown below depicts the Knudsen number ranges and their corresponding significance to the applied theoretical flow model.

Kn < 0.01	Continuum Flow
0.01<Kn< 0.1	Slip at Walls
0.1<Kn<10	Transition Flow
Kn>10	Free Molecular Flow

Table 3.2 - Knudsen Number Definition

It is evident from the information in this table that the continuum model utilized by FLUENT is indeed an applicable theoretical model for the device analyzed in the current study.

The limitations inherent in the flow assumptions made by the designation of material properties and solver selections will be described in detail in the FLUENT setup section of this report.

3.2 Geometry and Model

3.2.1 Validation Model

The validation model consisted of a nozzle designed, fabricated and tested by the University of Oklahoma (Choudhuri et. al., 2001). Figure 3.2 is a picture of the nozzle, which was fabricated from electro-discharge machined (EDM) copper.

Figure 3.2 - University of Oklahoma Micro-Nozzle

The model of this nozzle was imported into Gambit and simplified before meshing was completed. The inlet was shortened to lower the mesh size, and the radius at the inlet was eliminated to allow for a simplified mesh of little skew. Also, the convergence angle at the inlet was reduced to reduce mesh skew. This geometric change is validated by experimental research that has concluded that the inlet geometry has little effect on the output flow (Back, Cuffel, and Massier, 1973). Figure 3.3 shows the final model with vertex coordinate values expressed in millimeters. The overall length and height of the nozzle is approximately 17mm (0.67 in) and 4.7mm (0.19 in) respectively, with a throat width of 0.38mm (0.015 in). Only half of the nozzle is modeled due to an applied symmetry boundary.

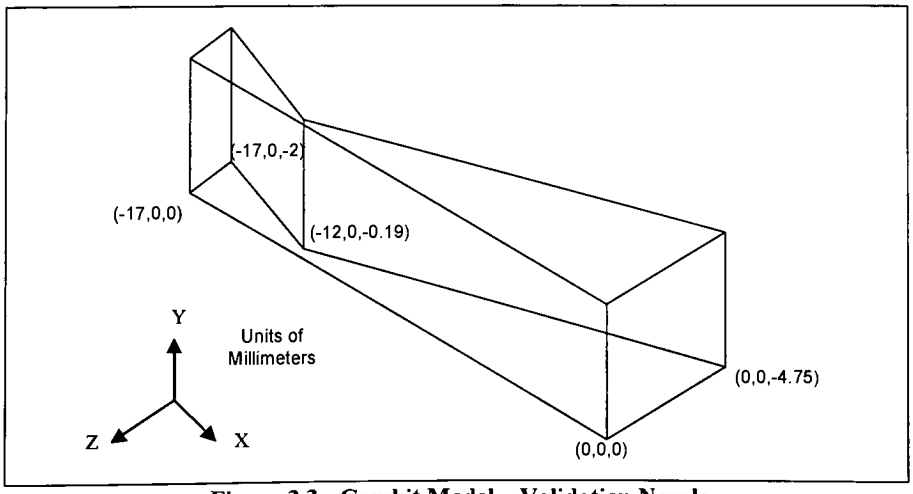

Figure 3.3 - Gambit Model – Validation Nozzle

3.2.2 RIT Nozzle

The RIT nozzle's geometry is of similar scale and shape to the University of Oklahoma's nozzle, but several critical dimensions are different. The model imported into Gambit for this nozzle was also slightly modified to allow for the construction of a high quality mesh. The only modification made to this model was the shortening of the inlet. A drawing of the Gambit model is shown in Figure 3.4 with the vertex coordinate values expressed in millimeters.

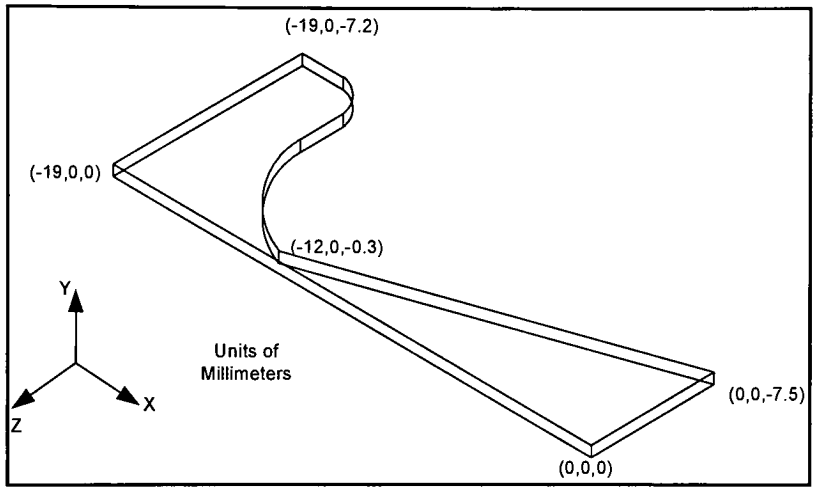

Figure 3.4 – Gambit Model - RIT Nozzle

The overall length and height of the nozzle is approximately 19mm (0.75 in) and 0.3mm (0.012 in) respectively, with a throat width of 0.6mm (0.024 in). Only half of the nozzle is modeled due to an applied symmetry boundary.

3.3 Mesh Details

3.3.1 Validation Model

The entire nozzle mesh is constructed of quad elements, using a mapped mesh scheme. The first step in the process of meshing the geometry described by Figure 3.3 is the application of a boundary layer mesh along each wall. The boundary layer settings are shown in Table 3.3.

First Row Height	0.0005 mm
Growth Factor	1.2
Number of Rows	10
Depth of Boundary Layer Mesh	0.01298 mm

Table 3.3 - Boundary Layer Mesh Settings

Once the boundary layer mesh was complete, each edge was meshed independently. The upper faces were then meshed, followed by a volume mesh over the nozzle depth. Figure 3.5 shows the mesh used in the final validation model.

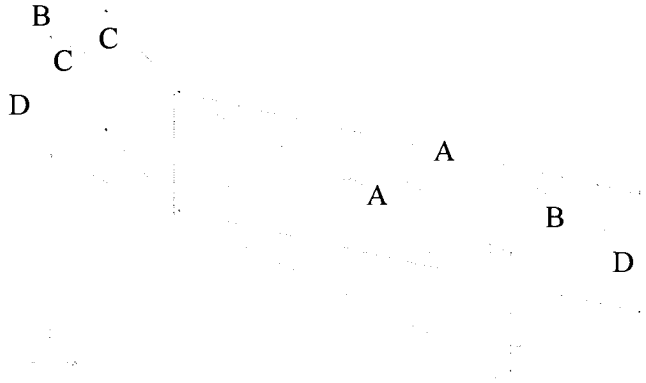

Figure 3.5- Validation Model Mesh

The edges designated 'A' in Figure 3.5 have 50 nodes, those designated 'B' have 40 nodes, those designated 'C' have 20 nodes, and those designated 'D' have 50 nodes. Each set of edge nodes has a successive ratio of 1. The resulting volume mesh consists of 140,000 elements of an equi-angle skew (EAS) below 0.3.

3.3.2 RIT Nozzle

The RIT nozzle's geometry is more complex than the validation model's, therefore a small number of wedge elements were necessary. Each of the faces along the upper nozzle boundary were meshed before a Cooper volume mesh was applied over the nozzle depth. Figure 3.6 shows the mesh used in the RIT nozzle for cases both with and without flow control.

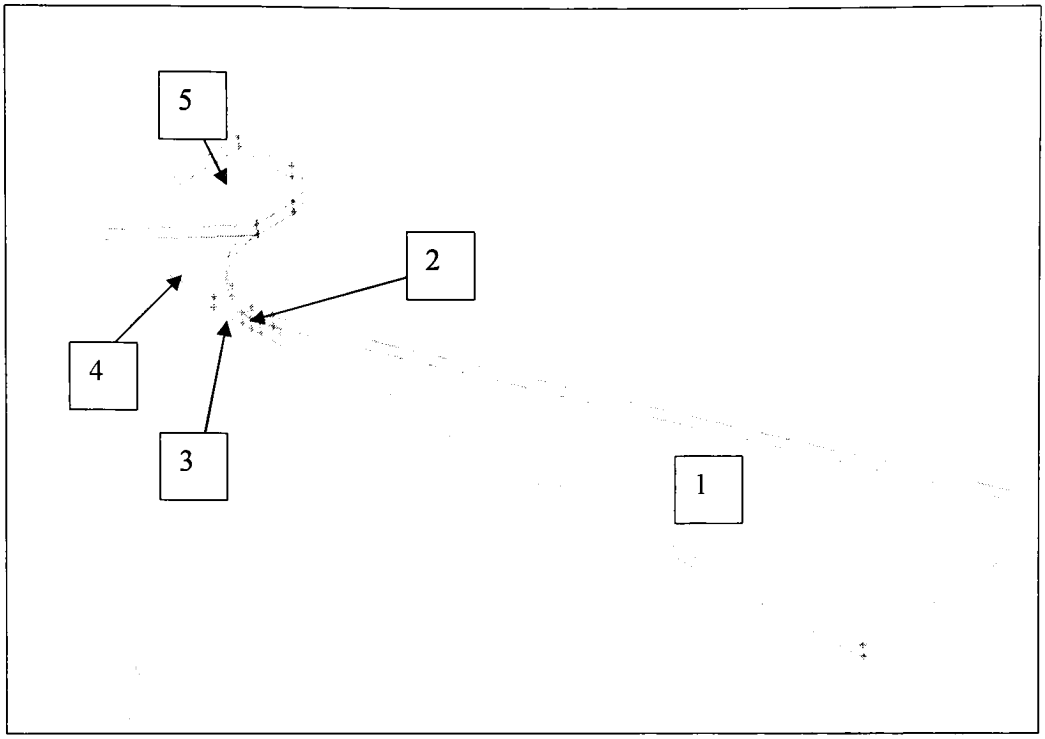

Figure 3.6 - RIT Nozzle Mesh

Before any faces were meshed, the same boundary layer mesh used in the validation model was applied to the RIT nozzle's model. The RIT nozzle was then divided into 5 separate volumes to permit the construction of a high quality mesh. Figure 3.6 shows each of these volumes labeled one thru five. Volume '1' is a simple quad map mesh that consists of 50 nodes along the length of the nozzle with a successive ratio (SR) of 0.95 to tighten the mesh towards the nozzle throat. A total of 25 nodes are applied across the width of the nozzle with an SR of 1. Volume '2' is the volume containing the nozzle throat and the deflected silicone diaphragm. The diaphragm profile was obtained from the ANSYS solid modeling results presented in Section 2.3.2.2 and imported into Gambit as vertex values. A total of 150 vertex values were used over the 0.3mm (0.012 in) radius diaphragm. These vertex values were then used to create the final membrane volume. Due to the complexity of this geometry, the only acceptable mesh was found to be a tri-pave face mesh. A close-up of this mesh is shown in Figure 3.7. Before applying the tri pave mesh 15 nodes were applied to each of the edges labeled 'A' in Figure 3.7. The edges across the width of the nozzle maintain 25 nodes.

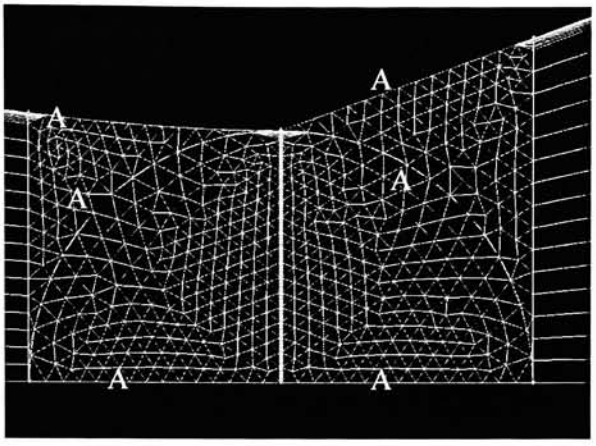

Figure 3.7 - Face Mesh of Throat Section

Volume '3' as designated in Figure 3.6 is the first section of the nozzle upstream of the nozzle throat. Due to the small curvature in this section of the inlet, it was possible to use a Quad/Map mesh. The resulting mesh is shown in Figure 3.8. The edges marked 'A' in the figure below each contain 20 nodes with an SR of 1. The edges across the width of the nozzle maintain 25 nodes.

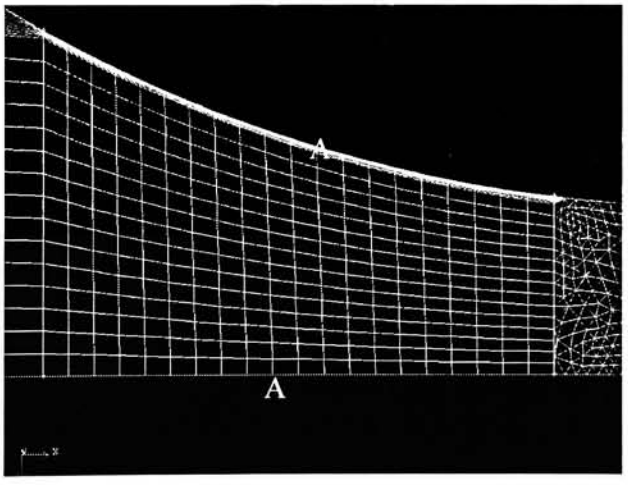

Figure 3.8 - Face Mesh of First Section Upstream of Inlet

Volume '4' as designated in Figure 3.6 is further upstream of the section shown above in Figure 3.8. This section was also meshed using quad map elements, but due to the significant curvature at this portion of the inlet, significant element skew ($0 < EAS < 0.5$) is

present. The edges labeled 'A' in this section have 20 nodes, while the number of nodes across the nozzle is maintained. A close-up of this mesh is shown in Figure 3.9. The boundary layer mesh was abandoned in volumes '4' and '5' as designated in Figure 3.6.

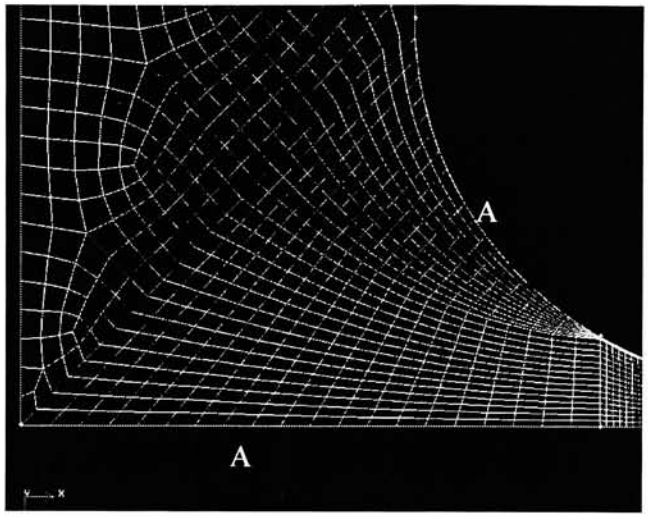

Figure 3.9 - Inlet Mesh

The final volume labeled '5' as designated in Figure 3.6 is shown below in Figure 3.10. Due to the complexity of the geometry in this section, the face mesh was achieved by applying a quad pave mesh with an interval size of 0.2.

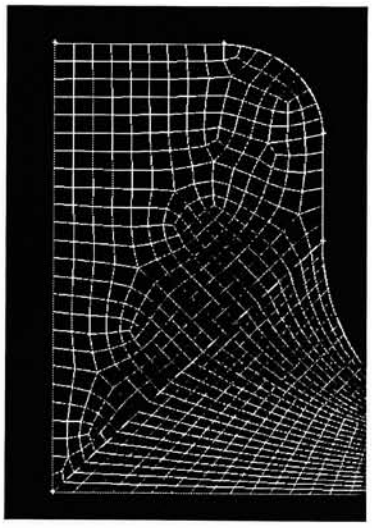

Figure 3.10 - Inlet Mesh

The final volume mesh was constructed by employing the Cooper scheme to the constructed face mesh. A total of 30 nodes were used across the nozzle thickness producing a mesh consisting of 109,230 elements. Of these 109,230 elements, 100,950 (92%) elements have an EAS less than 0.3.

3.4 FLUENT Setup

Both the validation and RIT nozzle models employ the same boundary conditions; a pressure inlet, a pressure outlet, a symmetry boundary, and a wall boundary. The operating pressure in both models was set to zero (recommended for supersonic flow), and 2nd order upwind turbulent models were used. The inlet pressure was modified as necessary and the outlet pressure was set to atmosphere. All other model specific setup parameters are discussed fully in their respective sections.

3.4.1 Validation Model

The final model setup in FLUENT was achieved after several iterations in which various model parameters were adjusted. Each of these cases and their respective parameter inputs are recorded below in Table 3.4.

	Solver	Turbulent Model	Material Prop.	Precision	Symmetry	Boundary Layer Mesh	Converged	Inlet Pressure
4 cases	Coupled/ Implicit	Spalart-Allmaras	Density Ideal Gas Viscosity - Sutherland	Single	One, Two Planes, None	None	No	2.1 Bar
	Coupled/ Implicit	k-ε	Density Ideal Gas Viscosity - Sutherland	Single	One Plane	None	Yes	2.1 Bar
	Coupled/ Implicit	k-ε	Density - Ideal Gas	Single	One Plane	None	Yes	2.1 Bar
	Coupled/ Implicit	k-ε	Density - Ideal Gas	Single	One Plane	None	Yes	5.0 Bar
	Coupled/ Implicit	k-ε	Density - Ideal Gas	Single	One Plane	None	Yes	10.6 Bar
	Coupled/ Implicit	k-ε	Density - Ideal Gas	Double	One Plane	None	Yes	10.6 Bar
	Coupled/ Implicit	k-ε	Density - Ideal Gas	Single	One Plane	Yes	Yes	2.1 Bar
	Coupled/ Implicit	k-ε	Density - Ideal Gas	Single	One Plane	Yes	Yes	8.0 Bar
	Coupled/ Implicit	k-ε	Density - Ideal Gas	Single	One Plane	Yes	Yes	10.6 Bar

Table 3.4 - Case Study History - Validation Model

The initial FLUENT setup utilized the Spalart-Allmaras turbulent model with the default coefficients. Unfortunately, even after several adjustments were made to the mesh and the

material properties, the model would not converge. For all of the cases listed in Table 3.4, the mass flow rate through the nozzle exit face was monitored. In the four cases using the Spalart-Allmaras turbulent model, the mass-flow rate would also not converge to a steady value.

The first successful case occurred with the use of the default k-ε turbulent model. This turbulence model would be used for the remainder of the test cases. The Courant number and relaxation factors never required modification, and therefore the default values were used. Also, the coupled/implicit solver was used in each case due to the highly interdependent fluid properties inherent with high speed compressible flows.

Throughout the trial cases it became evident that the initialization phase was critical in determining whether a case would or would not converge. In order to ensure a good initial guess at the pressure inlet, the isentropic analysis was referenced. Due to the flow physics at work in the modeled device, it was fairly simple to back-out the inlet speed of the flow. Equation 3-3 shown below is used to solve for the inlet Mach number for a known fluid and inlet to throat area ratio.

$$\left(\frac{A}{A_t}\right)^2 = \frac{1}{M^2}\left[\frac{2}{(\gamma+1)}\left(1+\frac{\gamma-1}{2}M^2\right)\right]^{\frac{\gamma+1}{\gamma-1}}$$

Equation 3-3 – Isentropic - Area Ratio - Mach Number Relationship

Once the upstream Mach number is known the static pressure is calculated using Equation 3-4.

$$\frac{P_o}{P} = \left[1+\frac{\gamma-1}{2}M^2\right]^{\frac{\gamma}{\gamma-1}}$$

Equation 3-4 – Isentropic - Pressure Ratio - Mach Number Relationship

The model was then initialized using the static pressure and x-velocity calculated from the process described above.

Once a convergent solution was achieved other parameters were adjusted to determine their effect on the model solution. For example, the air viscosity was modeled using the three-coefficient Sutherland model. The resulting solution was in good agreement with the original model solution and consequently it was decided that the additional computational effort required by instituting the viscosity model was unnecessary. In another case, the model was solved using double precision computations. This also resulted in a nearly identical solution. Once again the additional computational effort was deemed unnecessary. Finally, the original course mesh was modified with the addition of wall treatments. A boundary layer mesh as described in Section 3.3 was applied. The wall treatment lowered the y-plus values into an acceptable range. The y-plus property is used to determine if the mesh density is sufficient within the boundary layer of the modeled flow. The final three cases shown in gray in Table 3.4 represent the final FLUENT setup used for the validation model. Table 3.5 summarizes the boundary conditions for the three different inlet pressures modeled.

Total Pressure Inlet Pa (psi)	Static Pressure Inlet Pa (psi)	Pressure Outlet Pa (psi)
210,000 (30.5)	208,231 (30.2)	101325 (14.7)
800,000 (116.0)	793,261 (115.1)	101325 (14.7)
1,060,000 (153.7)	1,051,071 (152.4)	101325 (14.7)

Table 3.5 - Boundary Condition Values - Validation Model

3.4.2 RIT Nozzle

The FLUENT setup for the RIT nozzle was very similar to that of the validation model. The final setup parameters are shown in Table 3.6. The only adjustment made from the validation model to the RIT nozzle was the use of the double precision solver for the RIT nozzle. The double precision solver was necessary because of the nozzle's long slender geometry. For geometry of its type, it is recommended by FLUENT that a double precision solver be used.

Solver	Coupled/Implicit
Energy	On
Turbulent Model	k-ε
Material Properties	Air – Density – Ideal Gas Viscosity – Constant
Turbulent Kinetic Energy	2nd Order Upwind
Turbulent Dissipation	2nd Order Upwind
Precision	Double

Table 3.6 - FLUENT Setup Parameters - RIT Nozzle

The boundary conditions in all cases modeled were as designated in Table 3.7.

Total Pressure Inlet Pa (psi)	Static Pressure Inlet Pa (psi)	Pressure Outlet Pa (psi)
551,581 (80.0 psi)	549,714 (79.7)	101,325 (14.7)

Table 3.7 - Boundary Condition Values - RIT Nozzle

For the RIT nozzle four separate cases were modeled. In each the wall boundary was modified to either represent a nozzle without flow control or represent a nozzle with active flow control of various membrane deflections.

3.5 Results

3.5.1 Solution Validity

Before the results are presented for the two models, it should be understood that solution convergence was achieved under specific criteria. First, the default residual convergence criterion was not entirely the basis for judging convergence. Three factors were considered before judging convergence. The first factor was the residual data. Another factor was the ability of the monitored mass-flow rate to reach a steady value. The final factor was the satisfaction of the conservation of mass and energy evaluated using flux reports. As long as the mass-flow rate had reached a steady value and the flux imbalance was less than 5% of the nominal flux, the solution was considered converged, regardless of the residual data.

Other factors used to determine solution validity beyond conservation of mass and energy was the trend in the solution entropy. In general, the entropy increases within the boundary layer, and as the flow proceeds downstream, as expected. A contour plot of the entropy in the RIT nozzle with flow control is shown in Figure 3.11. While the entropy is shown as negative, this is simply due to an incorrect reference value; the trend in the entropy is of more importance.

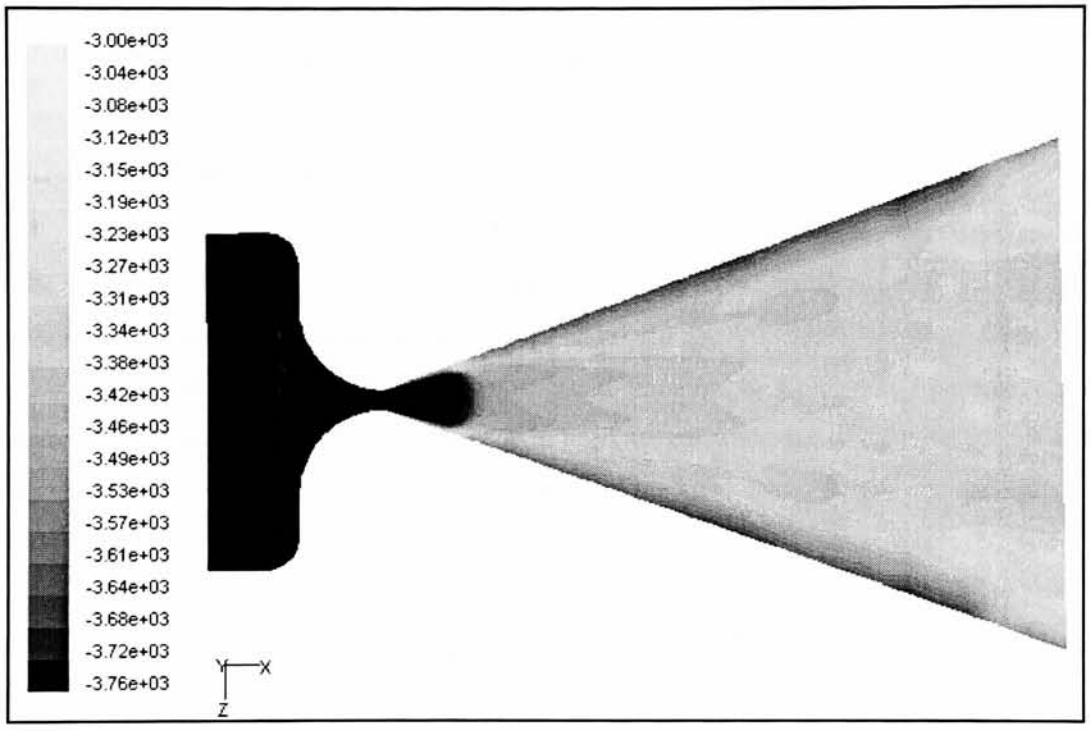

Figure 3.11 - Contours of Entropy for RIT Nozzle w/ Membrane Pressurized to 207 kPa (30 psi)

Grid independence was also checked in the RIT model. Two meshes were constructed of similar grid type, but of different densities. The grid used in the results section of this report has a total of 92,400 elements. The grid used to test grid independence is nearly half as dense with 54,025 elements. The two models were solved for an inlet pressure of 552 kPa (80 psi) and the critical parameters of interest in this study were compared for the two solutions. Table 3.8 shows the results and the percent difference between the two models' results.

Model	Inlet Flow rate (kg/s)	Outlet Flow rate (kg/s)	Energy In (W)	Energy Out (W)	Thrust (N)	Specific Impulse (s)
Large Mesh	2.18e-4	-2.28e-4	32.97	-33.01	0.0337	15.75
Small Mesh	2.18e-4	-2.17e-4	32.85	-31.95	0.0358	16.78
Percent Difference	0.37%	4.85%	0.37%	3.32%	5.80%	6.16%

Table 3.8 - Grid Independence Comparison

The small variation in the nozzle performance considering the disparity between the two mesh densities suggests that the model is indeed grid independent.

3.5.2 Validation Model

The results obtained from FLUENT for the validation model can be summarized with a plot of the nozzle output thrust vs. the total inlet pressure as shown in Figure 3.12. This plot provides a comparison between experimental data and the FLUENT model results. The nozzle thrust was calculated using a custom field function in FLUENT. The function is defined by Equation 3-5. This equation was used to calculate the thrust output of each individual element of the exit boundary. These values were then summed to provide the overall nozzle thrust output.

$$\tau = \rho * V_x^2 * X - Face - Area * \left(\frac{abs(V_x)}{V_x} \right)$$

Equation 3-5 - Thrust Calculation

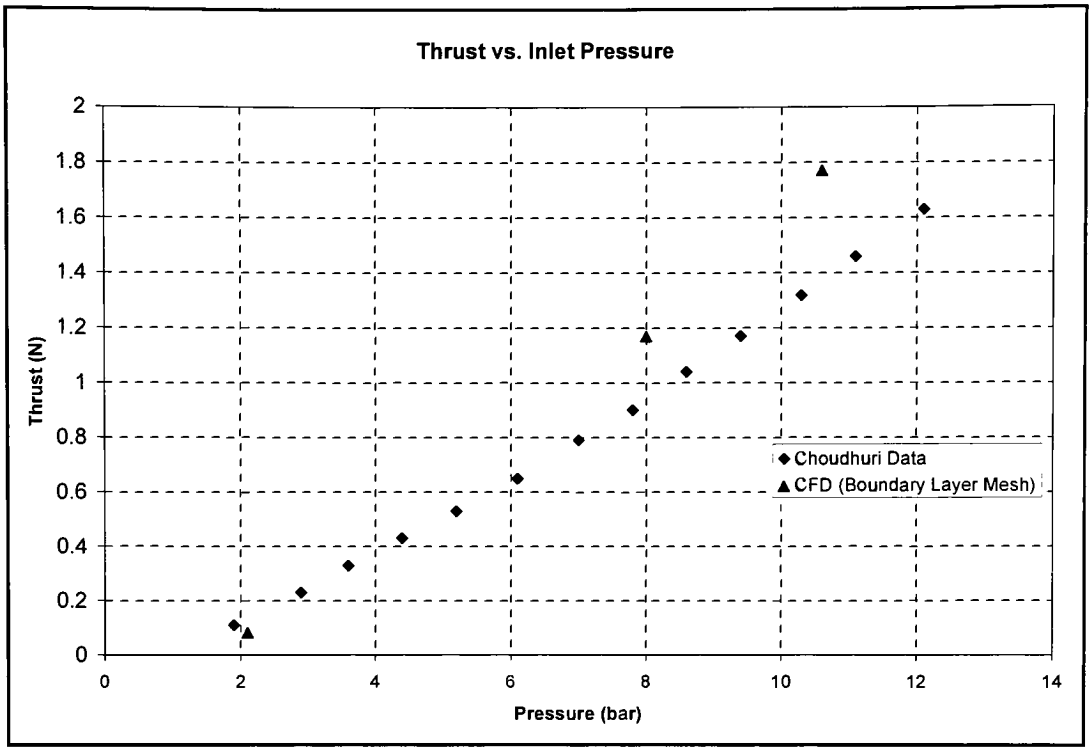

Figure 3.12 - Thrust vs. Inlet Pressure - Validation Model

From Figure 3.12 it is evident the FLUENT results agree reasonably well with the experimental data. The FLUENT results tend to over predict the thrust output values at higher pressures, but the solution is considered to be within an acceptable range to warrant the application of a model to the RIT nozzle. The specific impulse versus the inlet pressure was also plotted for both the Choudhuri and CFD data, and is shown in Figure 3.13. Both of these plots provide confidence that the CFD model employed is capable of providing accurate nozzle performance data.

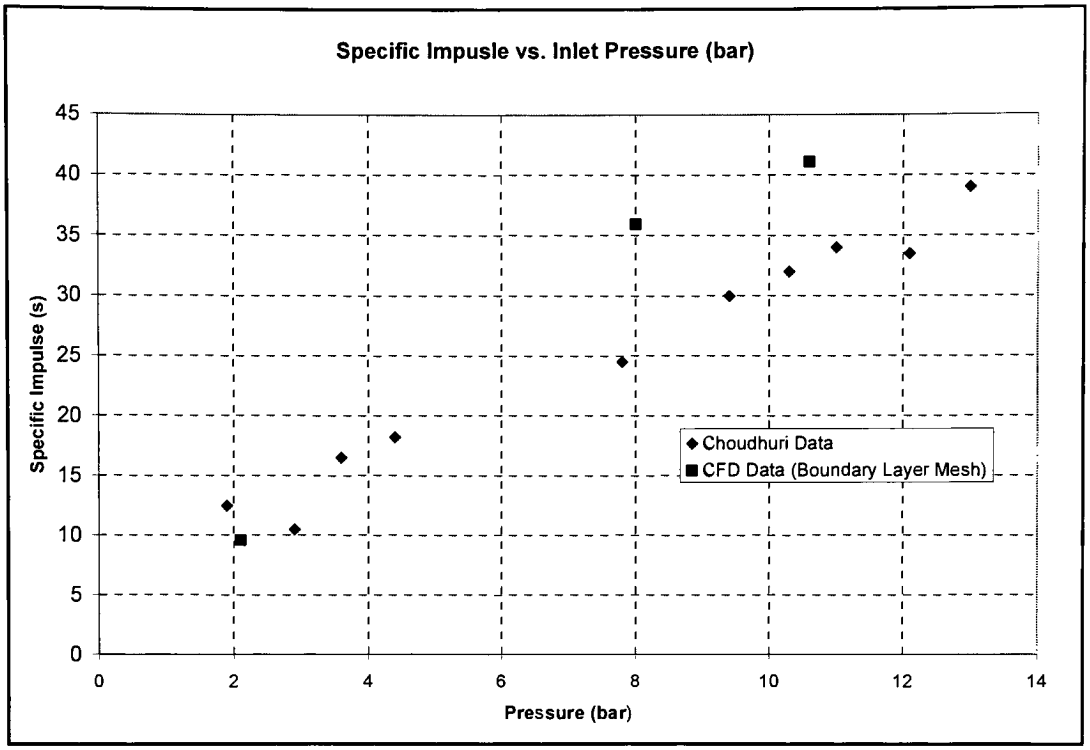

Figure 3.13 - Specific Impulse vs. Inlet Pressure - Validation Model

The trends in the thrust vs. pressure data and specific impulse vs. pressure data are very similar. The flow visualization provided by the CFD model solution, which will be presented shortly, is also in good agreement with the experimental data.

A single case for the validation model will be discussed here. The case described fully in this section has a total pressure inlet value of 1060 kPa (153.7 psi).

The following two figures depict the residuals and mass-flow rate monitor plot data characteristic of the cases solved for the validation model. From Figure 3.14 it is evident that the residual data never reach the default convergence criteria value of 1×10^{-3}, but the monitor data, shown in Figure 3.15, and flux reports were sufficient to assume solution convergence.

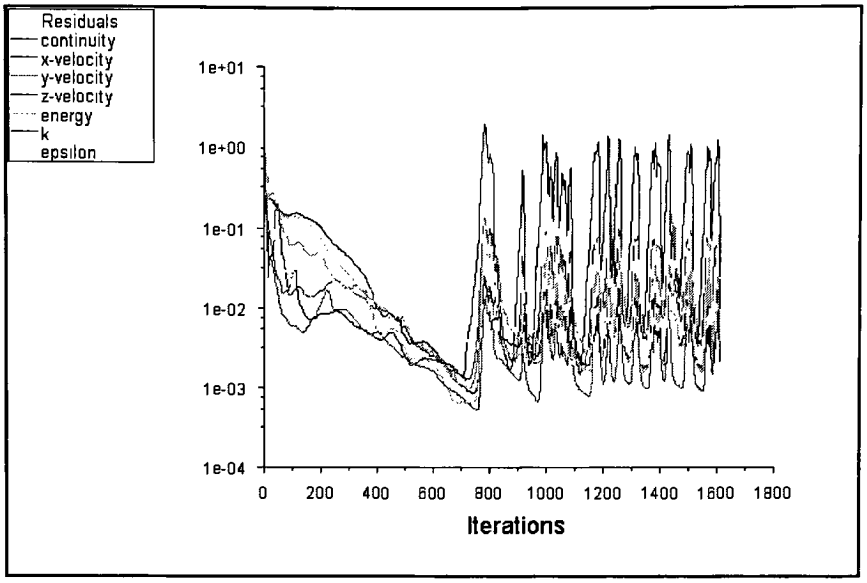

Figure 3.14 - Residual Data - 10.6 bar Inlet - Validation Model

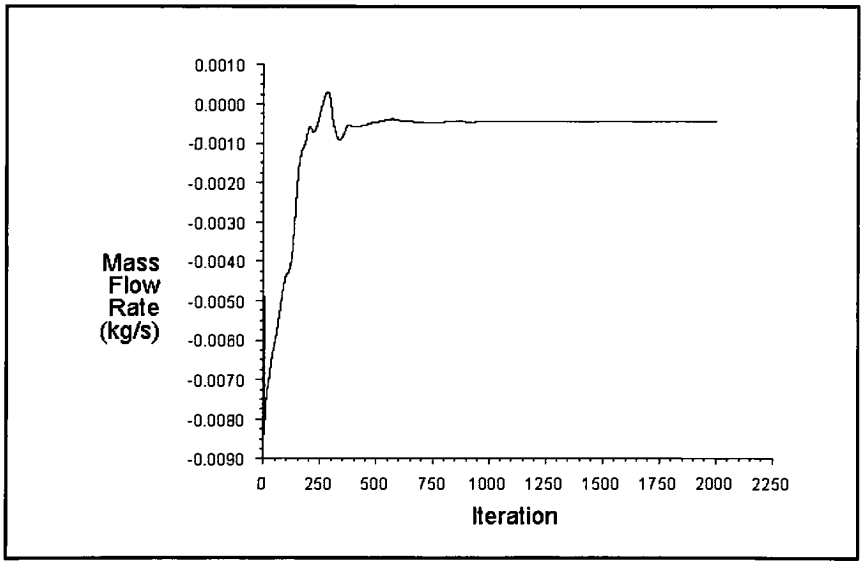

Figure 3.15 - Monitor Data - 10.6 bar Inlet - Validation Model

Figure 3.16 is a plot of the Mach number contours for a plane located at the midpoint of the nozzle thickness. The result is intuitively correct. The flow does not reach a Mach number of one until the throat and proceeds to accelerate to a Mach number of approximately 3.4 in the divergent section of the nozzle, before a series of shocks reduce the flow speed.

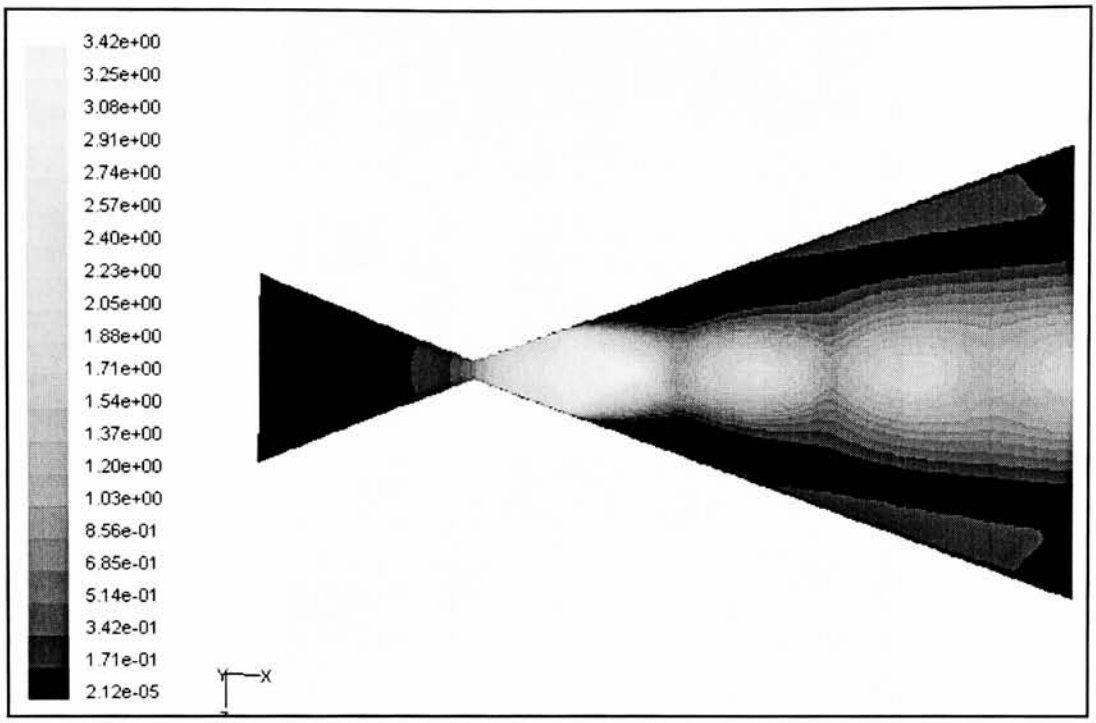

Figure 3.16 - Contours of Mach Number - Validation Model

The diamond shock pattern evident in the nozzle exit may not be expected, but is validated by means of experimental results. Choudhuri et. al. used Schlieren photography during nozzle thrust testing to obtain a qualitative understanding of the flow behavior. Schlieren photography is used to detect density gradients in the flow, which provides insight into separation and shock location in supersonic flows. Figure 3.17 shows a side by side comparison of the density gradient in the nozzle exit obtained experimentally from Schlieren photography and numerically from FLUENT.

Experimental
(Choudhuri et al.)

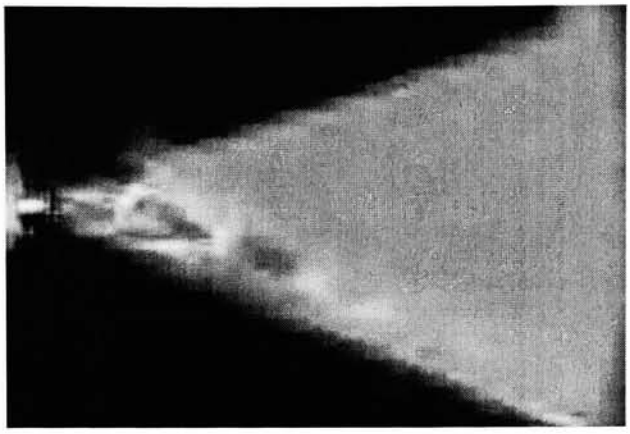

CFD

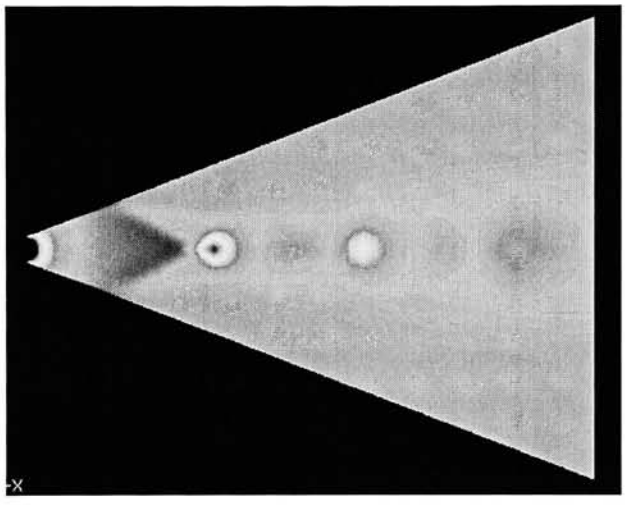

Figure 3.17 - Density Gradient - Validation Model

The agreement between the two flow visualizations is good. Both depictions confirm the diamond shock pattern as a result of the normal shock bouncing off of the nozzle walls. Also, the lengthwise locations of the shocks are similar. The fact that the shocks do not lie along the centerline in the experimental case is due to perturbations in the flow caused by wall imperfections. This is not a fundamental flow characteristic, and manufacturing techniques could possibly be modified to eliminate this flow behavior.

One concern with three-dimensional nozzles of this scale is the loss of performance due to viscous effects. Figure 3.18 is a vector plot of Mach number on the symmetry plane at the nozzle exit.

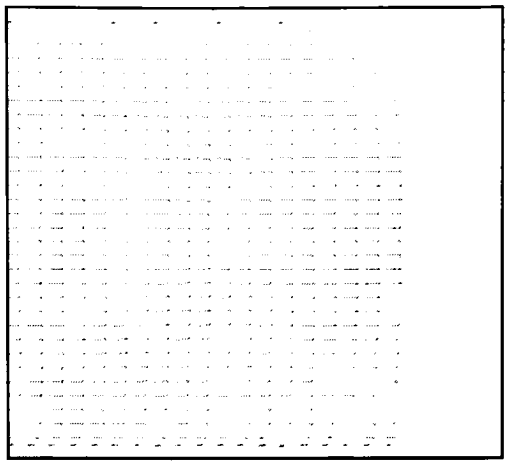

Figure 3.18 - Vector Plot of Mach Number - Symmetry Plane - Exit - Validation Model

From this figure it is easy to see that even at the exit, the boundary layer has not filled the core flow

While the velocity contour plot conveys the presence of a diamond shock pattern, the shock pattern can be clearly viewed in a plot of the static pressure along the length of the nozzle's centerline shown in Figure 3.19. The shocks do not appear to be very strong as the pressure discontinuities are not significantly large, but the shock presence is verified by this plot.

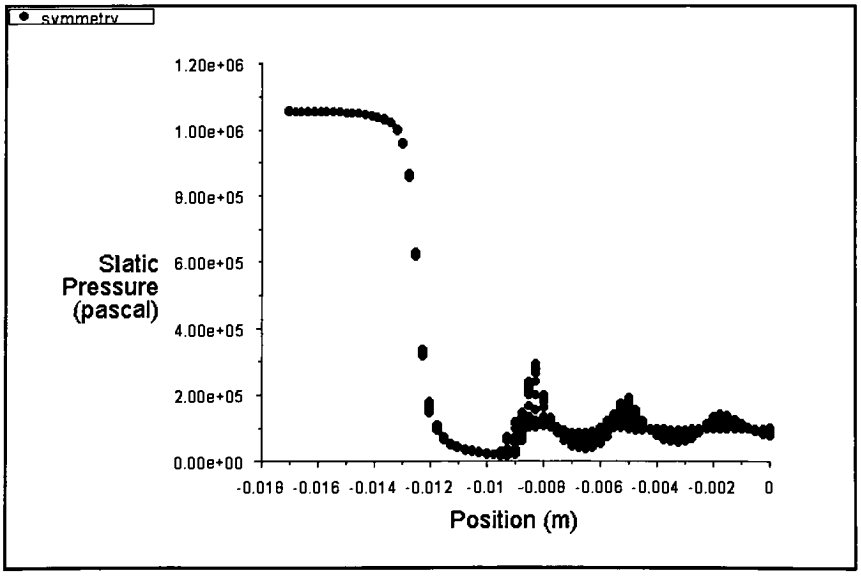

Figure 3.19 - Static Pressure Along Symmetry Plane – Validation Model

The results obtained from the FLUENT validation model are in good agreement with the experimental results obtained by Choudhuri et. al. This verifies FLUENT's ability to model high speed nozzle flows on this scale. Therefore, a model characterizing the performance of the RIT nozzle should provide practical and valid flow information.

3.5.3 RIT Nozzle

Plots of velocity and static pressure will be presented for the RIT nozzle. This will allow for a characterization of the flow field both with and without active flow control (AFC) to define the diaphragm's affect on the nozzle flow. Two cases will be presented; one without flow control and one with flow control defined by the silicone membrane pressurized at 414 kPa (60 psi). Two other cases were modeled with diaphragm pressures of 207 kPa (30 psi) and 621 kPa (90 psi). The results from these models will be summarized at the conclusion of this section of the report. The residuals and mass-flow rate monitor plots are very similar to that shown in the validation model results section. Therefore, they will not be shown here.

The first set of figures (Figure 3.20 and Figure 3.21) represents the velocity contours of Mach number near the nozzle throat for a plane cutting through the center of the nozzle thickness.

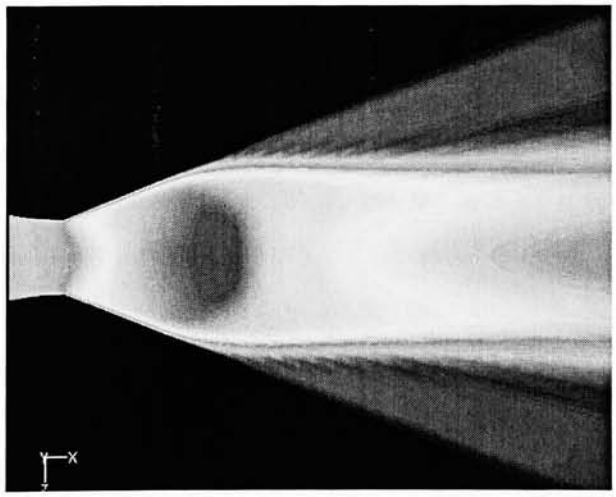

Figure 3.20 - Mach Contour – Original – RIT Nozzle

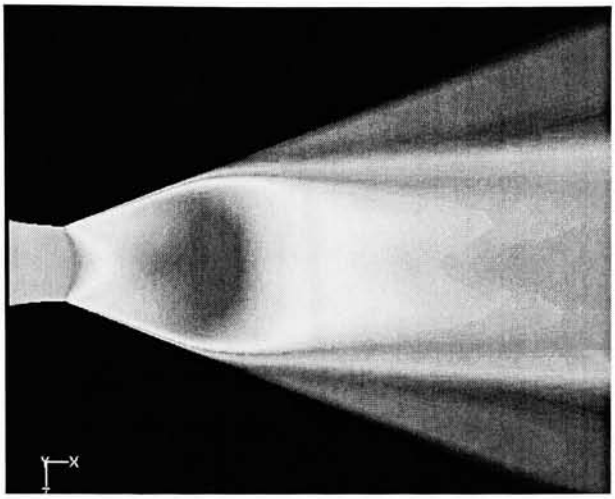

Figure 3.21 - Mach Contour – AFC – RIT Nozzle

The Mach contour of the original nozzle shown in Figure 3.20 portrays a larger region of high speed flow than the nozzle with AFC shown in Figure 3.21. The reason for this result will be discussed shortly. It should also be noted that in the nozzle with AFC the maximum speed of the flow is 2.36 while the original nozzle has a maximum speed of 2.35. This is expected with the introduction of the silicone diaphragm in the flow. The nozzle geometry remains unchanged; but the throat area is decreased, which increases the effective expansion ratio of the nozzle, leading to a higher maximum fluid speed. This same trend appears in the isentropic analysis.

From the Mach contours last presented it is unclear whether or not a shock is present in the nozzle exit. Figure 3.22 provides insight into this query. Figure 3.22 represents the static pressure along the symmetry plane of the nozzle with AFC. The small upward jump in static pressure hints at the presence of a shock, but the lack of a diamond shock pattern suggests other phenomena are possibly at work.

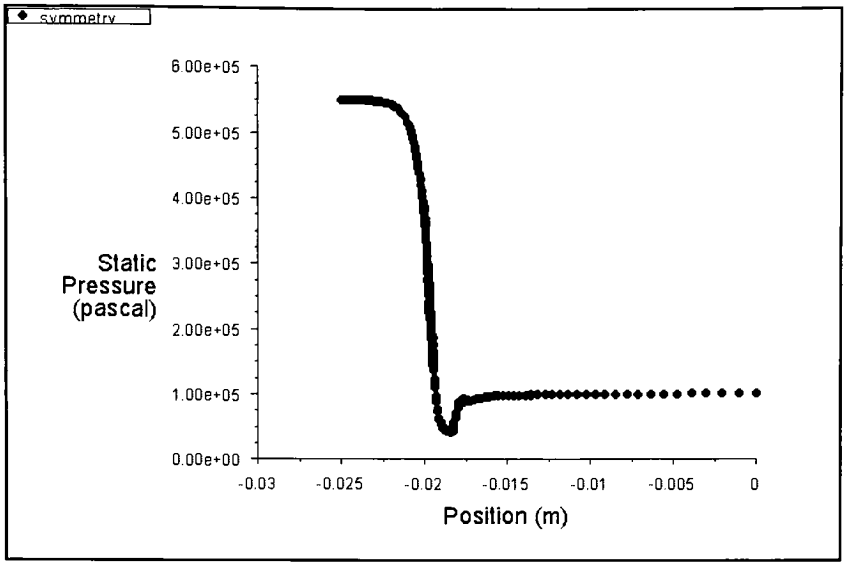

Figure 3.22 - Static Pressure Along Symmetry Plane - RIT Nozzle – AFC

Figure 3.23 depicts the velocity vector plot along the symmetry plane for the nozzles with and without flow control.

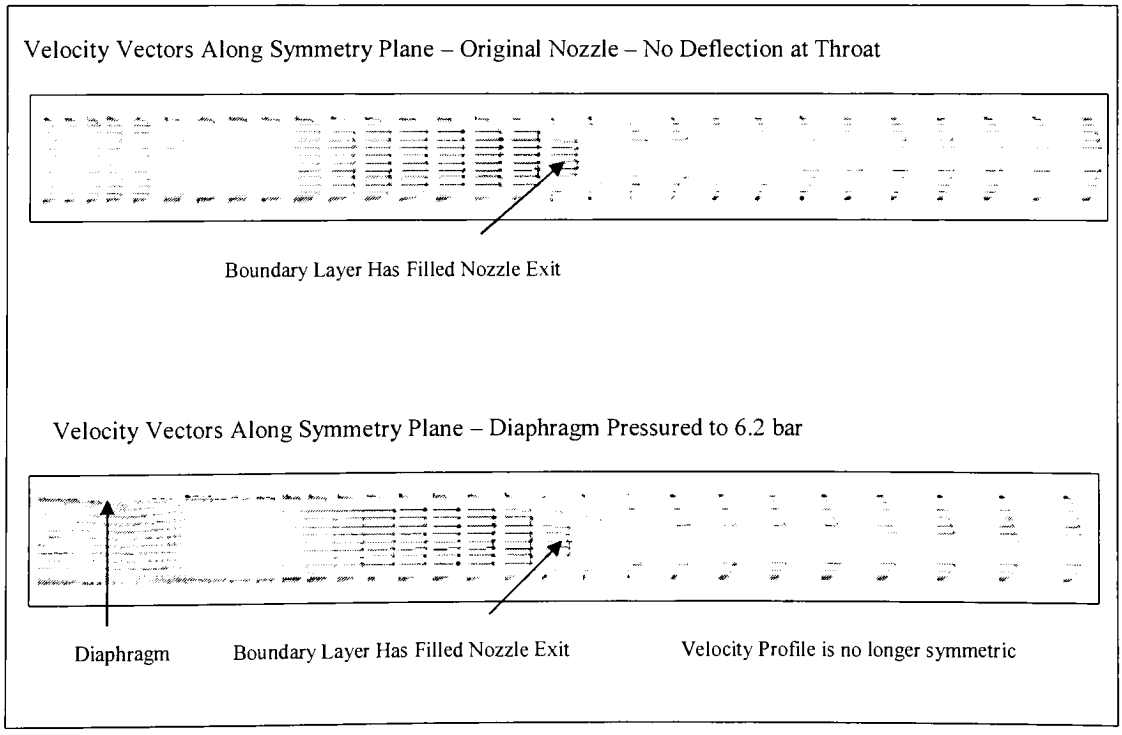

Figure 3.23 - Velocity Vector Plot Along Symmetry Plane

From these plots it is easy to see that the deceleration of the flow is partially due to viscous effects. The boundary layer fills the nozzle well upstream of the nozzle exit. This viscous transition from supersonic to subsonic flow is logical, but not intuitive. It is due to the low aspect ratio of the RIT nozzle. These highly dominant viscous effects are likely the reason for the differences between the Mach contours depicted in Figure 3.20 and Figure 3.21. One possible explanation is that the AFC is causing the shock wave to move upstream, which strengthens the effect of the shock on the fluid speed. This results in a more rapid deceleration in the flow. Another interesting phenomenon is the asymmetric velocity profile due to the silicon diaphragm on the upper surface of the nozzle throat.

A good quantification of the silicone diaphragm's effect on the nozzle flow is the thrust output of the nozzles. Table 3.9 shows the nozzle performance data for the nozzles with and without flow control. The thrust output is calculated in the same manner described by Equation 3-5.

Model	Pressure Inlet (kPa)	Mass Flow Rate (g/s)	Isp (sec)	CFD Model Thrust (N)
Original (No Deflection)	552	0.2275	15.75	0.0337
Diaphragm Pressure of 207 kPa	552	0.2242	14.87	0.0316
Diaphragm Pressure of 417 kPa	552	0.2173	14.73	0.0310
Diaphragm Pressure of 621 kPa	552	0.2126	14.37	0.0296

Table 3.9 - Thrust Output

It is important to note that the thrust, mass flow rate, and specific impulse all have decreased with increasing membrane deflection, as expected. The effect from case to case is small, but the diaphragm can be deflected further into the nozzle flow to provide a larger effect on the flow field.

The CFD analysis provides good insight into the expected nozzle performance during experimental testing both with and without flow control. The CFD results also allow for flow visualization, which is helpful in understanding the driving forces behind nozzle performance in a flow regime which is still not entirely understood. However, it should be noted that the CFD results can only act as an approximation to the actual flow behavior. Several factors, such as surface roughness or membrane distortion, which are present in the actual device, are not accounted for within the CFD model.

4 Fabrication

4.1 Nozzle

4.1.1 Fabrication Options

The method of fabrication is critical because it determines the device cost, wall surface finish, and ultimately effects overall system performance. Several fabrication options are available for a device of this size and geometry. The three options researched were wire electrical discharge machining (EDM), Neodymium Yttrium-Aluminum-Garnet (Nd:YAG) laser cutting, and the use of Microsystems fabrication tools. Due to the thin nature of the micro-nozzle, the nozzle must be constructed of a very stiff material. This vastly affected the methods of fabrication. The following sections are devoted to the methods of fabrication of the nozzle profile. A detail drawing of the nozzle profile is contained within the Appendix in Figure C.5.

4.1.1.1 Wire EDM

Wire EDM is a cutting process that removes material by spark erosion. In simple terms wire EDM works like a high precision band saw. A charged wire and a dielectric fluid are fed through the work piece continuously. The dielectric fluid initially behaves as a resistor until the voltage is high enough for the fluid to ionize, which causes a spark to occur between the wire and the work piece. This spark, which melts and vaporizes the work material, is what actually completes the cutting process. Using this process, accuracies up to +/- 0.005 mm (0.0002 in) are possible (Sommer, C. & Sommer, S., 2000).

The smallest feature on the micro-nozzle is the nozzle throat, which has a width of 0.6 mm (0.0118 in). Wire as small as 0.05mm (0.002") thick can be used, which in general has a kerf of 0.075mm (0.003 in). Therefore, this size wire would be capable of cutting the small features of the micro-nozzle. Furthermore, surface finish is very good. Surface finishes as low as 12 RMS are possible with secondary finishing operations.

Material selection is critical due to the thin nature of the nozzle. This is where the wire EDM process is advantageous. It is capable of cutting a wide range of materials including stainless steels, titanium, and carbide. Carbide was selected as the material of choice, primarily for its stiffness.

Unfortunately, the costs of machine setup and material are prohibitive. It should be noted that even with the fine finish possible with EDM, wall imperfections have been shown to be large enough to affect the overall flow behavior. Choudhuri et al. used micro-nozzles fabricated by this process, and asymmetrical flow was present due to wall imperfections. Even so, the wire EDM process is a capable and ideal process for fabrication of micro-nozzles. The costs, however, are prohibitive.

4.1.1.2 Micromachining

Micromachining refers to the fabrication process that utilizes the fabrication techniques and tools used in semiconductor processing. With this in mind, the material selection is primarily limited to silicon wafers. The techniques and tools used in semiconductor processing are in general limited to devices with dimensions on the order of one to a few microns. The device being fabricated in the current study has a minimum feature size of 0.6 mm (0.024 in). This is very large for this fabrication process, but the accuracy of the tooling allows for the device to be constructed with incredible accuracy and low surface roughness. This is its primary advantage.

This fabrication process was pursued nearly until completion at the RIT Semiconductor and Microsystems Fabrication Laboratory (SMFL). Unfortunately, due to equipment availability, this method of fabrication was abandoned. The fabrication steps completed in the lab along with the necessary fabrication steps that were not able to be completed will be presented here. Figure 4.1 shows a basic process flow for the fabrication of the micro-nozzle.

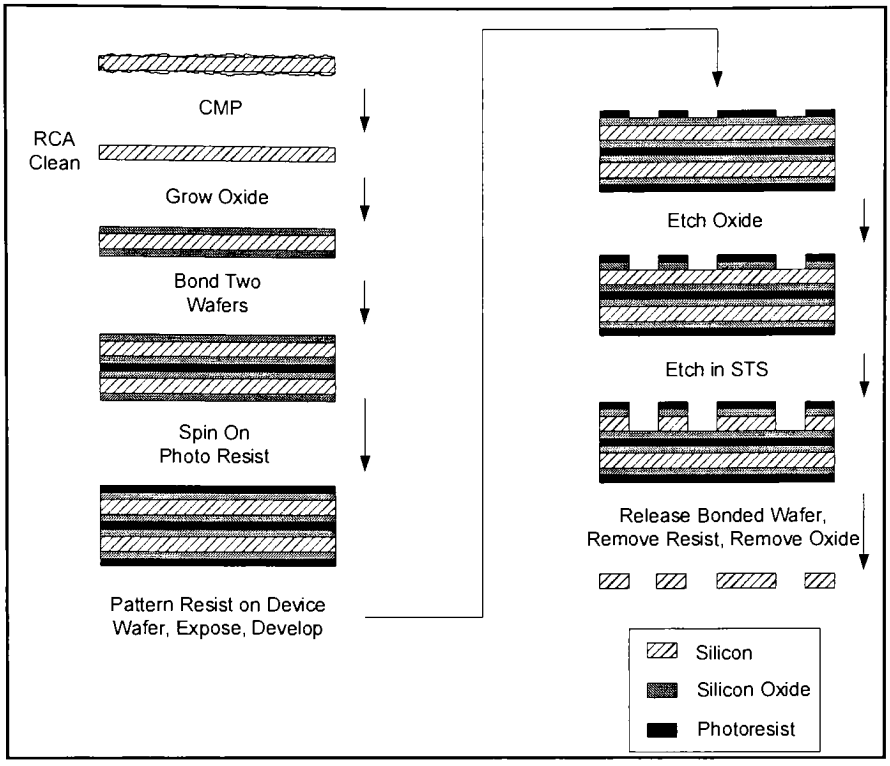

Figure 4.1 - Overview of Fabrication Microsystems Fabrication Process

The fabrication process began with a 0.3 mm (0.012 in) thick lapped silicon wafer. Due to the surface finish of the lapped wafer, preliminary processes were necessary before entering the clean room. Before a mask or deposition layer is added to the wafer surface, the surface finish must have peaks and valleys of amplitude less than at most a few microns. In order to achieve this surface finish from a lapped wafer, a chemical mechanical polish (CMP) was necessary. Both sides of the wafer must be polished due to future process requirements. The Strausbaugh CMP Tool was used for this process. Initially the processing specifications contained in Table 4.1 were used.

Slurry	Lavisil 100/45% KLVP ph>11
Length of Polish	20 min per side
Drip Rate	~1 drop per second
Down Pressure	8 psi
Quill Speed	70 RPM
Oscillation Speed	6 per minute
Table Speed	50 RPM (~10 Hz)

Table 4.1 - Strausbaugh CMP Process Specifications

This initial polishing proved to be unacceptable as the divots in the wafer surface were still too numerous and too deep. Further polishing was necessary. The setup remained the same accept the slurry was changed to Lavisil 50CK-862/30% KLVP due to availability. After a CMP of another 15 min the wafer surface looked as it is shown in Figure 4.2.

Figure 4.2 - Wafer Surface After 35 min. of CMP

The number of divots in the wafer surface was still numerous, and their depth was estimated at 2-3 μm (79 – 118 μin). It was necessary to continue polishing the wafers. After another 5 minutes the wafer was checked once again. More polishing was necessary. The wafer was

polished for another 15 minutes, for a total of 55 minutes of polishing for a single side of a single wafer. The resulting surface finish is shown in Figure 4.3.

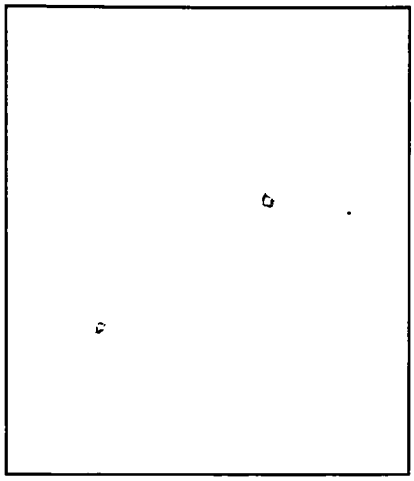

Figure 4.3 - Wafer Surface After 55 min. of CMP

The number of divots in the wafer had decreased significantly through polishing. The divots left in the wafer surface were estimated to have a depth of approximately 2 μm (79 μin).

Before any processing is completed on the wafer an RCA clean is necessary. An RCA clean is used to clear the wafer surface of contaminants before processing. This process, shown in Figure 4.4, consists of three major steps. Step '1' as labeled in Figure 4.4 is an organic clean to remove insoluble organic contaminants. Step '2' as labeled in the process figure removes a thin silicon dioxide layer, where metallic contaminants tend to accumulate. Step '3' as labeled in Figure 4.4 is an ionic clean, which removes heavy and ionic metal atomic contaminants. Once this cleaning process has been completed, the wafers are ready for processing.

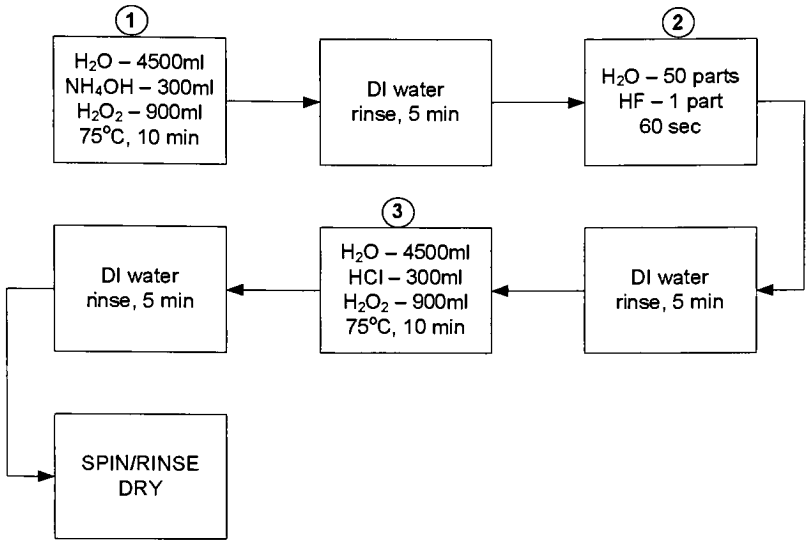

Figure 4.4 - RCA Clean Process Chart

Surface oxide growth is the next step in the wafer processing sequence. The oxide growth was completed in the Bruce Furnace Tubes located in the RIT SMFL. The deposition of the oxide layer is necessary to act as a mask for the final etch process. Due to the selectivity of the STS Deep Trench Etcher, which will be used to etch out the nozzle profile, at least a 10 μm (478 μin) thick oxide mask layer is necessary to etch through a 300 μm (0.012 in) thick wafer. Bruce Furnace Tubes are used to produce the thick silicon oxide layer. Upon removal from the Bruce Furnace Tubes the oxide thickness was measured using a Tencor SpectraMap SM300. Using this tool, the oxide thickness was found to vary from approximately 12.1 to 12.2 μm (approximately 478 μin). This was more than acceptable to proceed onward with processing.

The next step in the fabrication process is wafer bonding. This is necessary because of the large etch area. Without a support layer bonded to the device wafer, the wafer would shatter under the thermal and mechanical stresses inherent in the final etch process. Several bonding options are available. For a non-permanent bond, two wafers could be bonded using photo-resist as a bonding agent or intermediate layer. This would provide a bond strong enough for the etch process, but the support wafer could be released by an acetone soak. Other options include more permanent bonding techniques such as a thermal oxide bond. A thermal oxide bond uses thermal oxide as an intermediate layer. Two clean and flat wafers

coated in thermal oxide are pressed, and then heated to 1100 °C while a voltage of 10 to 30 V is applied across the wafers. This results in a permanent bond between the two wafers. In the current study the non-permanent bond utilizing photo-resist as an intermediate layer was used. After bonding, photo-resist must be spun on both sides of the wafer stack to provide a mask for photolithography. The resist layer thickness must be at least 12 μm (472 μin), which requires the use of a highly viscous resist. The thick resist layer is necessary to act as an additional mask layer in the etch process.

The next step in the fabrication process is to pattern, expose and develop the photo-resist layer. This set of processes is known as photolithography. The nozzle profile is patterned on the wafer surface using a contact mask containing the nozzle layout. The mask is made up of a copper plated quartz sheet. The copper is etched with the desired pattern from a CAD model source file. This mask is then used with a contact printer such as the Suss MA 150 available in the SMFL. Once the proper exposure time is calculated, the wafer can be exposed. Then the wafer is developed in an acetone bath, which for a positive photo-resist will remove resist only in the exposed areas of the wafer surface.

The final step before etching the silicon is to remove the silicon oxide in the previously exposed portion of the wafer. This is completed through a Buffered Oxide Etch (BOE). For a 12 μm (472 μin) thick oxide layer an etch time of approximately 15 minutes is necessary. The photo-resist is not removed during the BOE, therefore the pattern of the resist layer is transferred to the oxide layer. Once this is complete, bare silicon will be visible in the desired etch region.

The next step is to etch the device using the STS Deep Trench Etcher. Once the etch has proceeded through the wafer, the two wafers can be released by an acetone soak. This will remove the remaining photo-resist. Another BOE etch is necessary to remove the remaining silicon oxide. Finally, each device is diced from the parent wafer.

While this process was not used due to equipment availability, it is advantageous for its accuracy and ability to achieve high quality surface finishes. The fabrication process is also very advantageous if future work demands miniaturization or batch fabrication.

4.1.1.3 YAG Laser Cutting

YAG laser cutting utilizes the cutting power of a Neodymium Yttrium-Aluminum Garnet laser. The laser is contained within a thin water jet, which cools the cutting face. The

low pressure jet exerts little mechanical force on the part being cut. The cutting device has a precision of 0.001 mm (39 μin) and an accuracy of 0.003 mm (118 μin). Surface roughness is unknown. The laser cutting tool is capable of cutting a variety of materials including ferrite, silicon, silicon nitride and synthetic diamond. The minimum water jet nozzle diameter is 0.050 mm (0.002 in) with a kerf as small as 0.05 mm (0.002 in). Therefore, the smallest feature size possible with this cutting device is approximately 0.1mm (0.004 in). The RIT nozzle has a minimum feature size of 0.6 mm (0.024 in), and consequently is a good candidate for the laser cutting process.

The laser cutting process was used to create the nozzles experimentally tested in the current study. The Synova LCS 300 laser micro-jet cutting system was used to cut the nozzle profile from a 0.3 mm (0.012 in) thick silicon wafer. The nozzle profile data was imported using an AutoCAD two dimensional drawing. The detailed tool settings for each cut are contained within the Appendix. A slight burr existed on the wafer edge after the cut was completed. Photos were taken of the cut surface to try to quantify the surface finish. Surface finish is important in high speed flow because wall imperfections can create shocks or even cause asymmetric flow, as was shown by Choudhuri et. al. Figure 4.5 shows a photo of the laser cut edge at 100x magnification. From this photo it looks as if the laser did not cut completely through the surface before the device separated from the wafer. There appears to be two distinct regions on the cut surface. One region appears fairly smooth with small grooves directed across the thickness.

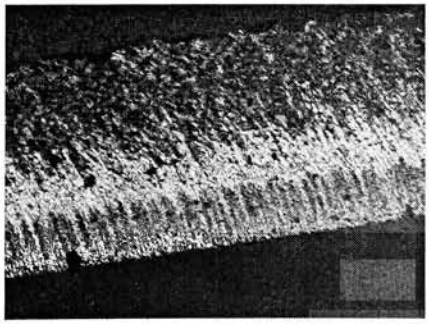

Figure 4.5 – Laser Cut Edge at 100x Magnification

The other region appears to be rougher with no directivity. The grooved surface looks to be the laser cut portion which makes up about one-third of the wafer thickness. The other region

seems to be from a fracture, which occurred as the device fell from the wafer before the cut completed. A value for the surface finish was not obtained, but from the photo it is estimated that the surface finish be on the order of 5 – 10 μm (197 – 394 μin). Figure 4.6 shows the same surface at 200x magnification.

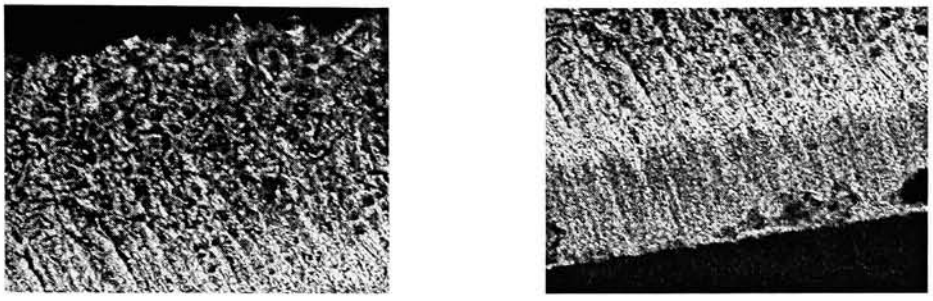

Figure 4.6 - Laser Cut Edge at 200x Magnification

It is likely that this surface finish could affect the nozzle performance. Possibly future work can investigate nozzle wall surface roughness effect on nozzle performance. The final nozzle is pictured below in Figure 4.7.

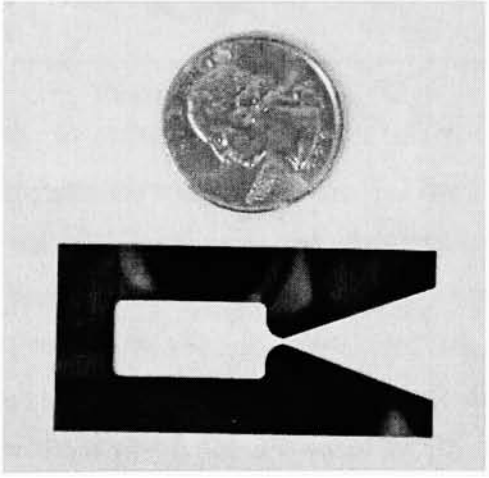

Figure 4.7 - Photo of Final RIT Nozzle

4.2 Casing and Actuation Device

The casing is constructed of several layers that are sandwiched to form the final device. A figure of the basic stack-up is shown in Figure 4.8. The upper and lower surfaces

are constructed of ¼ inch thick aluminum milled to the nozzle width and length. The upper surface has two pressure inlets; the leftmost inlet in Figure 4.8 is for the pressurization of the silicone membrane, while the right inlet is the propellant inlet. Detail drawings of the aluminum surfaces are contained in Appendix C. The clamp device used in the actual assembly is discussed within the Test Setup Section of this report.

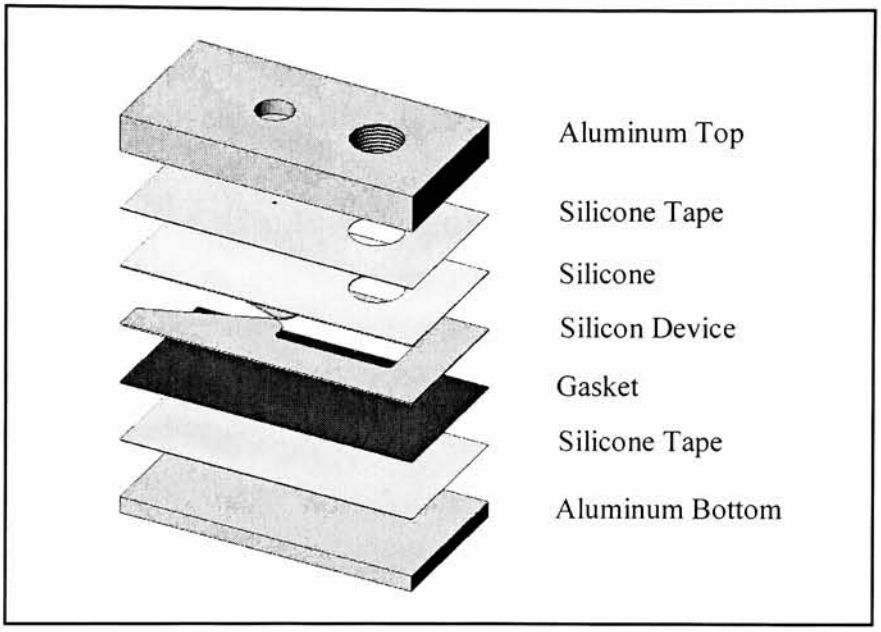

Figure 4.8 - Nozzle Stack Up

The fabrication of the silicone actuation device was not a trivial task. The difficulty came in the adhesion of the silicone sheet to the aluminum block. It must be attached securely enough to handle pressurization to 207 kPa (30 psi) without excessive pealing. This was accomplished using F-9469PC 3M silicone double sided tape. While this is effective for a short series of tests, it does not provide a bond strength high enough to be used in an actual application. A more reliable fabrication procedure would involve the Sylgard 184 silicone in a spin on process, which would allow the silicone to cure on the nozzle wall. This process will be discussed further in the conclusions and recommendations section of this report.

5 Testing

5.1 Test Setup

The primary application of the supersonic nozzle with active flow control (AFC) is thrusting in micro or nano-satellite systems. Therefore the major nozzle performance properties of interest are the nozzle output thrust, coefficient of discharge (C_d), and specific impulse. For these reasons it is important that during testing, the inlet pressure, upstream temperature, flow rate, and nozzle thrust are measured and recorded. These parameters will provide sufficient information to calculate the nozzle performance characteristics. The testing methodology is as follows; the pressure, flow rate, upstream temperature, and thrust are to be recorded as the inlet pressure is varied from 68.9 kPa (10psi) to 689 kPa (100 psi).

Two slightly different test setups were necessary. One test setup was used to test the micro-nozzle without AFC, the other with AFC. Similar data was taken in each; except in the latter an additional pressure inlet was necessary.

5.1.1 Setup Without Active Flow Control

Initial testing was completed on the nozzle without AFC. In order to prevent leakage out of the device during operation at high pressures, a clamp was designed and built. A stack up of tape, gasket material, and 2024-T4 aluminum plates is used to minimize leakage while protecting the fragile nature of the silicon nozzle as it is clamped down. The stack up is shown in Figure 4.8. The upper aluminum support has two inlets. The rightmost inlet of the upper aluminum support in Figure 4.8 is tapped with 1/8" – 27 NPT thread. This provides the flow inlet to the nozzle. The remaining inlet is only of use during activation of AFC. The silicone tape is used to adhere the silicone sheeting to the upper aluminum support. It is important that no air pockets remain between the silicone sheet and the aluminum block. Due to the thin nature of the nozzle, even a small air pocket could create an obstruction in the flow. On the lower half of the nozzle stack-up, silicone tape is used to adhere the gasket layer to the lower aluminum support. The entire device is held together using a clamp fastened with ten #8-32 thread screws. A photo of this is shown in Figure 5.1.

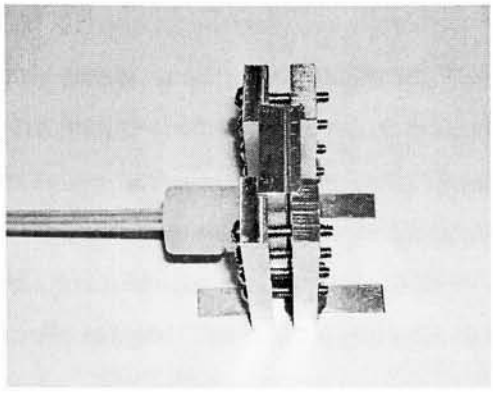

Figure 5.1 - Micro-Nozzle Assembly

The clamped assembly is slowly tightened to prevent the brittle silicon nozzle from cracking. The clamp is tightened until the leakage is negligible. Two aluminum sheet runners are added to the bottom of the assembly to promote stability when mounted on the thrust stand.

The overall test setup is shown below in Figure 5.2. The flow source is a compressed air tank which is regulated at the tank outlet. The air is breathing quality, which is dryer and cleaner than the available 'shop air.'

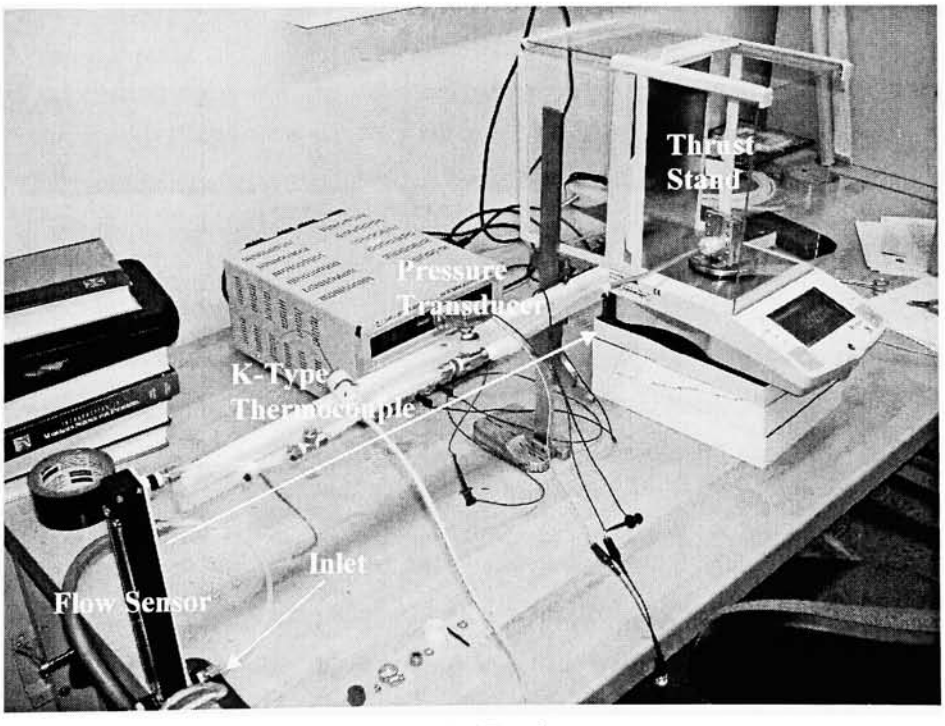

Figure 5.2 - Test Setup

The air first enters the flow sensor, a 150 mm rotameter. The air exits this sensor and proceeds through ¼" nylon tubing before entering a t-coupling fitted with a k-type thermocouple. The flow exits the t-coupling and proceeds through more ¼" nylon tubing before entering another t-coupling fitted with a pressure transducer. From this point the air enters ¼" Tygon tubing until it reaches the micro-nozzle assembly, which is mounted on the weighing stage of an electronic balance. The basic specifications of each sensing device are listed in Table 5.1.

Transducer	**Rotameter Flow Sensor**	**K-type Thermocouple**	**Pressure Sensor**	**Thrust Stand**
Manufacturer	Omega	Omega	Omega	Ohaus
Model Number	N034-39ST	K-type Standard	PX242A-100G5V	Voyager Balance VP213CN
Range	16.737 std. L/min	0 - 480°C	0 – 100 psig	210g
Accuracy	+/- 2% full scale	0.1°C	1.5%	+/- 0.002 g
Repeatability	+/- ¼% full scale	0.1°C	+/- 0.1% full scale	0.0005g

Table 5.1 - Test Equipment Specifications

The experimental data was acquired through both live data capture and manual acquisition. The thermocouple and pressure transducer signals were acquired through the Labview software package in conjunction with National Instruments DAQ hardware. Within Labview the transducer outputs were converted to temperature and pressure data. This data was then manually recorded at set intervals throughout the testing process. The OHaus Voyager Balance was interfaced with a PC using an RS232 connection. Using a National Instruments Measurement Studio macro for Microsoft Excel, the balance was operated through a PC interface. During testing a transmission loop was run, which requested and recorded thrust data at the fastest intervals possible over the RS232 connection. Thrust data was manually

recorded at set intervals throughout the testing process in conjunction with the live data capture. Unfortunately, due to the dissimilar interfaces, simultaneously capturing live data of each signal on the PC was never accomplished. The flow sensor required manual readings to be taken at each set interval throughout the testing process.

Due to the low thrust output inherent with micro-nozzles, resolution of the thrust data was of significant concern. The balance accuracy and repeatability specifications were satisfactory, but external sources of error were a considerable issue. As noted earlier, the flow input is perpendicular to the nozzle thrust output. In order to minimize the tubing's effect on the thrust output the final length of tubing is ¼" flexible Tygon tubing. The initial setup, in which nylon tubing was used, proved to be unacceptable as the tubing stiffness caused undesirable amounts of drift in the thrust data. In order to quantify the tubing's effect on the thrust output, several objects were weighed on the balance before and after the addition of the micro-nozzle assembly. This static data showed that the effect of the Tygon tubing is negligible. This data is contained within the Appendix in Figure B.8. Another concern was that during testing, as the tubing is pressurized, the thrust output would vary. Testing has been completed to quantify this effect. The accuracy of the thrust data has been adjusted to represent this tubing effect in the uncertainty. This is discussed further in Section 5.2.1

The testing methodology consisted of taking flow rate, temperature, pressure, and thrust data at 34.5 kPa (5 psi) intervals from an initial pressure of 68.9 kPa (10 psi) to a maximum pressure of 689.5 kPa (100 psi). Input pressure is being estimated by the static pressure transducer. The head loss through the final bend and short section of the tubing is considered negligible. Also, the tube area to throat ratio is approximately 100, therefore the flow speed through the tubing is low enough to assume the equivalency of the total and static pressure. The input pressure is manually adjusted using the valve assembly on the compressed air cylinder.

5.1.2 Setup With Active Flow Control

The basic test setup for the micro-nozzle with AFC is slightly modified from the setup without AFC. The major difference between the two setups is the addition of a second

pressure input and the removal of the flow sensor. The source of the pressure input is 'shop air' from a central compressor located in the building. The air is fed through a large plenum before pressurizing the silicone diaphragm above the nozzle throat. The magnitude of the pressure inlet is controlled by a valve located between the 'shop air' source and the plenum. Using a dial pressure gage with a least count of 2 psi, the pressure is recorded. A schematic of the overall test setup is shown in Figure 5.3.

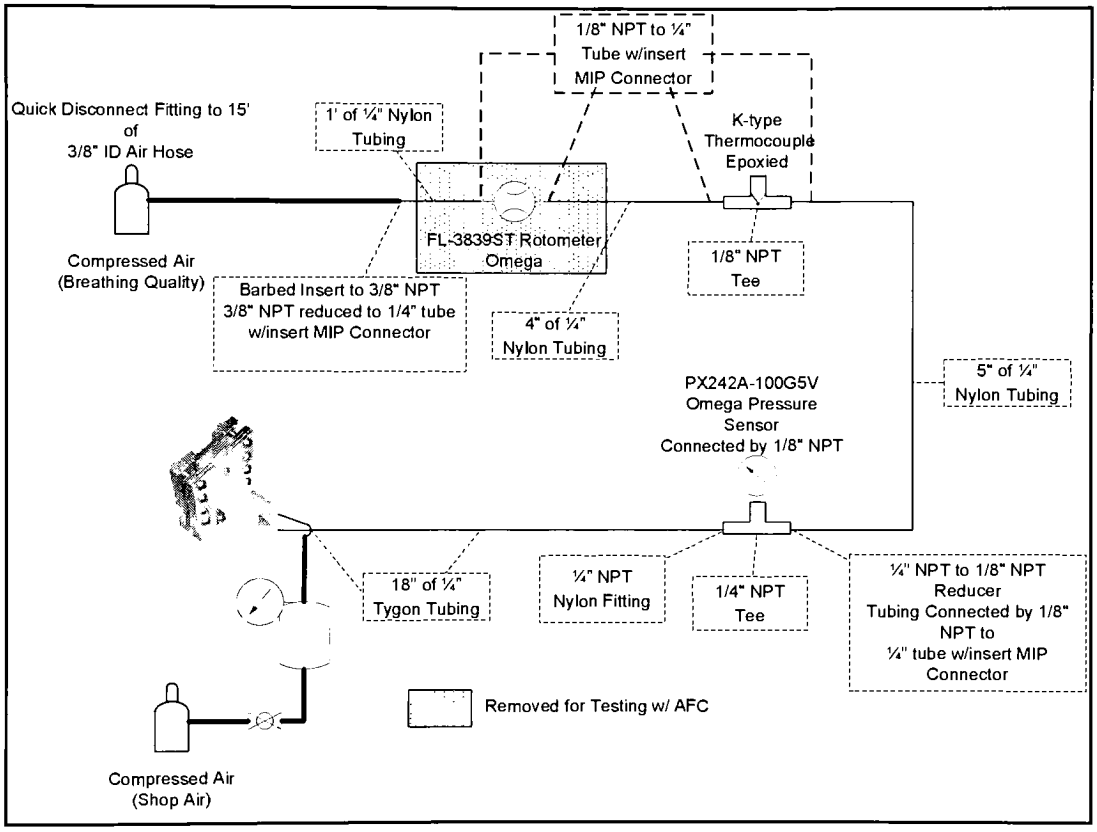

Figure 5.3 - Test Schematic - With AFC

The test procedure for micro-nozzle testing with AFC is nearly unchanged from the test procedure used without AFC. The only difference is that the membrane is pressurized, and the balance is zeroed before taking flow rate, temperature, pressure, and thrust data at 68.9 kPa (10 psi) intervals from an initial pressure of 68.9 kPa (10 psi) to a maximum pressure of 689.5 kPa (100 psi).

5.1.3 Uncertainty

The uncertainty of each device was estimated by the sensor fluctuation during testing and the manufacturer specified uncertainty. The uncertainty values used throughout the uncertainty analysis are shown in Table 5.2

Sensor	Uncertainty
K-Type Thermocouple	2 K
Omega 150mm Rotameter	3% of full scale or 6.834e-3 g/s
Omega Pressure Sensor	1.5% of full scale or 10.3 kPa
OHaus Balance	Variable

Table 5.2 - Sensor Uncertainty

The uncertainties above were used in the uncertainty propagation calculations describe within Appendix D. The thrust uncertainty is variable due to tubing pressurization effects. This uncertainty due to the tubing effect was determined through experimental testing. The results of this testing were averaged and applied to the original thrust data as a bias. By examining the upper and lower bounds of the thrust generated during the tube effect testing, an error bound was estimated. This bound was then increased by 2 mN on either side to account for normal fluctuations during data collection.

The uncertainty in the CFD results was also addressed. A thrust and flow rate uncertainty was determined from the criteria used to judge model convergence. One criterion set for model convergence was that mass conservation had to be satisfied within 5% of the overall mass flow rate. Using this information the uncertainty in the mass flow rate was set at +/- 5%. The flow rate is a function of flow velocity, while the thrust is a function of the square of the flow velocity. Using this relationship, a worst case scenario set the thrust uncertainty at +/- 25%. These uncertainties are used throughout the test results section of this report.

5.2 Test Results

5.2.1 Without Active Flow Control

The testing was completed using the procedure outlined in Section 5.1.1. Figure 5.4 is a plot of nozzle thrust versus upstream pressure. The thrust is expressed in milli-Newtons and the upstream pressure is expressed as gauge pressure. The exit pressure or reference pressure is set at 101.3 kPa (14.7 psi) with an uncertainty of $^{+}$/- 0.5 kPa (.07 psi). This plot represents the averaged data of ten experimental runs. Between the first and second setup the entire test setup was disassembled and reassembled. Unfortunately, the process of clamping down the stack-up shown in Figure 4.8 is not entirely repeatable. Therefore, after reassembly it is likely that more force was applied to the clamp, causing the gaskets to decrease the overall nozzle thickness. Ideally, the exit thickness should be recorded for each setup, as the data from run to run, for a given setup, is in good agreement. The thrust versus upstream pressure data for each run is contained in the Appendix in Figure B.9 and Figure B.10.

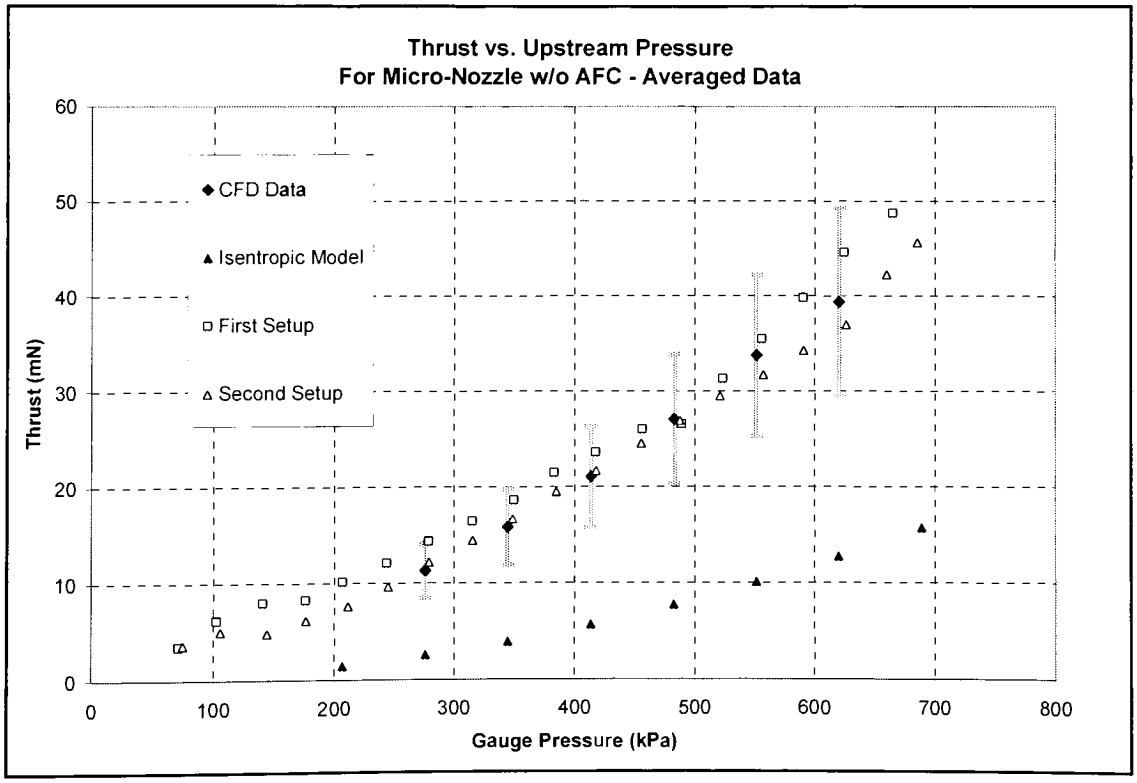

Figure 5.4 - Thrust vs. Upstream Pressure - No AFC

The isentropic model results along with the CFD model results are plotted against the experimental data. The experimental data shown here is inaccurate due to tube pressurization effects. As the tubing is pressurized it stiffens producing a positive thrust. This bias has been estimated through testing, and the nozzle thrust has been corrected to account for this effect. Figure 5.5 shows the final corrected experimental data. Within the experimental uncertainty, the CFD and experimental results are in agreement. However, it is likely that the nozzle thrust is at the lower end of the error range, which the flow-rate data to be presented shortly suggests. The low end experimental thrust output is expected because the gasket interference decreases the nozzle thickness to a value below the modeled thickness of 0.3 mm (0.012 in).

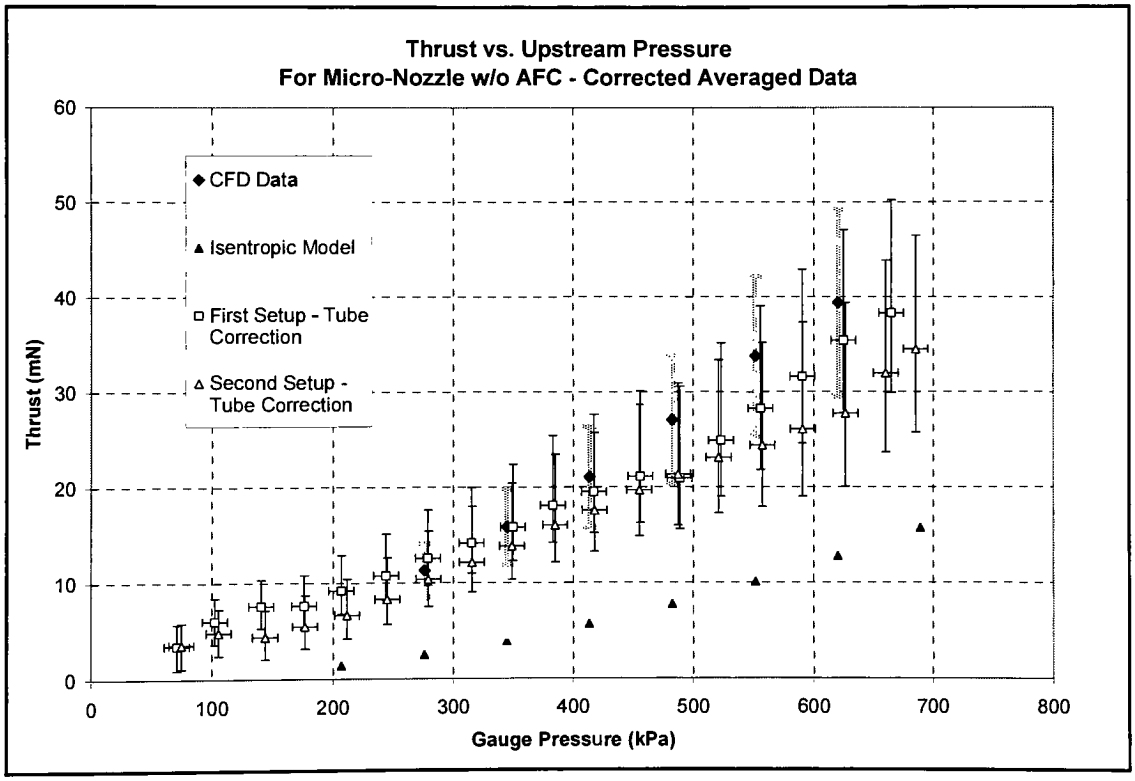

Figure 5.5 - Thrust vs. Upstream Pressure - No AFC - Corrected Data

The isentropic model results are under predicting the thrust output. The isentropic model assumes no losses except those due to the flow separation caused by a normal shock. However, the CFD results do not predict a strong normal shock within the nozzle exit.

Rather, CFD predicts a weak diamond shock, which has been confirmed experimentally by Schlieren photography in a study of similarly sized nozzles (Choudhuri et. al., 2001). The flow energy losses incurred in the weak diamond shock are not as significant as those due to a strong normal shock. Therefore, the isentropic model is effectively over-predicting the losses associated with the flow separation. In fact the isentropic model is predicting separation losses that exceed both the viscous and separation losses encountered in the actual nozzle.

Figure 5.6 is a plot of the flow rate through the nozzle as the upstream gauge pressure is varied. Once again a total of 10 experimental runs are represented on the plot by two sets of points; 'First Setup – No Membrane' and 'Second Setup – No Membrane.' The data for each run can be viewed in the Appendix in Figure B.11 and Figure B.12. Also plotted in Figure 5.6 is the CFD and isentropic model results, along with a dotted line representing the minimum upstream pressure required to achieve choked flow, assuming isentropic compression. Overall, the CFD and isentropic models are in agreement with each other, but are not in agreement with the experimental data. Possible reasons for this behavior will be discussed shortly.

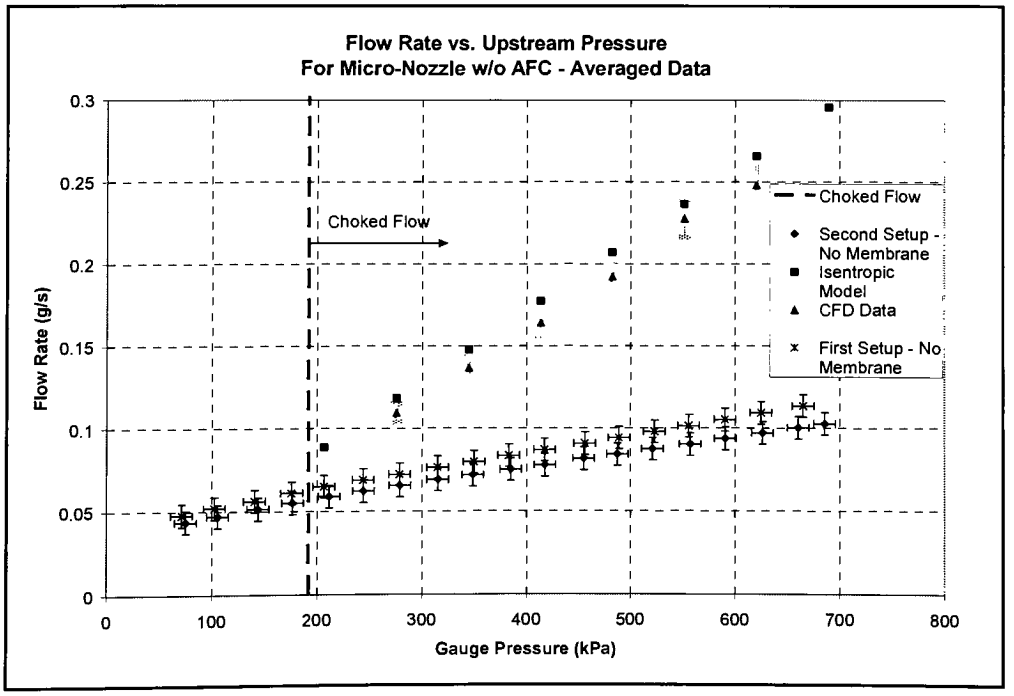

Figure 5.6 - Flow Rate vs. Upstream Pressure - No AFC

It is very interesting to note the change in the flow rate at the theoretical choke point of the nozzle. A zoomed view of the mass flow rate versus inlet pressure for the second setup is shown in Figure 5.7. Theoretically, when the flow becomes choked within the nozzle, the speed of the fluid cannot accelerate above a Mach number of one at the throat. However, the mass flow rate continues to increase as the inlet pressure is increased, due to an increase in the density of the flow. The increase in the mass flow rate after the flow becomes choked should theoretically be linear with pressure.

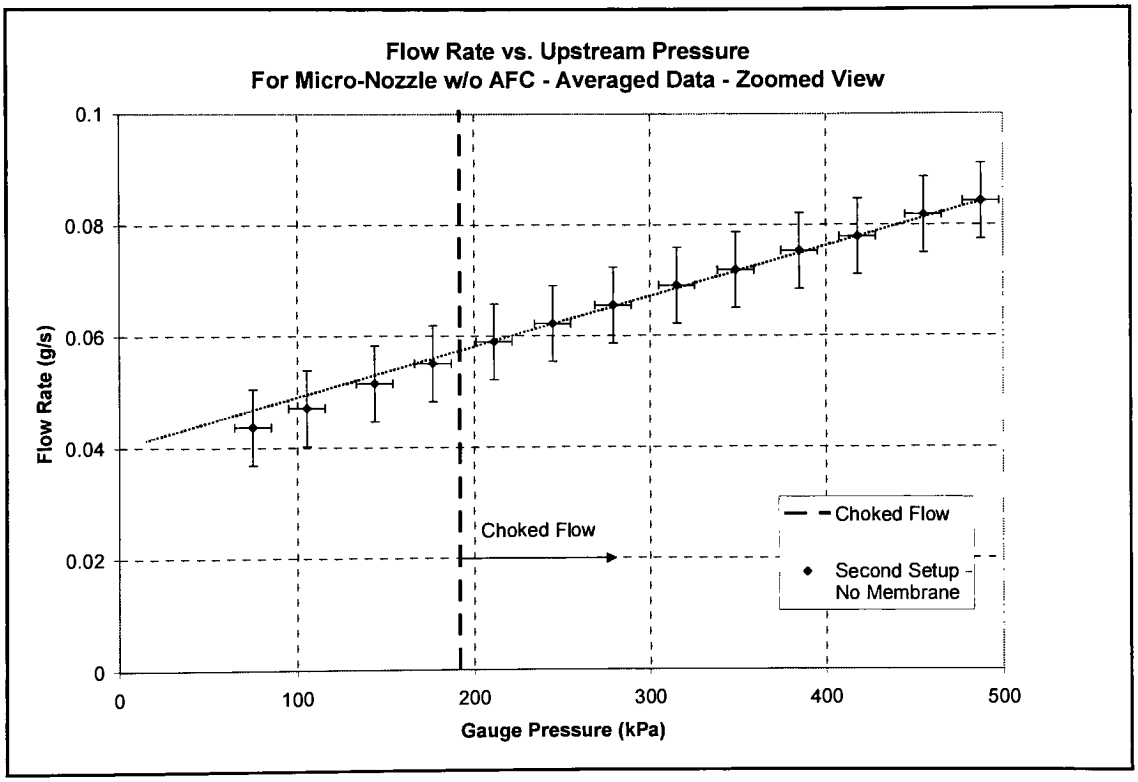

Figure 5.7 – Flow Rate vs. Upstream Pressure – No AFC – Zoomed Setup 2

This phenomenon is clearly occurring within the RIT nozzle, which supports the conclusion that the flow has reached sonic speeds at the nozzle throat. In Figure 5.7 a line is drawn through each of the data points following the choke point to demonstrate their linearity. From this line it is also evident that before the choke point the flow rate is exhibiting a non-linear

flow rate versus inlet pressure relationship. This same phenomenon occurs in the flow rate data for the first setup. A plot of this data is contained in the Appendix in Figure B.13.

Figure 5.8 shown below is a plot of the Coefficient of Discharge (C_d) of the RIT micro-nozzle as it varies with the nozzle inlet pressure. It is clear in both setups that the C_d is decreasing as the inlet pressure is increased, which is opposite to the findings of Bayt and others in experimental studies of micro-nozzles. These discrepancies may be attributed to the low aspect ratio of the RIT nozzle, which is not characteristic of the nozzles found in these other experimental studies. The highly three-dimensional flow behavior, as a result of the thin nozzle geometry, may be creating a blockage effect.

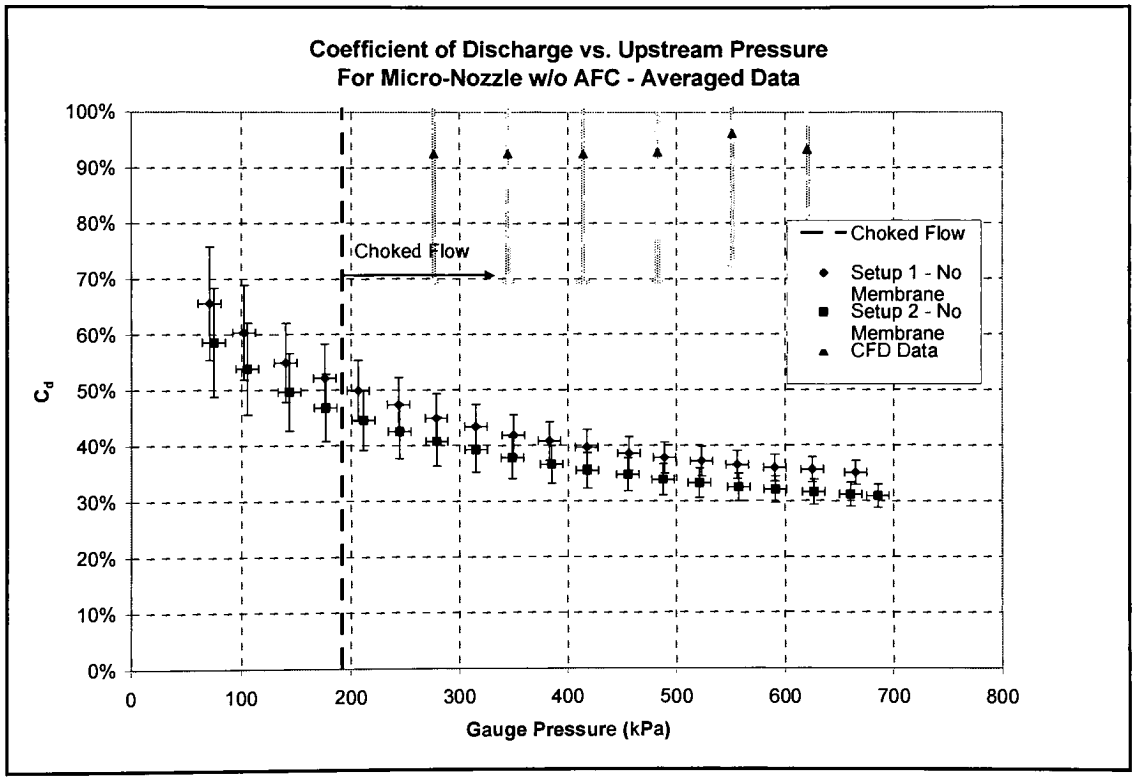

Figure 5.8 - C_d vs. Inlet Pressure

Another possible explanation is that significant flow separation is occurring upstream of the nozzle throat, in the nozzle plenum. Figure 5.9 shows the possible flow behavior at the nozzle inlet. Due to the small plenum size it is likely that the flow is separating before entering the nozzle inlet. This separation would increase as the pressure is increased, further degrading the nozzle performance as the experimental results illustrate. Unfortunately,

without flow visualization, no definitive conclusion can be drawn explaining this flow behavior.

The specific impulse of a nozzle varies proportionally with thrust and inversely with mass flow rate; therefore the trends in the specific impulse provide no original insight. A plot of the specific impulse versus inlet pressure is contained within the Appendix in Figure B.14.

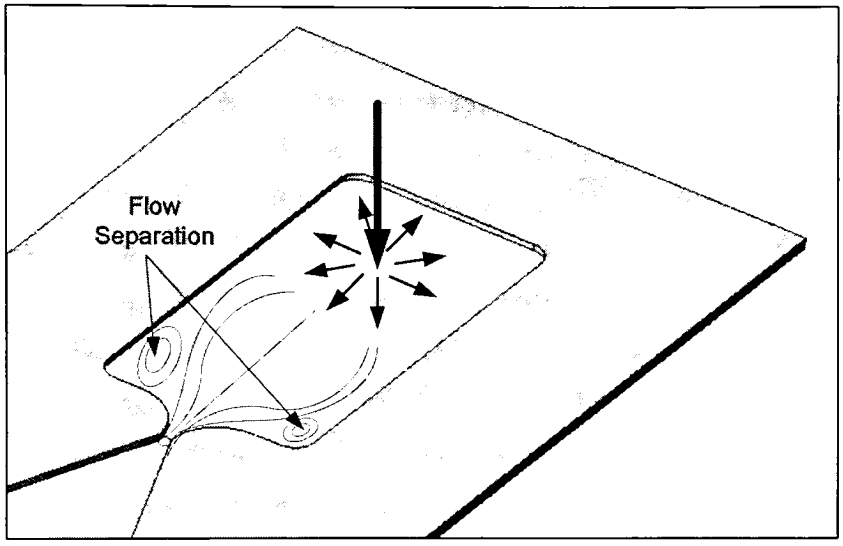

Figure 5.9 - Possible Flow Separation Occurring at Nozzle Inlet

The same degradation in nozzle performance with increased inlet pressure is evident in a plot of the throat displacement thickness versus the throat Reynolds number, shown in Figure 5.10. The displacement thickness is defined as the distance the upper or lower nozzle wall would have to displace in order to match the experimental flow-rate with the isentropic flow-rate. It allows for the quantification of the boundary layer thickness in the throat. The displacement thickness should decrease with increasing Reynolds number. Future testing with flow visualization is necessary to explain the driving force behind this flow behavior.

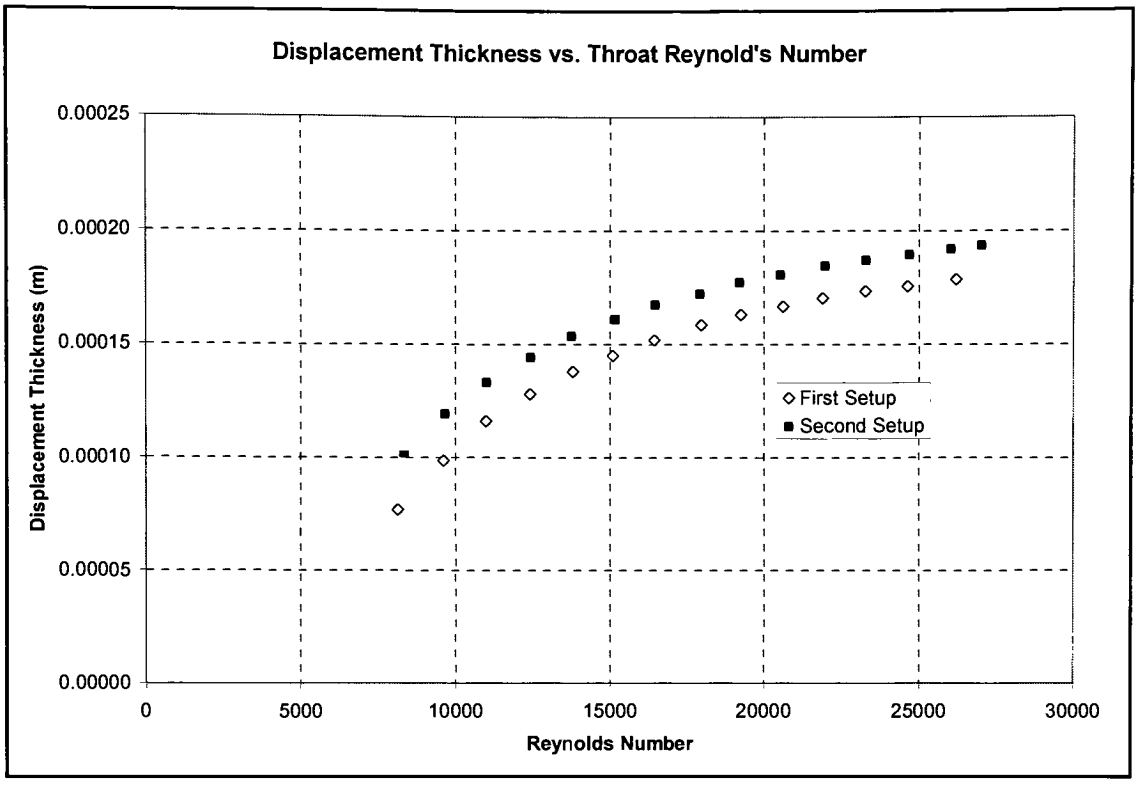

Figure 5.10 - Displacement Thickness vs. Reynolds Number - No AFC

The low C_d and low mass flow rate experimentally determined for the RIT nozzle suggest that the nozzle thrust is likely within the lower end of the measurement error. The CFD predicted nozzle efficiency is considerably better than the experimental efficiency. Since mass flow rate and thrust output are interrelated properties, relative to the experimental results, the high flow-rate predicted by the CFD model, would be coupled with a high thrust prediction. This is true if the experimental thrust is in the lower end of the measurement error.

5.2.2 With Active Flow Control

In Figure 5.11 the thrust is plotted against the inlet pressure for membrane pressures of 0 and 138 kPa (20 psi). Figure 5.11 represents averaged data from five experimental runs. The original data is shown within the Appendix in Figure B.15. The uncertainty in the thrust measurement for the nozzle without AFC is estimated to compensate for the uncertainty due to the pressurization of the tubing. In the two cases plotted in Figure 5.11 the tubing effect is

the same. Since the thrust difference between the two cases is of greatest concern, this tubing effect can be ignored in evaluating the effect of AFC. This being the case, the uncertainty in the thrust data can confidently be lowered to 0.5 mN. Under this modified uncertainty it can be stated with confidence that the membrane deflection has an effect on the nozzle's thrust output. Flow rate data was not taken for the nozzle with AFC, therefore the nozzle efficiency and specific impulse were not calculated.

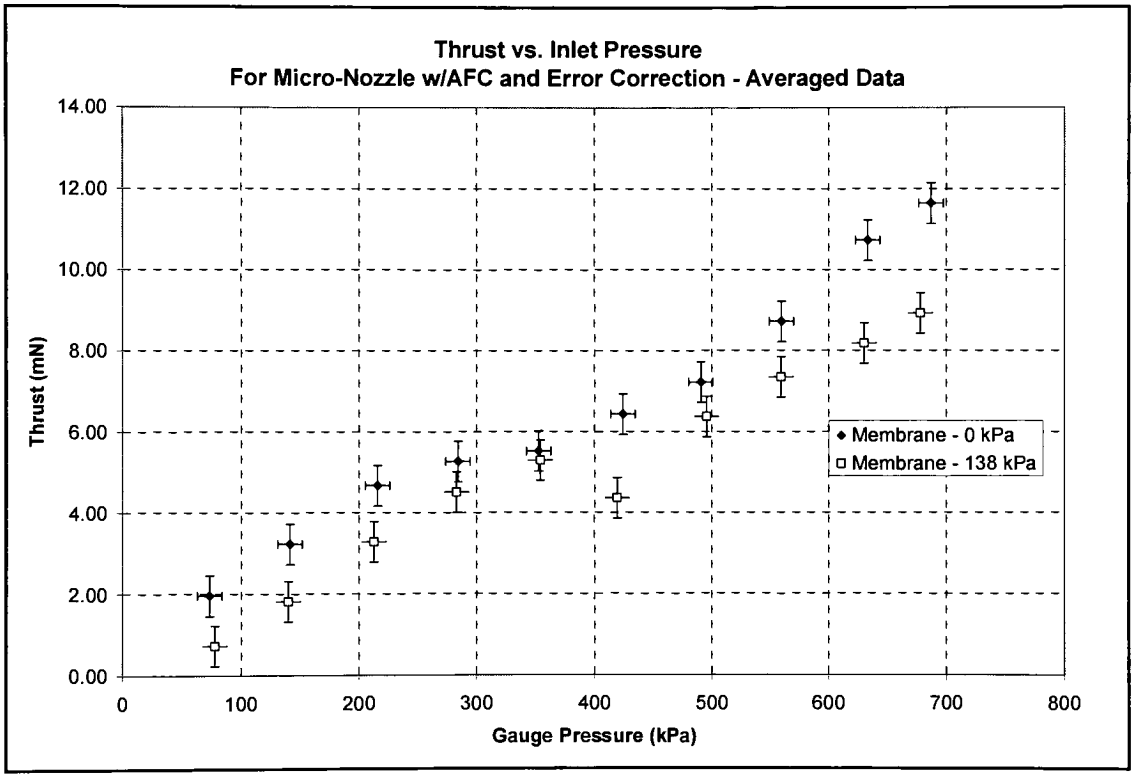

Figure 5.11 Thrust vs. Inlet Pressure w/AFC - Averaged Data - Modified Uncertainty

Fabrication issues do not permit repeatable test results due to reliability issues related to the silicone's adhesion to the upper aluminum boundary. Unfortunately, the membrane size varied from setup to setup and run to run as the silicone separated from the aluminum block. The fabrication process recommended in Section 6 would likely eliminate these issues.

With the introduction of the membrane to the high-speed flow distinct screeching sounds were produced by the device. Depending upon the inlet pressure applied, the sound

would vary. This is likely due to dynamic instability in the membrane. In the current study this instability along with membrane distortion was not addressed, but it certainly should be noted. It is likely that as the membrane deflected the surface became distorted due to the viscous effects of the impinging flow. This distortion was not modeled in this study. The distortion was most likely dynamic, possibly fluttering in the flow creating the sounds observed during testing.

The membrane shape also is affected by the local static pressure at the throat. Assuming an isentropic compression from the plenum to the nozzle throat, for a 689 kPa (100 psi) inlet pressure, the static pressure at the throat would be (364 kPa) 52.8 psi. Therefore in theory the membrane was actually being deflected away from the flow at all times. Simply the degree of this inward deflection was modified as the membrane was pressured. Whether or not this was actually occurring is unknown. It was observed that the membrane pressurization did indeed lower the nozzle thrust, but the method of control is unknown.

6 Conclusions and Recommendations

A micro-nozzle with flow control capabilities has been designed, modeled and tested. A three-dimensional viscous computational fluid dynamics (CFD) model of a supersonic micro-nozzle, with throat dimensions of 0.380 mm (0.015 in) x 4.7 mm (0.185 in) has been solved using FLUENT. This model was validated using available published experimental data by Choudhuri et al., which showed good agreement with the CFD results. The greatest percent difference in the thrust was 23%, but the trends in the data were similar. Also, the qualitative flow behavior predicted by the CFD model closely matches the published Schlieren photography flow visualizations provided in the same study.

Using CFD, a model of the RIT nozzle with active flow control (AFC) was constructed. The CFD analysis predicts a supersonic to subsonic transition in the nozzle exit caused by the combined effect of a weak normal shock and boundary layer build up. The dominant viscous effects are due to the low aspect ratio of the nozzle, which creates three dimensional losses in the nozzle flow.

Experimental mass flow-rate results for the RIT nozzle without AFC show that choked flow was achieved. The nozzle efficiency ranged from 66% to 31%. This low performance is partially due to the gasket compression from the clamping process during the device assembly. The gasket material is forced into the nozzle flow reducing the nozzle thickness. The nozzle efficiency or coefficient of discharge (C_d) was found to decrease as the inlet pressure was increased, contrary to other published micro-nozzle studies. This is likely due to three-dimensional viscous effects not encountered in the high aspect ratio nozzles of these other studies Also, separation occurring upstream of the nozzle throat, in the nozzle plenum, may be decreasing the effective throat width.

The CFD results for the RIT nozzle over-predict the nozzle thrust and efficiency. However, the CFD model does not account for gasket compression or flow separation. Considering these factors, it can be concluded that CFD can be used as a design tool in supersonic micro-nozzle research with separated flow. It should be noted; the nozzle flow must be considered continuum flow. Also, the CFD study completed was not exhaustive, but the results obtained support the conclusion that CFD can be used as a design tool of supersonic micro-nozzles of the size scale investigated here.

A supersonic micro-nozzle assembly with AFC was constructed and successfully operated. Thrust data was captured and flow control was demonstrated. By varying the membrane pressure, the nozzle thrust magnitude was controlled. However, the degree of the thrust magnitude control was not repeatable due to adhesion issues between the silicone and the aluminum block. This could be remedied by using Sylgard 184 silicone. This silicone could be spun onto a quartz or thick silicon wafer to the desired membrane thickness, and a hole could then be etched in the wafer to provide the pressure input. This process provides more flexibility in the actuator's performance by allowing for more precise control over the membrane thickness. As the membrane fabrication process becomes more refined it would be advantageous to test and model the membrane material using the theory described by Kempski (Kempski, 1988). This would permit a more accurate deflection model than the simplistic model utilized in the current study.

The process of actuation was provided by an external pressure source, which would be impractical in a spacecraft application. A thermopneumatic actuator provides a low weight, low energy method of actuation. A device of this nature is also easily fabricated. A simple resistive heater and sealed cavity is all that is required. If time response of the actuator is of significant concern, a smart metal diaphragm could be investigated, although fabrication is a momentous hurdle to overcome.

In the current study all experimentation occurred in standard atmospheric conditions. This prevented the nozzle from achieving supersonic flow at the nozzle exit. Experimentation in a near vacuum environment is necessary to quantify the actual performance of the AFC device without flow separation due to shock formation. Furthermore, flow visualization using Schlieren photography would be valuable to gain a better understand of the driving forces behind the nozzle performance with and without flow control. Using this tool it would be possible to achieve a qualitative understanding of the flow behavior as the silicone membrane enters the nozzle flow. Furthermore, visualization of the membrane deflection would provide an understanding of the effects of the pressure distribution and the possible dynamic instability in the membrane. A real understanding of the membrane behavior in the harsh environment of a high-pressure high-speed flow is crucial to the reliable operation of a flow control device of this type.

Thrust measurement of low thrust devices such as micro-nozzles is not a trivial task. Measurement resolution and accuracy is difficult to obtain when the thrust output remains on the order of 40-50 mN. It would be advantageous to design and build a low force thrust stand, which would isolate the nozzle thrust from inlet connection effects. This would allow for the acquisition of more valuable nozzle performance data. Also, as further miniaturization occurs, a thrust stand of the type becomes necessary.

Attention must be paid to the fabrication of the micro-nozzle. Surface finish has been shown to affect performance; therefore the fabrication of the device through semiconductor processing techniques remains advantageous. This is true for several reasons. This method of fabrication permits further miniaturization of the device. Also, as the device reduces in size, several nozzle designs can be fabricated from a single wafer, bringing down the cost per device.

While surface finish is mentioned as an important factor in nozzle fabrication, the degree to which the nozzle wall surface finish affects nozzle performance is not known. It would be advantageous to quantify the effect of the wall finish in order to obtain a better understanding of the limitations of fabrication options. Furthermore, Choudhuri et al. proposed that the assumption of symmetric flow in micro-nozzles may be incorrect due to the effects of small unavoidable imperfects at the nozzle wall. This hypothesis could be scrutinized by an investigation into the affect of surface finish on nozzle performance.

The results and concepts established in the current study should serve to be a good spring board to future work at RIT in the area of micro-nozzle research.

A. Appendix – Isentropic Model Equations

'On-Design' Isentropic Model

The following properties are set as constants: γ, T_o, A_e, P_o, P_e, ρ_o, C_p, R

The exit Mach number drives the analysis; the throat area is then calculated assuming isentropic expansion:

$$A_t = \frac{A_e}{\sqrt{\frac{1}{M^2}\left[\frac{2}{\gamma+1}\left(1+\frac{\gamma-1}{2}M^2\right)\right]^{(\gamma+1)/(\gamma-1)}}}$$

Equation A-1 - Isentropic Throat Area Calculation

Once the throat area is known, the mass flow rate is calculated:

$$\dot{m} = \frac{P_o A_t}{\sqrt{RT_o}}\sqrt{\frac{\gamma}{\left[1+\frac{\gamma-1}{2}\right]^{(\gamma+1)/(\gamma-1)}}}$$

Equation A-2 - Isentropic Mass Flow Rate at Nozzle Throat

From this information the thrust and specific impulse are calculated:

$$\tau = \dot{m}\left[M_e\sqrt{\gamma R\left[\frac{T_o}{\left[1+\frac{\gamma-1}{2}M_e^2\right]}\right]}\right]$$

Equation A-3 - Isentropic Thrust Calculation

$$I_{sp} = \frac{\tau}{\dot{m}(9.81)}$$ Assuming Acceleration of Gravity is 9.81 m/s^2

Equation A-4 - Isentropic Specific Impulse Calculation

'Off-Design' Isentropic Model

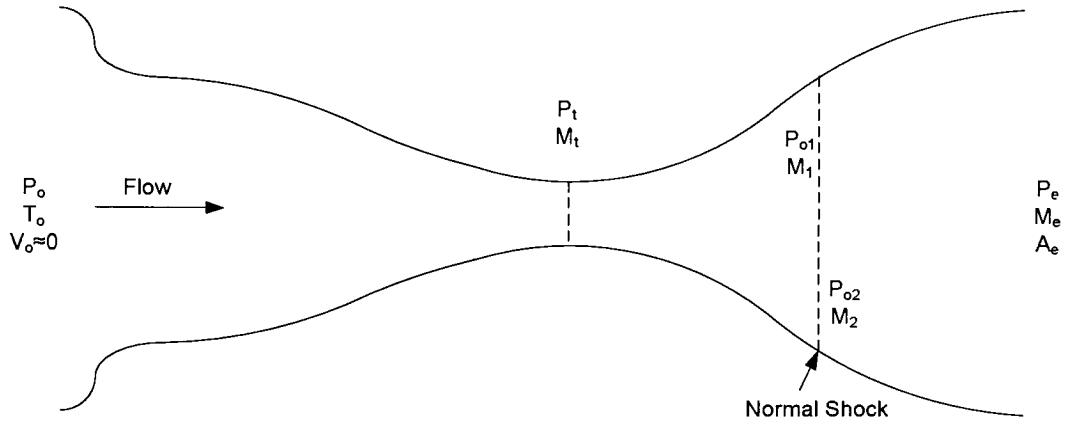

Figure A.1 - 'Off – Design' Problem Schematic

The following properties are set as constants: γ, T_o, A_e, P_o, P_e, ρ_o, C_p, R,μ

The inlet pressure or nozzle throat area is varied. Using the available information the exit Mach number is calculated.

$$M_e = \left[\left(\frac{-1}{\gamma - 1} \right) + \sqrt{ \left(\frac{1}{(\gamma-1)^2} + \left(\frac{2}{\gamma - 1} \right) \left(\frac{2}{\gamma + 1} \right)^{(\gamma+1)/(\gamma-1)} \left[\left(\frac{P_{o1}}{P_e} \right) \left(\frac{A_t}{A_e} \right) \right]^2 \right) } \right]^{1/2}$$

Equation A-5 - Exit Mach Number For Separation Conditions

Then,

$$\frac{P_{02}}{P_e} = \left[1 + \frac{\gamma - 1}{2} M_e^2 \right]^{\gamma/\gamma-1}$$

Equation A-6 - Total to Static Pressure Isentropic Relationship

The next step is to determine shock location, therefore M_1 must be found.

$\frac{P_{o2}}{P_{o1}} = e^{-(s_2 - s_1)/R}$ Where,

$$s_2 - s_1 = C_p \ln\left\{\left[1 + \frac{2\gamma}{\gamma+1}\left(M_1^2 - 1\right)\right]\left[\frac{2 + (\gamma-1)M_1^2}{(\gamma+1)M_1^2}\right]\right\} - R\ln\left[1 + \frac{2\gamma}{\gamma+1}\left(M_1^2 - 1\right)\right]$$

Equation A-7 - Calculation of Pressure Drop Across a Normal Shock

Using a solver macro in Microsoft Excel, M_1 was found. The nozzle area at the shock was found using a slightly modified version of Equation A-1. The nozzle geometry is known, therefore, the shock location was easily found knowing the nozzle area at the shock.

The mass flow rate, thrust, and specific impulse were each found using Equation A-2, Equation A-3, and Equation A-4.

B. Appendix – Additional Figures

B.1 CFD

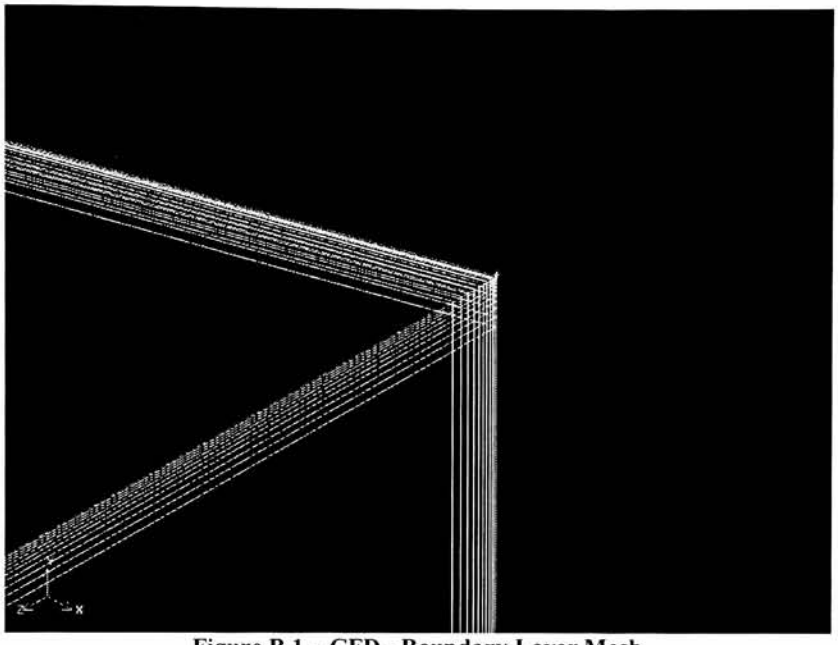

Figure B.1 – CFD - Boundary Layer Mesh

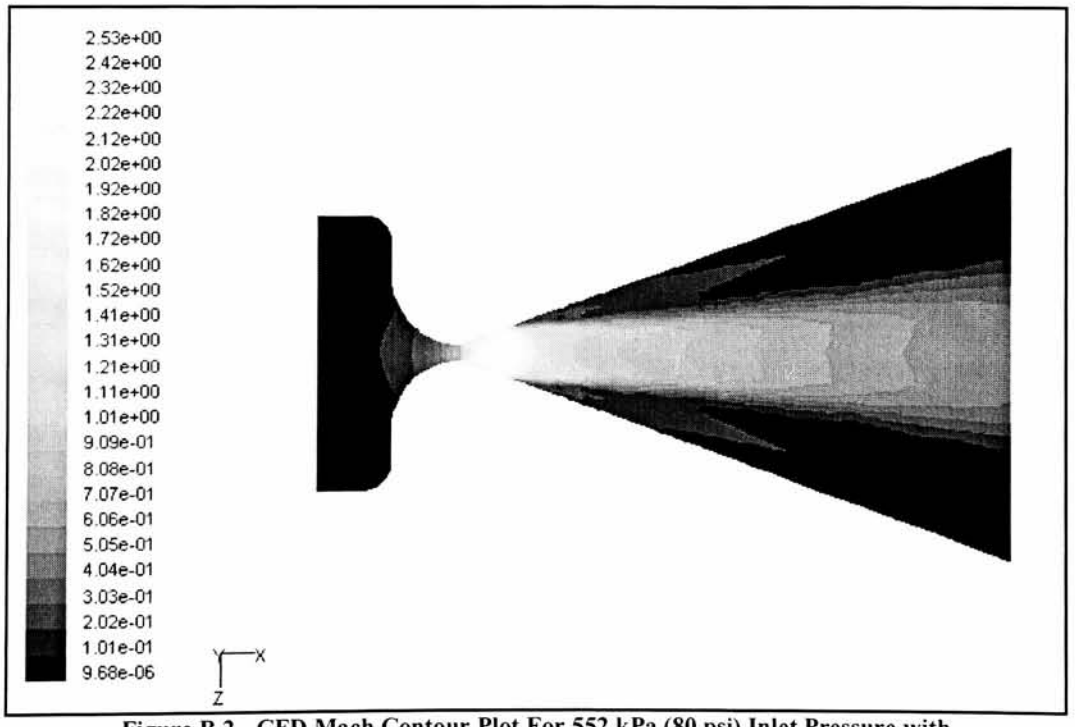

Figure B.2 - CFD Mach Contour Plot For 552 kPa (80 psi) Inlet Pressure with Membrane Pressure of 207 kPa (30 psi)

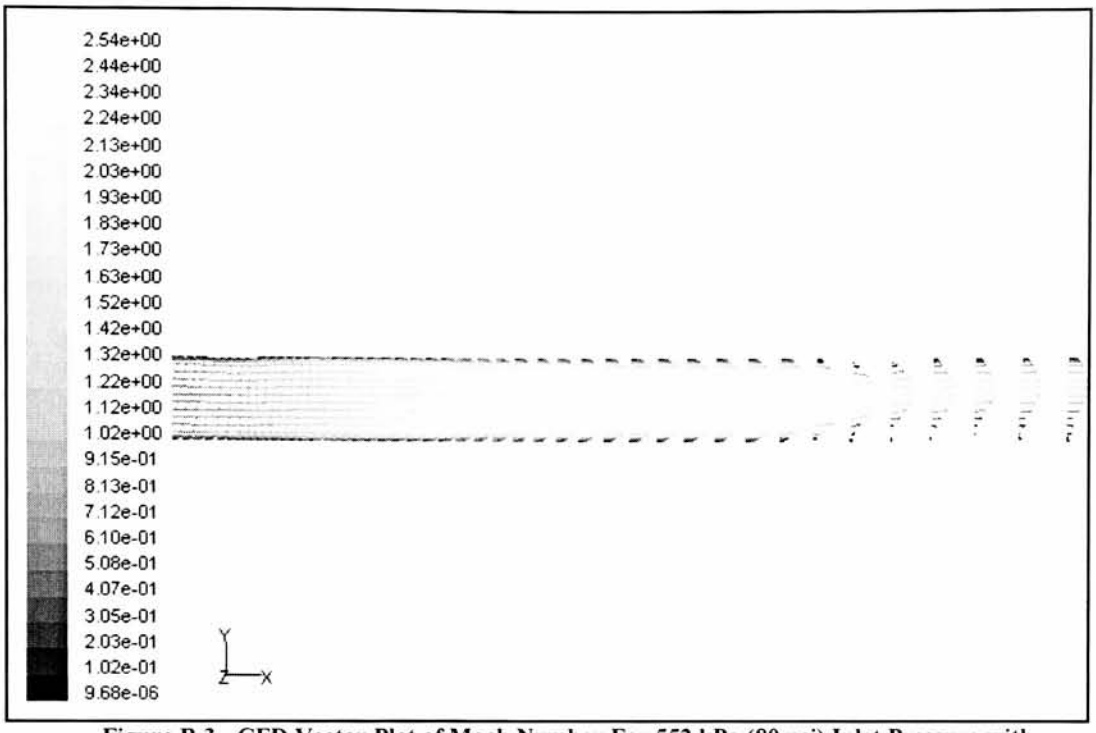

Figure B.3 - CFD Vector Plot of Mach Number For 552 kPa (80 psi) Inlet Pressure with Membrane Pressure of 207 kPa (30 psi)

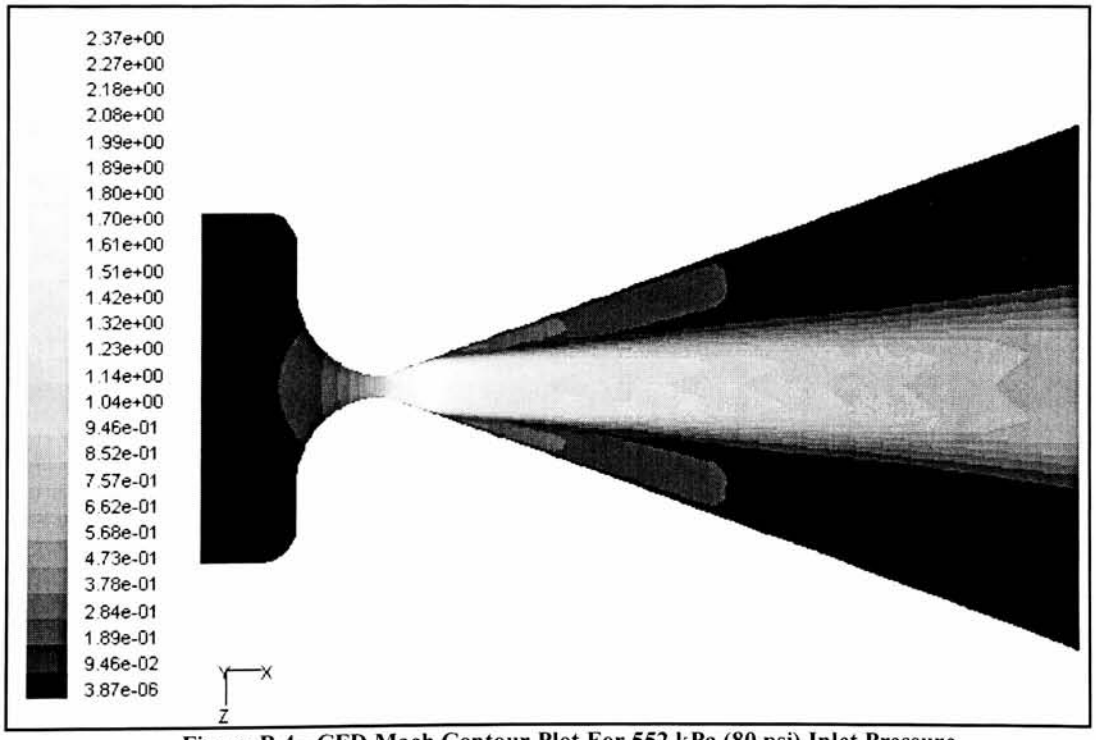

Figure B.4 - CFD Mach Contour Plot For 552 kPa (80 psi) Inlet Pressure With Membrane Pressure of 414 kPa (60 psi)

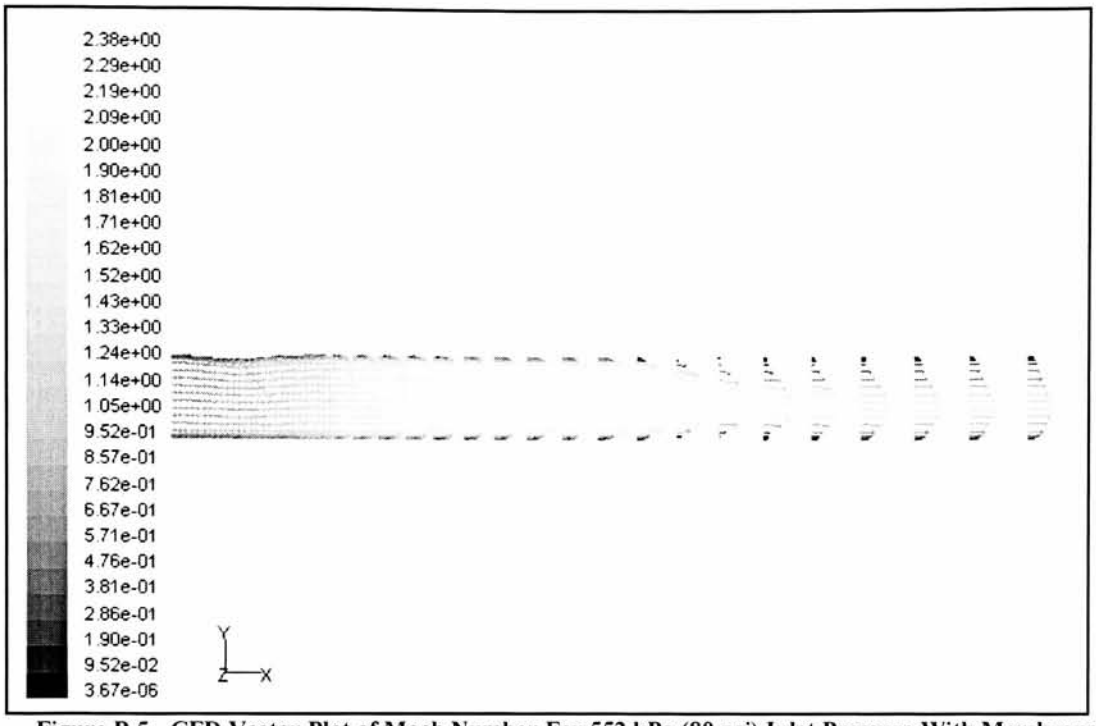

Figure B.5 - CFD Vector Plot of Mach Number For 552 kPa (80 psi) Inlet Pressure With Membrane Pressure of 414 kPa (60 psi)

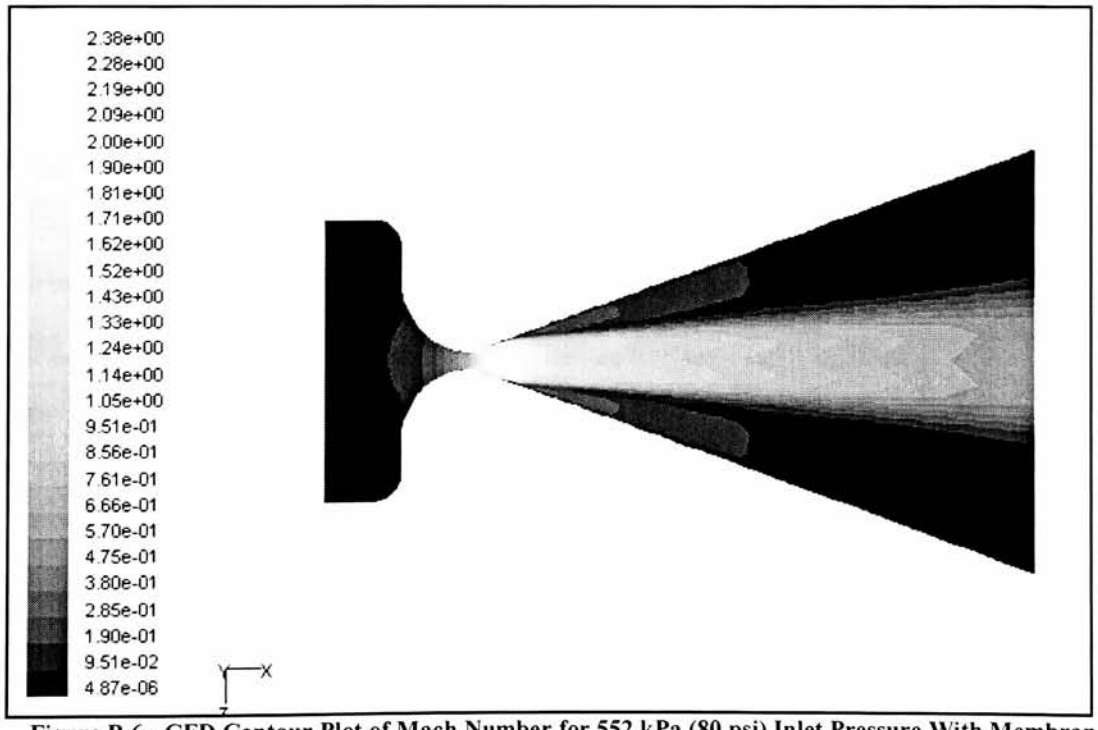

Figure B.6 - CFD Contour Plot of Mach Number for 552 kPa (80 psi) Inlet Pressure With Membrane Pressure of 621 kPa (90 psi)

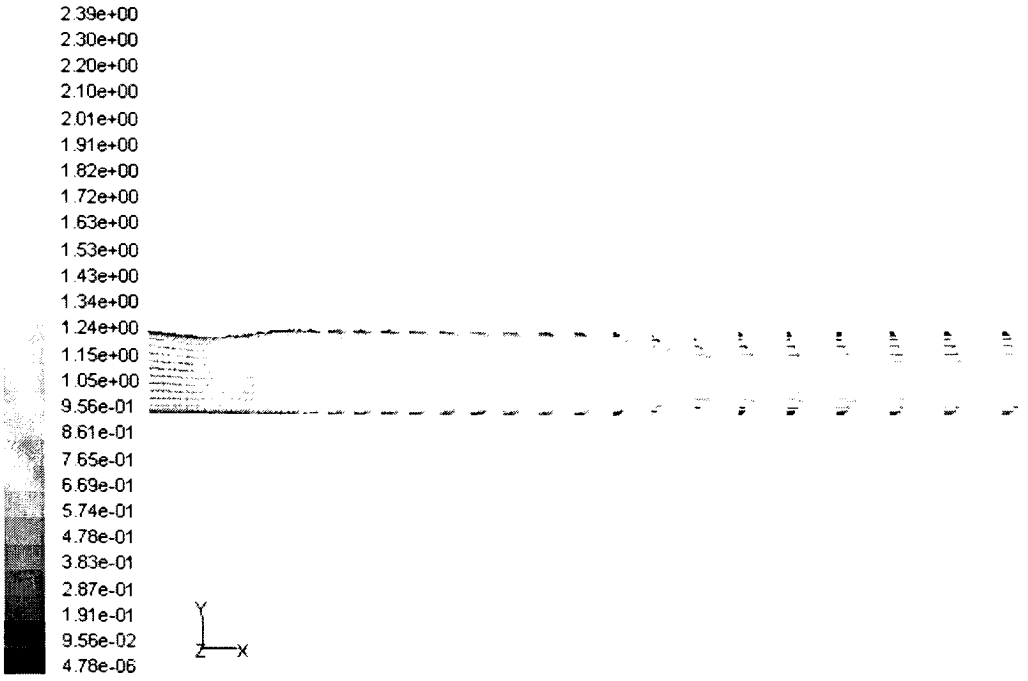

Figure B.7 - CFD Vector Plot of Mach Number for 552 kPa (80 psi) Inlet Pressure With Membrane Pressure of 621 kPa (90 psi)

B.2 Experimental Results

Run 1				Run 2		
Mass Before (g)	Mass After Assembly (g)	Percent Difference		Mass Before (g)	Mass After Assembly (g)	Percent Difference
0.75	0.75	0.00%		0.75	0.75	0.00%
1.17	1.17	0.00%		1.17	1.18	-0.85%
6.12	6.12	0.00%		6.12	6.13	-0.16%
6.16	6.18	-0.32%		6.16	6.17	-0.16%
0.43	0.44	-2.33%		0.43	0.44	-2.33%
1.46	1.47	-0.68%		1.46	1.45	0.69%
2.72	2.73	-0.37%		2.72	2.72	0.00%
0.46	0.47	-2.17%		0.46	0.46	0.00%
0.70	0.72	-2.86%		0.70	0.71	-1.43%
0.13	0.14	-7.69%		0.13	0.13	0.00%

Figure B.8 - Tubing Effect Test Results

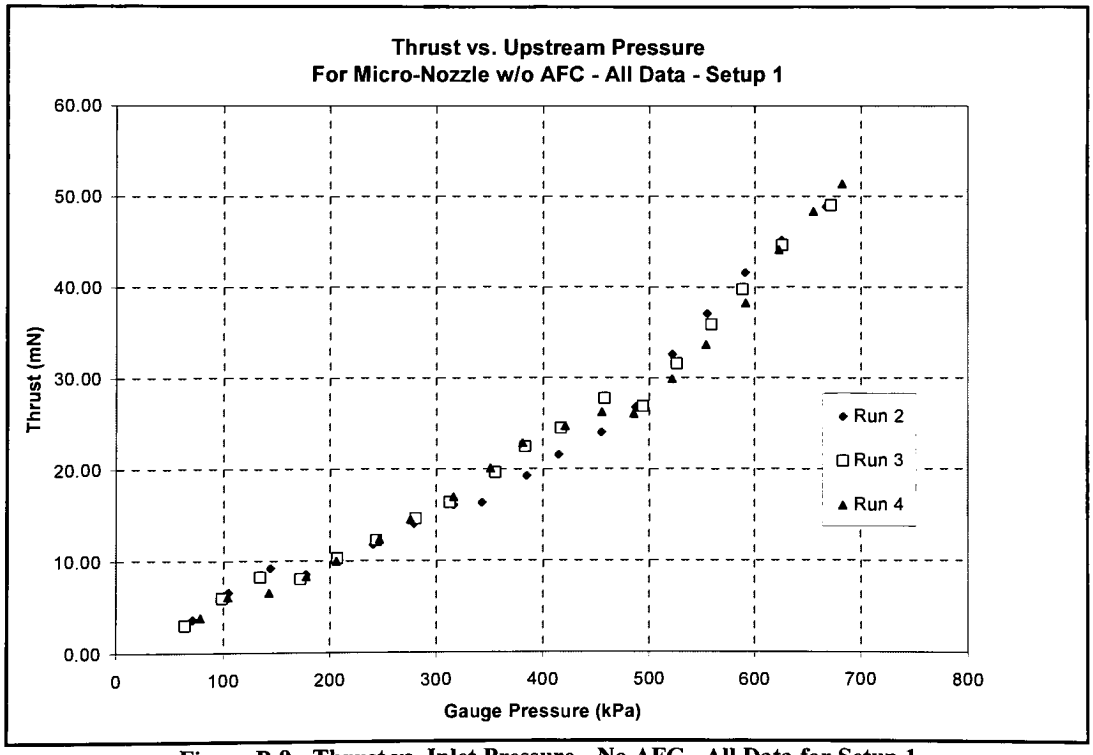

Figure B.9 - Thrust vs. Inlet Pressure - No AFC - All Data for Setup 1

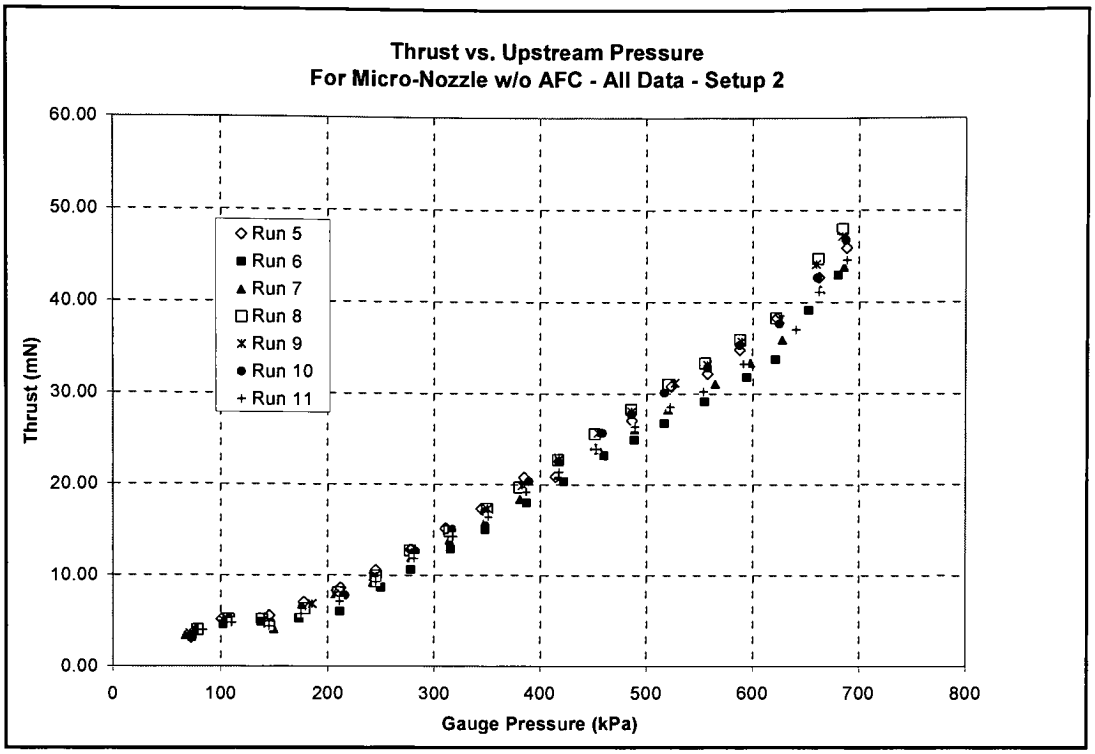

Figure B.10 - Thrust vs. Inlet Pressure - No AFC - All Data for Setup 2

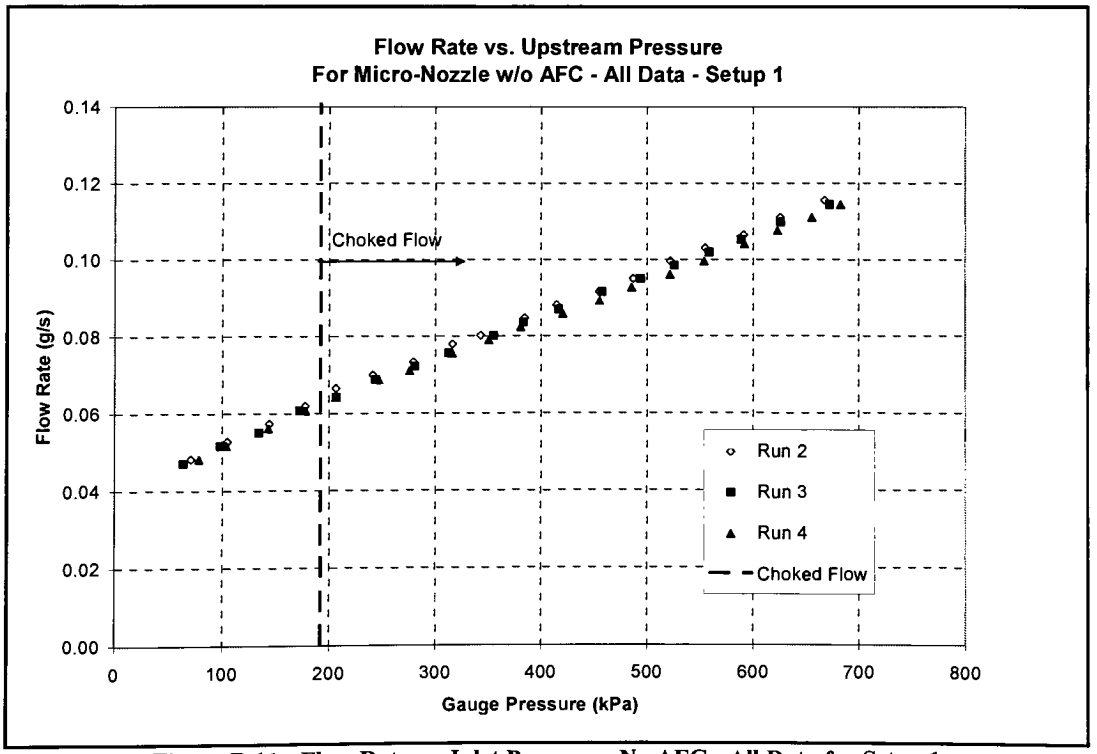

Figure B.11 - Flow Rate vs. Inlet Pressure - No AFC - All Data for Setup 1

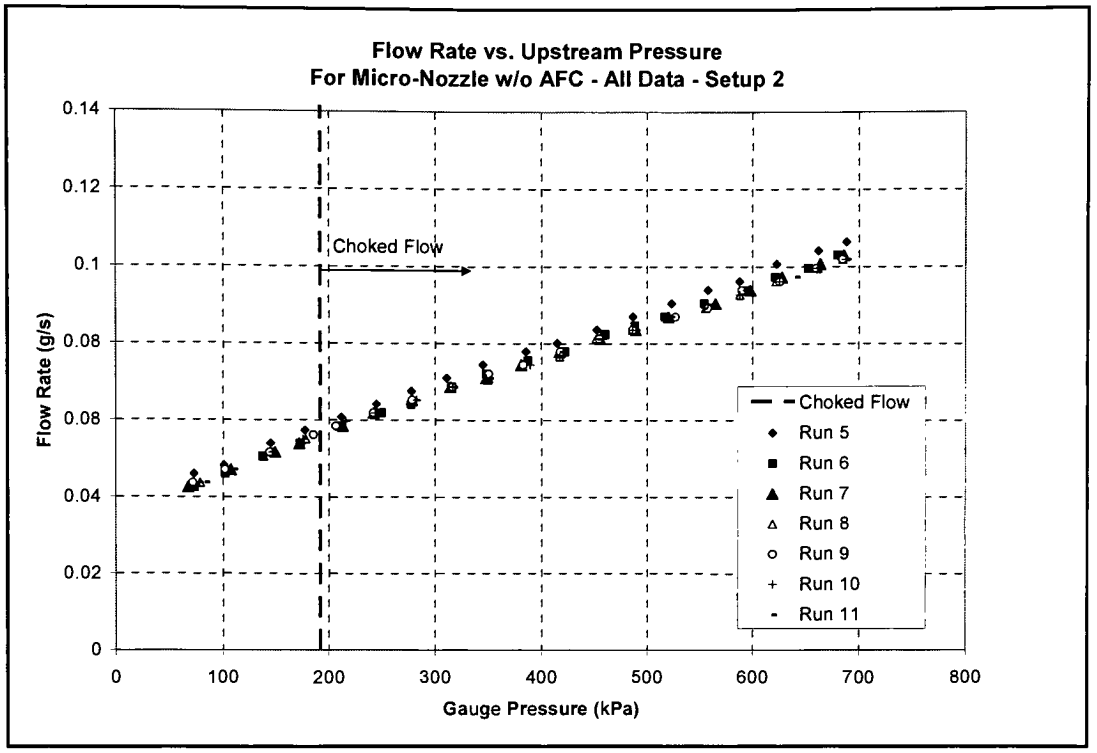

Figure B.12 - Flow Rate vs. Inlet Pressure - No AFC - All Data for Setup 2

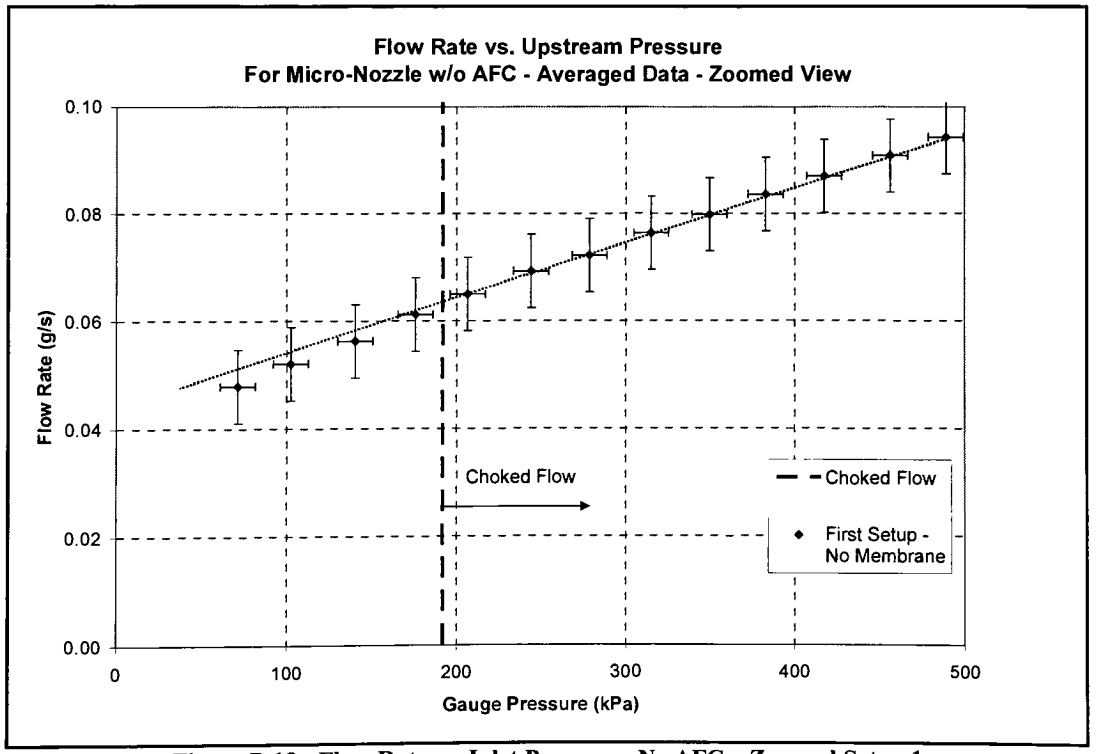

Figure B.13 - Flow Rate vs. Inlet Pressure - No AFC – Zoomed Setup 1

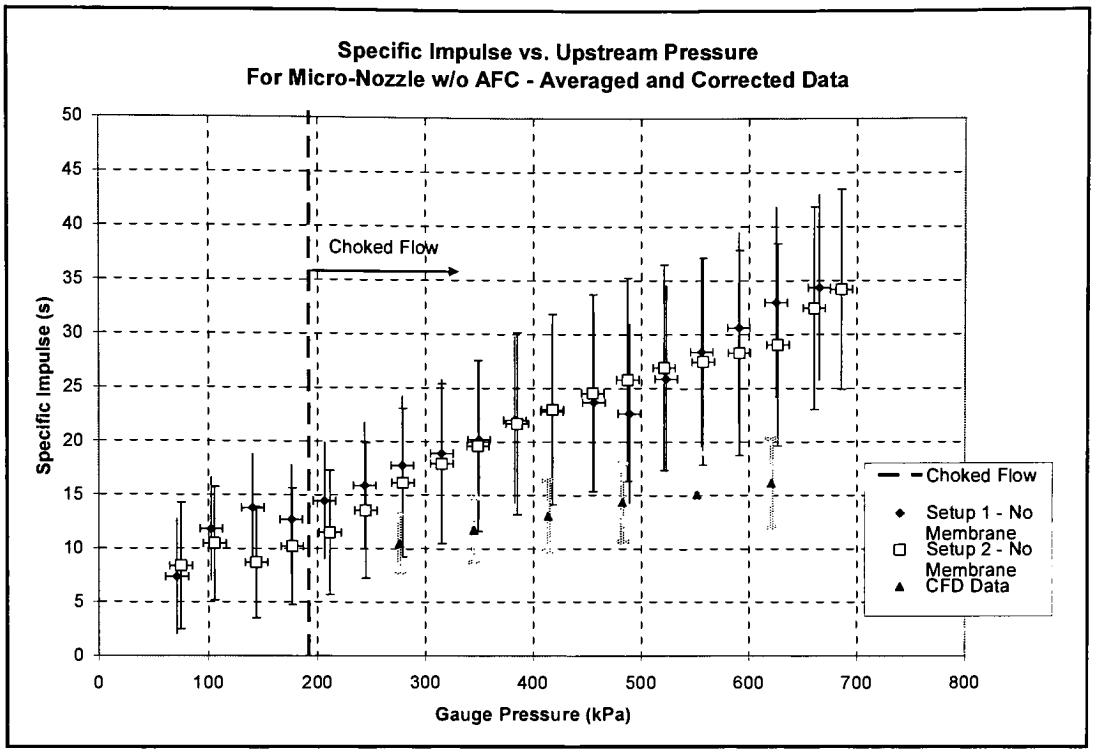

Figure B.14 - Specific Impulse vs. Inlet Pressure - Corrected Data - No AFC

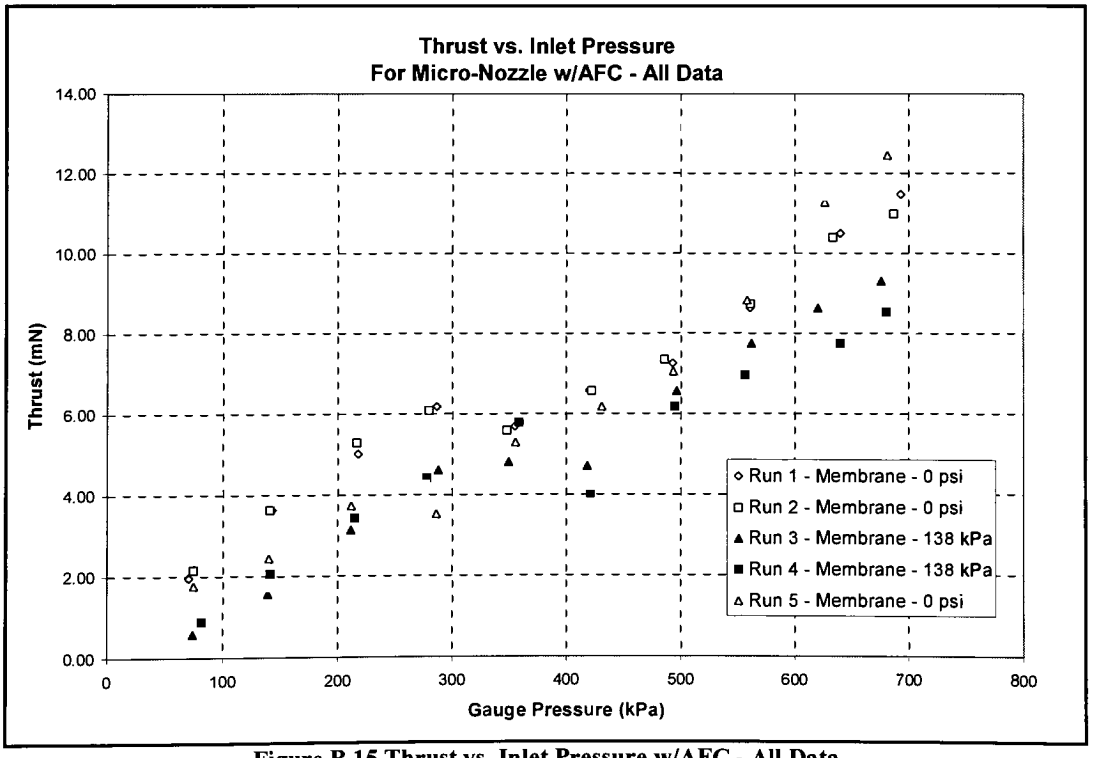

Figure B.15 Thrust vs. Inlet Pressure w/AFC - All Data

C. Appendix – CAD Detail Drawings

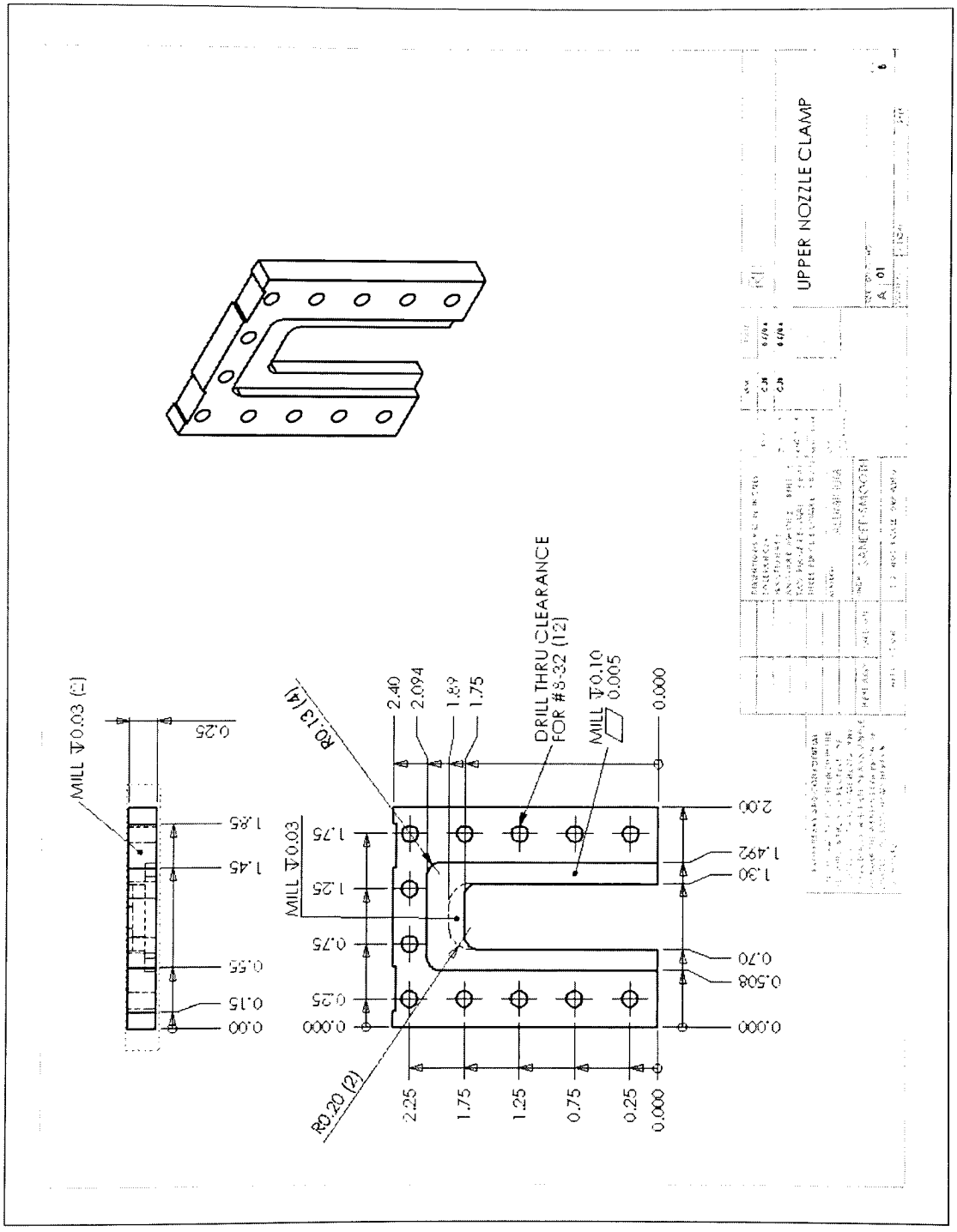

Figure C.1 - Upper Nozzle Clamp Detail Drawing

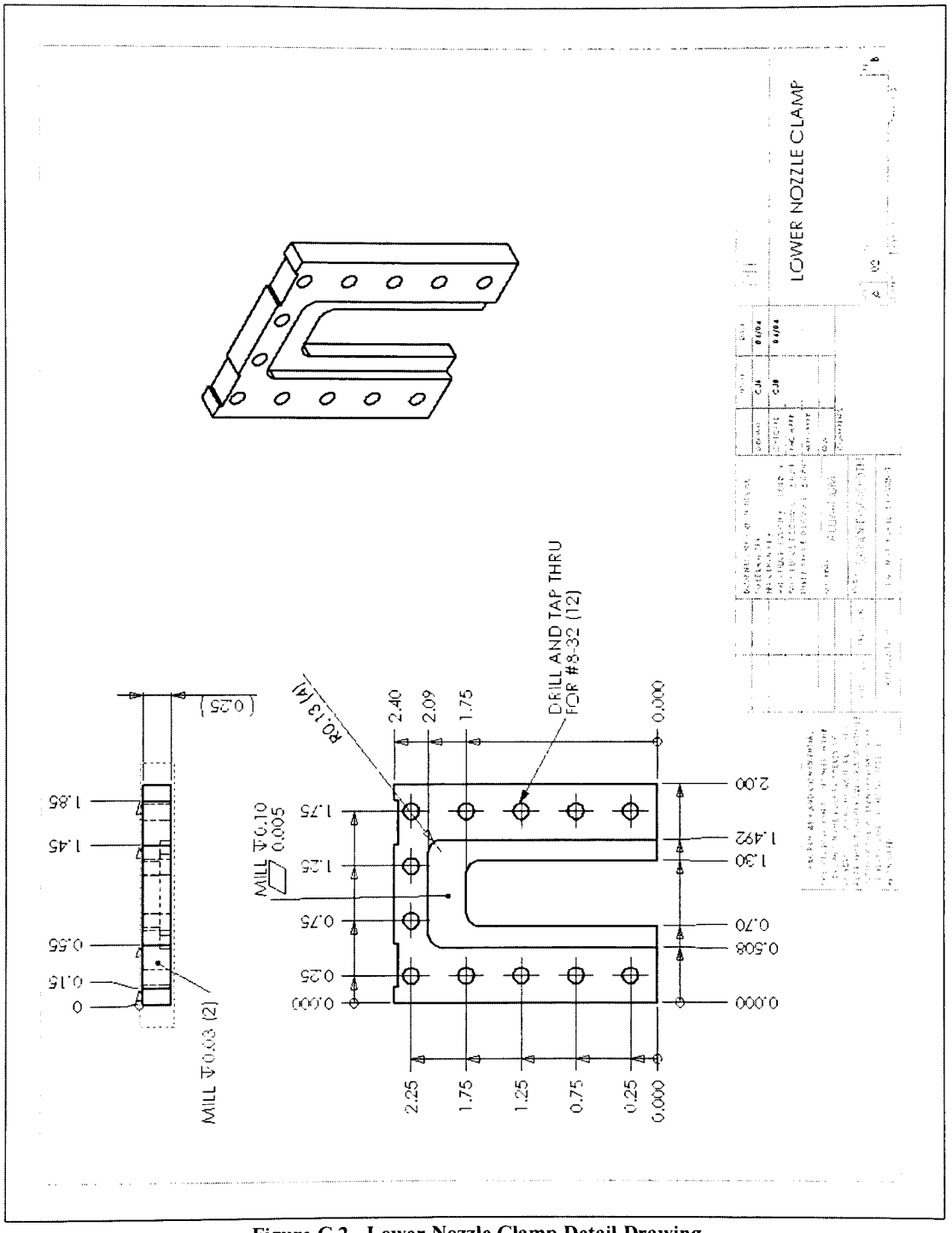

Figure C.2 - Lower Nozzle Clamp Detail Drawing

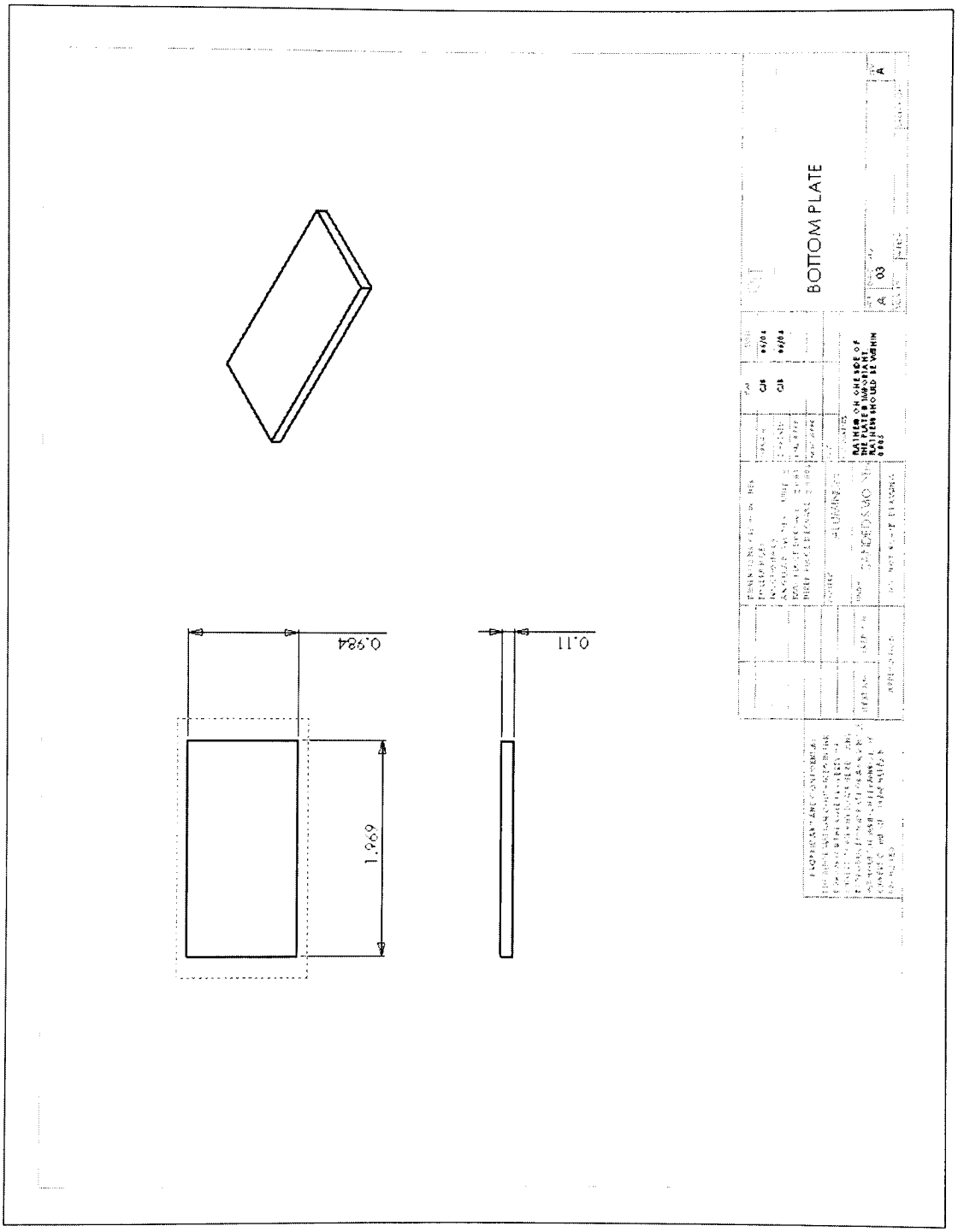

Figure C.3 - Bottom Plate Detail Drawing

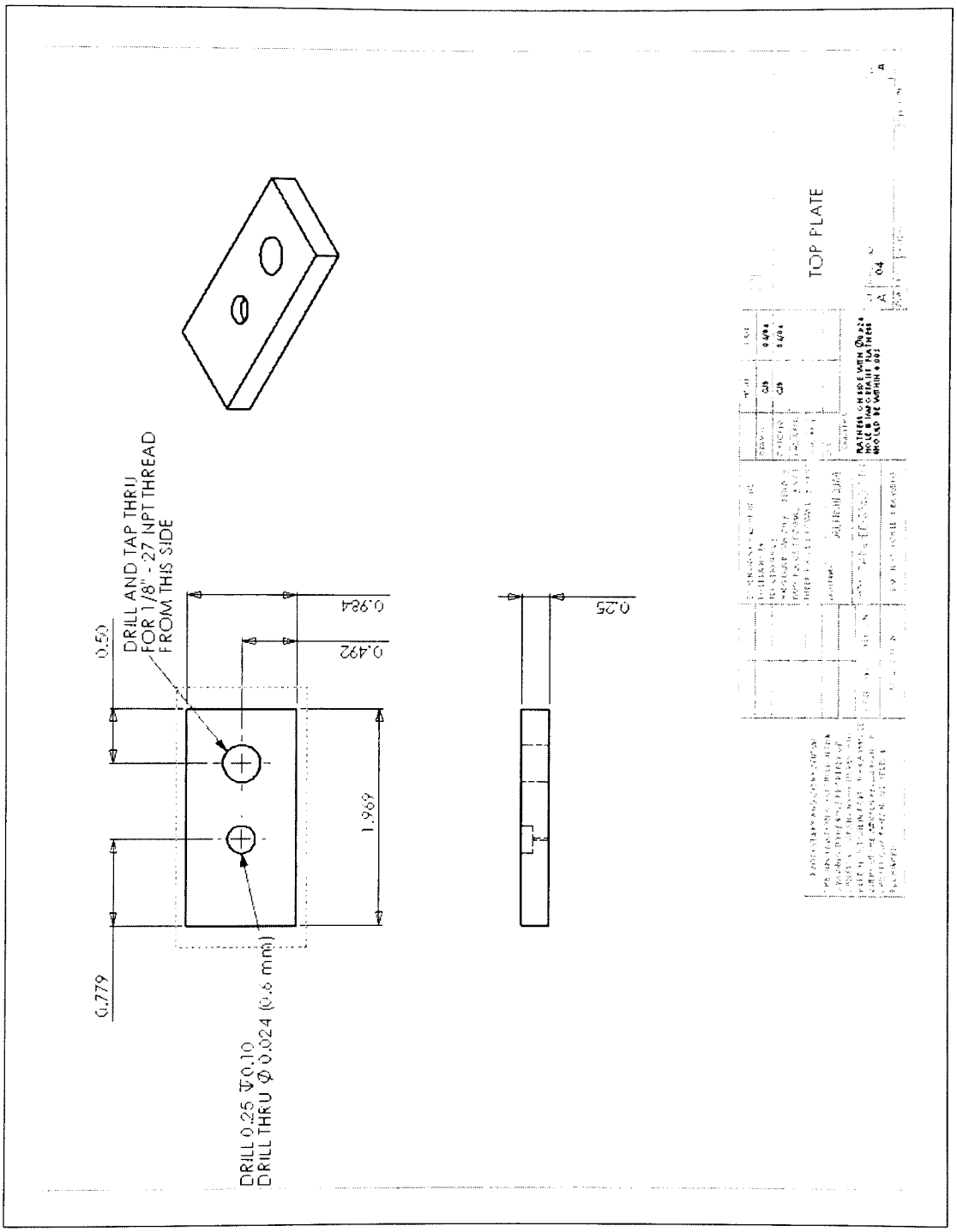

Figure C.4 - Top Plate Detail Drawing

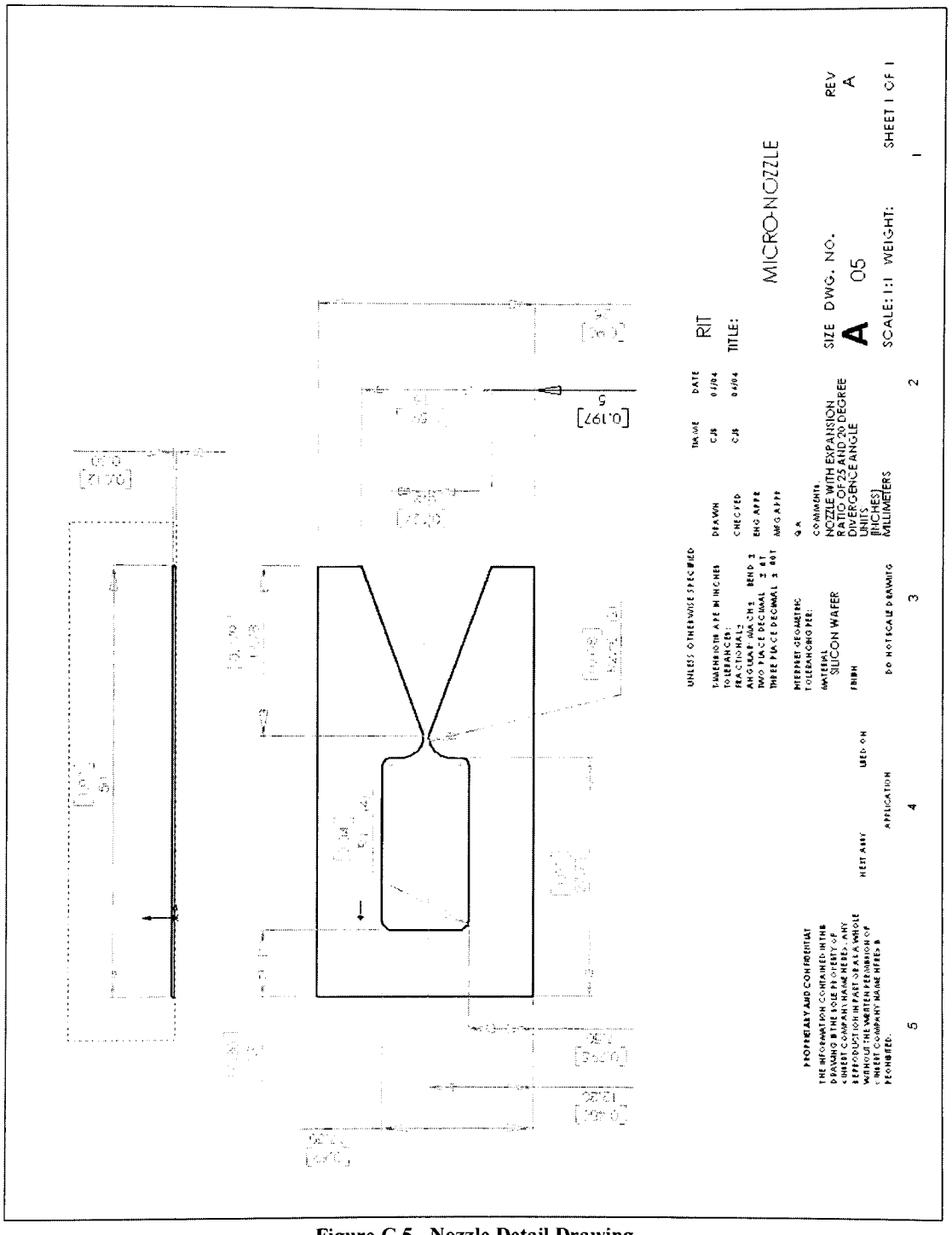

Figure C.5 - Nozzle Detail Drawing

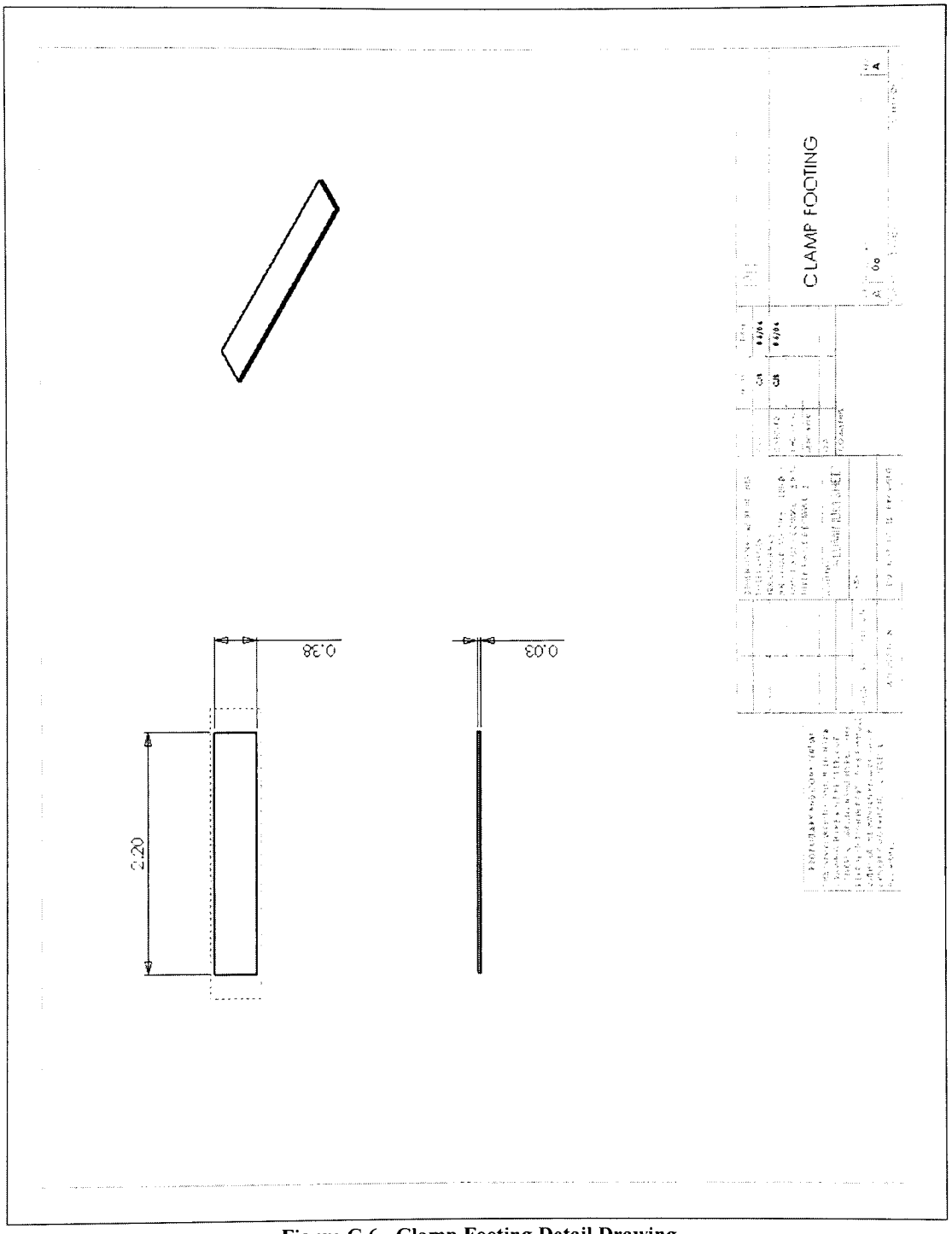

Figure C.6 - Clamp Footing Detail Drawing

D. Appendix – Uncertainty Analysis

The values used for the experimental equipment uncertainties are shown in Table 5.2. The following analysis was used in the calculation of the uncertainty propagation in calculations (Fox & McDonald, 1998). The relative uncertainty was used in the error propagation calculations. The relative uncertainty of a measured quantity X is defined as:

$$u_X = \frac{\Delta X}{X}$$

Equation D-1 - Definition of Relative Uncertainty

The uncertainty propagation was calculated for the theoretical flow rate, coefficient of discharge (C_d), and specific impulse. The uncertainty propagation in the theoretical mass flow rate was derived by:

$$\dot{m}_{Theo} = \frac{(P_o + P_{atm})A_t}{\sqrt{RT_o}} \sqrt{\frac{\gamma}{\left[1+\frac{\gamma-1}{2}\right]^{\gamma+1/\gamma-1}}}$$

$$\dot{m}_{Theo} = f(P_o, T_o, P_{atm})$$

All other quantities are assumed constants.

$$d\dot{m}_{Theo} = \frac{\partial \dot{m}_{Theo}}{\partial P_o}\delta P_o + \frac{\partial \dot{m}_{Theo}}{\partial T_o}\delta T_o + \frac{\partial \dot{m}_{Theo}}{\partial P_{atm}}\delta P_{atm}$$

$$\frac{\partial \dot{m}_{Theo}}{\partial P_{atm}} = \frac{A_t}{\sqrt{RT_o}} \sqrt{\frac{\gamma}{\left[1+\frac{\gamma-1}{2}\right]^{\gamma+1/\gamma-1}}}$$

$$u_{\dot{m}_{Theo}, P_o} = \frac{P_o}{\dot{m}_{Theo}} \frac{\partial \dot{m}_{Theo}}{\partial P_o} u_{P_o} = \frac{P_o}{P_o + P_{atm}} u_{P_o}$$

Equation D-2- Uncertainty Propagation Calculation Process

The same procedure was used for P_{atm} and T_o, the uncertainty of the mass flow rate due to each of these is shown in Equation D-3.

$$u_{\dot{m}_{Theo},P_{atm}} = \frac{P_{atm}}{P_o + P_{atm}} u_{P_{atm}}$$

$$u_{\dot{m}_{Theo},T_o} = -\frac{1}{2} u_{T_o}$$

Equation D-3 - Relative Uncertainty of the Theoretical Mass-Flow Due to Uncertainty in P_{atm} and T_o

The overall relative uncertainty of the theoretical mass flow is shown in Equation D-4.

$$u_{\dot{m}_{Theo}} = \left[\left[\frac{P_o u_{P_o}}{P_o + P_{atm}} \right]^2 + \left[\frac{P_{atm} u_{P_{atm}}}{P_o + P_{atm}} \right]^2 + \left[-\frac{1}{2} u_{T_o} \right]^2 \right]^{1/2}$$

Equation D-4 - Overall Relative Uncertainty of Theoretical Mass-Flow Rate

The uncertainty used for the C_d and specific impulse was found using the same process. The equations used to calculate the error in these two properties is shown in Equation D-5 and Equation D-6 respectively.

$$u_{COD} = \left[\left(u_{\dot{m}_{act}} \right)^2 + \left(u_{\dot{m}_{Theo}} \right)^2 \right]^{1/2}$$

Equation D-5 - Overall Relative Uncertainty of Coefficient of Discharge (C_d)

$$u_{I_{sp}} = \left[(u_\tau)^2 + \left(u_{\dot{m}_{act}} \right)^2 \right]^{1/2}$$

Equation D-6 - Overall Relative Uncertainty of Specific Impulse

E. Appendix – Original Data

E.1 Without AFC

Run 1 5/28/2004

Flow Rate (mm)	Flow Rate (sL/min)	Upstream Temp (°C)	Static Pressure (psi)	Static Pressure Act (psi)	Thrust (g)
22.0	2.59	22.24	10	10.00	0.54
25.0	2.92	22.24	15	14.90	0.82
27.0	3.15	22.24	20	20.20	1.09
30.0	3.48	22.26	25	25.20	1.15
32.0	3.70	22.26	30	30.00	1.15
35.0	4.04	22.28	35	35.38	1.32
37.0	4.26	22.28	40	40.08	1.53
40.0	4.60	22.30	45	45.68	1.88
42.5	4.88	22.31	50	50.72	2.26
45.5	5.21	22.31	55	55.11	2.64
48.0	5.49	22.34	60	60.50	3.15
52.0	5.94	22.36	65	65.36	3.65
55.0	6.28	22.37	70	70.48	4.16
60.0	6.84	22.38	75	76.16	4.77
63.0	7.17	22.38	80	80.22	5.18
67.5	7.67	22.40	85	85.25	5.77
73.0	8.29	22.40	90	90.24	6.40
81.0	9.18	22.40	95	96.04	7.20
87.0	9.85	22.40	100	99.74	7.85

Run 2 5/28/2004

Flow Rate (mm)	Flow Rate (sL/min)	Upstream Temp (°C)	Static Pressure (psi)	Static Pressure Act (psi)	Thrust (g)
20.0	2.36	22.34	10	10.32	0.37
22.0	2.59	22.36	15	15.2	0.67
24.0	2.81	22.38	20	20.87	0.94
26.0	3.03	22.4	25	25.75	0.87
28.0	3.26	22.43	30	29.98	1.04
29.5	3.43	22.44	35	34.95	1.20
31.0	3.59	22.44	40	40.5	1.43
33.0	3.82	22.46	45	45.89	1.64
34.0	3.93	22.47	50	49.76	1.66
36.0	4.15	22.48	55	55.79	1.96
37.5	4.32	22.49	60	60.17	2.20
39.0	4.49	22.5	65	66.01	2.45
40.5	4.66	22.51	70	70.66	2.73
42.5	4.88	22.51	75	75.7	3.32
44.0	5.05	22.51	80	80.49	3.78
45.5	5.21	22.53	85	85.74	4.24
47.5	5.44	22.53	90	90.76	4.60
49.5	5.66	22.54	95	96.81	4.98
			100		

Run 3 5/28/2004

Flow Rate (mm)	Flow Rate (sL/min)	Upstream Temp (°C)	Static Pressure (psi)	Static Pressure Act (psi)	Thrust (g)
19.5	2.31	22.28	10	9.27	0.31
21.5	2.53	22.33	15	14.30	0.61
23.0	2.70	22.34	20	19.50	0.84
25.5	2.98	22.36	25	25.00	0.82
27.0	3.15	22.37	30	30.00	1.05
29.0	3.37	22.39	35	35.34	1.25
30.5	3.54	22.40	40	40.72	1.49
32.0	3.70	22.42	45	45.35	1.67
34.0	3.93	22.44	50	51.56	2.00
35.5	4.10	22.45	55	55.63	2.29
37.0	4.26	22.47	60	60.44	2.50
39.0	4.49	22.49	65	66.39	2.83
40.5	4.66	22.51	70	71.67	2.74
42.0	4.82	22.52	75	76.28	3.22
43.5	4.99	22.53	80	81.04	3.66
45.0	5.16	22.54	85	85.39	4.05
47.0	5.38	22.55	90	90.82	4.55
49.0	5.61	22.56	95	97.46	5.00

Run 4 5/28/2004

Flow Rate (mm)	Flow Rate (sL/min)	Upstream Temp (°C)	Static Pressure (psi)	Static Pressure Act (psi)	Thrust (g)
20.0	2.36	23.08	10	11.38	0.39
21.5	2.53	23.08	15	15.08	0.62
23.5	2.75	23.07	20	20.75	0.67
25.5	2.98	23.08	25	25.78	0.85
27.0	3.15	23.08	30	29.92	1.02
29.0	3.37	23.08	35	35.78	1.26
30.0	3.48	23.07	40	40	1.48
32.0	3.70	23.08	45	45.85	1.73
33.5	3.87	23.1	50	50.88	2.05
35.0	4.04	23.09	55	55.25	2.33
36.5	4.21	23.09	60	61.03	2.52
38.0	4.38	23.1	65	66.06	2.68
39.5	4.54	23.09	70	70.41	2.66
41.0	4.71	23.1	75	75.65	3.05
42.5	4.88	23.1	80	80.34	3.43
44.5	5.10	23.1	85	85.82	3.90
46.0	5.27	23.1	90	90.37	4.50
47.5	5.44	23.1	95	95.1	4.93
49.0	5.61	23.1	100	98.97	5.24

Run 5 5/28/2004

Flow Rate (mm)	Flow Rate (sL/min)	Upstream Temp (°C)	Static Pressure (psi)	Static Pressure Act (psi)	Thrust (g)
19.0	2.25	23.17	10	10.54	0.32
20.0	2.36	23.18	15	14.63	0.53
22.5	2.64	23.20	20	21.05	0.57
24.0	2.81	23.20	25	25.77	0.72
25.5	2.98	23.21	30	30.77	0.88
27.0	3.15	23.22	35	35.53	1.08
28.5	3.31	23.23	40	40.33	1.31
30.0	3.48	23.23	45	45.13	1.55
31.5	3.65	23.25	50	50.05	1.77
33.0	3.82	23.25	55	55.90	2.12
34.0	3.93	23.26	60	60.16	2.13
35.5	4.10	23.26	65	65.65	2.44
37.0	4.26	23.27	70	70.58	2.76
38.5	4.43	23.27	75	75.94	3.14
40.0	4.60	23.28	80	80.90	3.28
41.0	4.71	23.29	85	85.26	3.55
43.0	4.93	23.29	90	90.35	3.90
44.5	5.10	23.29	95	96.05	4.35
45.5	5.21	23.30	100	99.86	4.68

Run 6 5/31/2004

Flow Rate (mm)	Flow Rate (sL/min)	Upstream Temp (°C)	Static Pressure (psi)	Static Pressure Act (psi)	Thrust (g)
17.5	2.08	22.64	10	10.64	0.33
19.0	2.25	22.63	15	14.84	0.47
21.0	2.47	22.62	20	19.99	0.50
22.5	2.64	22.62	25	25.10	0.54
24.5	2.87	22.62	30	30.69	0.62
26.0	3.03	22.63	35	36.21	0.89
27.0	3.15	22.64	40	40.26	1.09
29.0	3.37	22.65	45	45.78	1.32
30.5	3.54	22.65	50	50.50	1.54
32.0	3.70	22.67	55	56.20	1.84
33.0	3.82	22.65	60	61.26	2.08
35.0	4.04	22.66	65	66.76	2.37
36.0	4.15	22.67	70	70.85	2.54
37.0	4.26	22.67	75	75.00	2.73
38.5	4.43	22.67	80	80.44	2.97
40.0	4.60	22.67	85	86.17	3.24
41.5	4.77	22.68	90	90.16	3.44
42.5	4.88	22.68	95	94.64	3.99
44.0	5.05	22.68	100	98.64	4.38

Run 7 5/31/2004

Flow Rate (mm)	Flow Rate (sL/min)	Upstream Temp (°C)	Static Pressure (psi)	Static Pressure Act (psi)	Thrust (g)
17.5	2.08	22.70	10	9.77	0.35
19.5	2.31	22.72	15	15.59	0.52
21.5	2.53	22.72	20	21.67	0.42
22.5	2.64	22.72	25	25.00	0.57
24.5	2.87	22.73	30	30.92	0.80
26.0	3.03	22.73	35	35.15	0.94
27.5	3.20	22.73	40	40.38	1.22
29.0	3.37	22.73	45	45.60	1.42
30.0	3.48	22.73	50	50.52	1.63
31.5	3.65	22.73	55	55.30	1.88
33.0	3.82	22.74	60	60.53	2.15
34.5	3.98	22.74	65	66.08	2.44
35.5	4.10	22.75	70	70.96	2.66
37.0	4.26	22.74	75	75.47	2.88
38.5	4.43	22.75	80	81.95	3.17
40.0	4.60	22.75	85	86.72	3.40
41.5	4.77	22.76	90	91.04	3.66
43.0	4.93	22.75	95	96.27	4.22
44.0	5.05	22.75	100	99.47	4.47

Run 8 5/31/2004

Flow Rate (mm)	Flow Rate (sL/min)	Upstream Temp (°C)	Static Pressure (psi)	Static Pressure Act (psi)	Thrust (g)
18.0	2.14	22.77	10	11.41	0.41
19.5	2.31	22.78	15	15.60	0.53
21.0	2.47	22.78	20	20.10	0.53
23.0	2.70	22.79	25	25.86	0.65
24.5	2.87	22.78	30	30.44	0.83
26.0	3.03	22.79	35	35.55	1.02
27.5	3.20	22.79	40	40.20	1.30
29.0	3.37	22.8	45	45.62	1.52
30.0	3.48	22.8	50	50.80	1.77
31.5	3.65	22.81	55	55.26	2.01
32.5	3.76	22.81	60	60.53	2.32
34.5	3.98	22.82	65	65.53	2.61
35.5	4.10	22.82	70	70.49	2.88
37.0	4.26	22.82	75	75.50	3.16
38.0	4.38	22.81	80	80.56	3.40
39.5	4.54	22.82	85	85.31	3.66
41.0	4.71	22.81	90	90.23	3.90
42.5	4.88	22.82	95	95.94	4.56
43.5	4.99	22.81	100	99.30	4.89

Run 9 5/31/2004

Flow Rate (mm)	Flow Rate (sL/min)	Upstream Temp (°C)	Static Pressure (psi)	Static Pressure Act (psi)	Thrust (g)
18.0	2.14	22.82	10	10.39	0.37
19.5	2.31	22.83	15	14.80	0.52
21.5	2.53	22.82	20	20.90	0.48
23.5	2.75	22.83	25	26.90	0.70
24.5	2.87	22.84	30	30.00	0.81
26.0	3.03	22.85	35	35.14	1.01
27.5	3.20	22.84	40	40.40	1.28
29.0	3.37	22.85	45	45.89	1.53
30.5	3.54	22.86	50	50.83	1.77
31.5	3.65	22.87	55	55.55	2.03
33.0	3.82	22.87	60	60.62	2.32
34.5	3.98	22.87	65	65.96	2.62
35.5	4.10	22.87	70	70.53	2.86
37.0	4.26	22.87	75	76.43	3.18
38.0	4.38	22.87	80	80.86	3.38
40.0	4.60	22.87	85	85.55	3.64
41.0	4.71	22.87	90	90.74	3.89
42.5	4.88	22.88	95	95.69	4.50
43.5	4.99	22.87	100	99.24	4.81

Run 10 5/31/2004

Flow Rate (mm)	Flow Rate (sL/min)	Upstream Temp (°C)	Static Pressure (psi)	Static Pressure Act (psi)	Thrust (g)
18.0	2.14	22.84	10	11.31	0.41
19.5	2.31	22.84	15	15.64	0.53
21.5	2.53	22.85	20	21.28	0.49
23.0	2.70	22.85	25	25.50	0.65
25.0	2.92	22.86	30	31.36	0.80
26.0	3.03	22.86	35	35.33	1.00
27.5	3.20	22.86	40	41.02	1.29
29.0	3.37	22.87	45	45.95	1.53
30.0	3.48	22.87	50	50.49	1.74
31.5	3.65	22.87	55	56.51	2.08
32.5	3.76	22.87	60	60.56	2.30
34.5	3.98	22.88	65	66.53	2.62
35.5	4.10	22.88	70	70.53	2.83
37.0	4.26	22.88	75	75.00	3.07
38.5	4.43	22.88	80	80.89	3.35
39.5	4.54	22.88	85	85.25	3.60
41.0	4.71	22.88	90	90.68	3.84
42.5	4.88	22.88	95	95.84	4.35
43.5	4.99	22.88	100	99.71	4.77

Run 11 5/31/2004

Flow Rate (mm)	Flow Rate (sL/min)	Upstream Temp (°C)	Static Pressure (psi)	Static Pressure Act (psi)	Thrust (g)
18.0	2.14	22.86	10	12.10	0.41
19.5	2.31	22.87	15	16.00	0.49
21.0	2.47	22.88	20	21.06	0.45
22.5	2.64	22.89	25	25.36	0.59
24.5	2.87	22.89	30	30.60	0.73
26.0	3.03	22.90	35	35.55	0.95
27.5	3.20	22.90	40	40.76	1.21
29.0	3.37	22.91	45	46.10	1.46
30.0	3.48	22.91	50	50.93	1.68
32.0	3.70	22.92	55	56.17	1.96
33.0	3.82	22.92	60	60.66	2.18
34.5	3.98	22.93	65	65.68	2.44
35.5	4.10	22.92	70	71.00	2.69
37.0	4.26	22.92	75	75.79	2.91
38.0	4.38	22.93	80	80.29	3.08
40.0	4.60	22.93	85	85.78	3.39
41.5	4.77	22.93	90	92.94	3.77
42.5	4.88	22.92	95	96.05	4.19
43.5	4.99	22.92	100	99.86	4.55

E.2 With AFC

E.2.1 Membrane Pressure of 0 psi

Run 1 6/13/2004

Upstream Temp (°C)	Static Pressure (psi)	Static Pressure Act (psi)	Thrust (g)
21.56	10	10.22	0.20
21.61	20	20.71	0.37
21.61	30	31.57	0.51
21.62	40	41.54	0.63
21.65	50	51.47	0.58
21.66	60	60.95	0.67
21.68	70	71.49	0.74
21.70	80	81.32	0.88
21.74	90	92.83	1.07
21.76	100	100.51	1.17

Run 2 6/13/2004

Upstream Temp (°C)	Static Pressure (psi)	Static Pressure Act (psi)	Thrust (g)
21.61	10	10.82	0.22
21.62	20	20.41	0.37
21.65	30	31.43	0.54
21.67	40	40.57	0.62
21.68	50	50.48	0.57
21.70	60	61.24	0.67
21.71	70	70.46	0.75
21.74	80	81.40	0.89
21.76	90	91.89	1.06
21.78	100	99.62	1.12

Run 5 6/13/2004

Upstream Temp (°C)	Static Pressure (psi)	Static Pressure Act (psi)	Thrust (g)
21.57	10	10.81	0.18
21.58	20	20.28	0.25
21.61	30	30.76	0.38
21.64	40	41.52	0.36
21.67	50	51.52	0.54
21.69	60	62.52	0.63
21.71	70	71.58	0.72
21.73	80	80.96	0.90
21.81	90	90.87	1.15
21.77	100	98.81	1.27

E.2.2 Membrane Pressure of 20 psi

Run 3 6/13/2004

Upstream Temp (°C)	Static Pressure (psi)	Static Pressure Act (psi)	Thrust (g)
21.61	10	10.70	0.06
21.62	20	20.16	0.16
21.65	30	30.65	0.32
21.66	40	41.77	0.47
21.66	50	50.75	0.49
21.68	60	60.66	0.48
21.70	70	72.00	0.67
21.72	80	81.52	0.79
21.73	90	90.00	0.88
21.77	100	98.04	0.95

Run 4 6/13/2004

Upstream Temp (°C)	Static Pressure (psi)	Static Pressure Act (psi)	Thrust (g)
21.52	10	11.80	0.09
21.56	20	20.41	0.21
21.61	30	31.10	0.35
21.63	40	40.27	0.45
21.66	50	51.99	0.59
21.66	60	61.02	0.41
21.68	70	71.73	0.63
21.70	80	80.72	0.71
21.74	90	92.81	0.79
21.76	100	98.67	0.87

7 References

Anderson, J. D. (2001). *Fundamentals of Aerodynamics*. New York, NY: McGraw-Hill.

Back, L. H., Cuffel, R. F., & Massier, P. F. (1972). Influence of Contraction Section Shape and Inlet Flow Direction on Supersonic Nozzle Flow and Performance. *Journal of Spacecraft and Rockets. 9(6), 420-427.*

Baechi, D., Buser, R. (2000). Suspension Handling System. *Sensors and Actuators B.* 63, 195-200.

Baechi, D., Dual, J., & Buser, R. (2001). A High Density Microchannel Network with Integrated Valves and Photodiodes. *The 14th IEEE International Conference on Micro Electro Mechanical Systems.* January 21-25 (pp. 463-466), IEEE.

Bayt, R., Breuer, K. (2001). Systems design and performance of hot and cold supersonic microjets. *39th AIAA Aerospace Sciences Meeting and Exhibit*, January 8-11 (pp. 1-10). AIAA.

Boedo, S. (1999). Evaluation and Comparison of Plate Finite Elements in ANSYS. *NAFEMS World Congress '99: Effective Engineering Analysis.* April 25-28 (pp. 965-975). NAFEMS.

Bousse, L., Dijkstra, E., & Guenat, O. (1996). High-Density Arrays of Valves and Interconnects for Liquid Switching. *Solid-State Sensor and Actuator Workshop.* June 2-6 (pp. 272-275), TRF.

Christophorou, C., Nagib, H., Naguib, A., Fabris, D. (2000). Array of MEMS-based actuators for the excitation of a high-speed axisymmetric jet. *Fluids 2000 Conference and Exhibit.* June 19-22 (pp. 1- 4). AIAA.

Choudhuri, A. R., Baird, B., Gollahalli, S. R., Schneider, S. J. (2001). Effects of geometry and ambient pressure on micronozzle flow. *37th AIAA/ASME/SAE/ASEE Joint Propulsion Conference and Exhibit.* July 8-11 (pp. 1-9). AIAA.

Fox, R. W., McDonald, A. T. (1998). *Introduction to fluid mechanics*. New York, NY: John Wiley & Sons, Inc.

Grisnik, S. P., Smith, T. A. (1987). *Experimental study of low Reynolds number nozzles* (NASA TM-89858). Cleveland, OH: National Aeronautics and Space Administration.

Janson, S., Helvajian, H., Amimoto, S., Smit, G., Mayer, D., Feuerstein, S. (1998). Microtechnology for space systems. *Proceeding of the IEEE Aerospace Conference*, March 21-28 (1, pp. 409-418). IEEE.

Kempski, M. H., Taber, L. A., & Su, F. C. (1988). Large Elastic Deformation of Shear Deformable Shells of Revolution: Numerical and Experimental Results. *Journal of Applied Mechanics*, 55, 629-634.

Mueller, J., Marrese, C., Polk, J., Yang, E., Green, A., White, V. et al. (2003). An overview of MEMS-based micropropulsion developments at JPL. *Acta Astronautica*, 52(9-12), 881-895.

Mueller, J. (1999). A review and applicability assessment of MEMS-based microvalve technologies for microspacecraft propulsion. *35th AIAA/ASME/SAE/ASEE Joint Propulsion Conference and Exhibit*. June 20-24 (pp. 1- 18). AIAA.

Rothe, D. E. (1970). Electron-beam studies of viscous flow in supersonic nozzles. *AIAA Journal*. 9(5), 804-810.

Smith, B. L., Glezer, A. (2002). Jet vectoring using synthetic jets. Journal *of Fluid Mechanics*. 458, 1-34.

Sommer, C., & Sommer, S. (2000). *Wire EDM Handbook*. Houston, TX: Advanced Publishing.

Suzuki, H., Kasagi, N., Suzuki, Y., Shima, H. (1999). Manipulation of a round jet with electromagnetic flap actuators. *Twelfth IEEE International Conference Micro Electro Mechanical Systems*. January 17-21 (pp. 534-540). IEEE.

Wolden, C. (2001). *RCA Clean*. Retrieved June 28, 2004, from Colorado School of Mines, Colin Wolden's Web site: http://www.mines.edu/fs_home/cwolden/chen435/clean.htm

Yang, X., Grosjean, C., & Tai, Y. (1999). Design, Fabrication, and Testing of Micromachined Silicone Rubber Membrane Valves. *Journal of Microelectromechanical Systems*. 8(4), 393-402.

Young, W. C. (1989). *Roark's Formulas for Stress & Strain* (6th ed.).New York: McGraw-Hill.

Zdeblick, M. J., Anderson, R., Jankowski, J., KlineSchoder, B., Christel, L., Miles, R. et al. (1994). Theropneumatically Actuated Microvalves and Integrated Electro-fluidic Circuits. Solid-State Sensor and Actuator Workshop Hilton Head, South Carolina, June 13-16 (pp. 251-255). IEEE.

Zelesnik, D., Dunn, T., & Micci, M. M. (1991). Numerical and Experimental Investigation of Low Reynolds Number Nozzle Flows. *AIAA/NASA/OAI Conference on Advanced SEI Technologies*. September 4-6 (pp. 1-10). AIAA.